SANDIA REPORT
SAND2011-4751
Unlimited Release
Printed September 2011

Packaging Strategies for Printed Circuit Board Components
Volume I: Materials & Thermal Stresses

Doug Adolf, Scott Spangler, and Kevin Austin (1833)
Matthew Neidigk and Mike Neilsen (1526)
Robert Chambers (1524)

Prepared by
Sandia National Laboratories
Albuquerque, New Mexico 87185 and Livermore, California 94550

Sandia National Laboratories is a multi-program laboratory managed and operated by Sandia Corporation, a wholly owned subsidiary of Lockheed Martin Corporation, for the United States Department of Energy's National Nuclear Security Administration under contract DE-AC04-94AL8500.

Approved for public release; further dissemination unlimited.

Sandia National Laboratories

Issued by Sandia National Laboratories, operated for the United States Department of Energy by Sandia Corporation.

NOTICE: This report was prepared as an account of work sponsored by an agency of the United States Government. Neither the United States Government, nor any agency thereof, nor any of their employees, nor any of their contractors, subcontractors, or their employees, make any warranty, express or implied, or assume any legal liability or responsibility for the accuracy, completeness, or usefulness of any information, apparatus, product, or process disclosed, or represent that its use would not infringe privately owned rights. Reference herein to any specific commercial product, process, or service by trade name, trademark, manufacturer, or otherwise, does not necessarily constitute or imply its endorsement, recommendation, or favoring by the United States Government, any agency thereof, or any of their contractors or subcontractors. The views and opinions expressed herein do not necessarily state or reflect those of the United States Government, any agency thereof, or any of their contractors.

Printed in the United States of America. This report has been reproduced directly from the best available copy.

Available to DOE and DOE contractors from
U.S. Department of Energy
Office of Scientific and Technical Information
P.O. Box 62
Oak Ridge, TN 37831

Telephone: (865) 576-8401
Facsimile: (865) 576-5728
E-Mail: reports@adonis.osti.gov
Online ordering: http://www.osti.gov/bridge

Available to the public from
U.S. Department of Commerce
National Technical Information Service
5285 Port Royal Rd.
Springfield, VA 22161

Telephone: (800) 553-6847
Facsimile: (703) 605-6900
E-Mail: orders@ntis.fedworld.gov
Online order: http://www.ntis.gov/help/ordermethods.asp?loc=7-4-0#online

SAND2011-4751
Unlimited Release
Printed September 2011

Packaging Strategies for Printed Circuit Board Components
Volume I: Materials & Thermal Stresses

Doug Adolf, Matthew Neidigk, Mike Neilsen, Robert Chambers
Scott Spangler and Kevin Austin,
Sandia National Laboratories
Albuquerque, NM 87185

Abstract

Decisions on material selections for electronics packaging can be quite complicated by the need to balance the criteria to withstand severe impacts yet survive deep thermal cycles intact. Many times, material choices are based on historical precedence perhaps ignorant of whether those initial choices were carefully investigated or whether the requirements on the new component match those of previous units. The goal of this program focuses on developing both increased intuition for generic packaging guidelines and computational methodologies for optimizing packaging in specific components. Initial efforts centered on characterization of classes of materials common to packaging strategies and computational analyses of stresses generated during thermal cycling to identify strengths and weaknesses of various material choices. Future studies will analyze the same example problems incorporating the effects of curing stresses as needed and analyzing dynamic loadings to compare trends with the quasi-static conclusions.

CONTENTS

1 Introduction 7

2 Material Characterization 8
- 2.1 Encapsulants 8
  - 2.1.1 Nonlinear Viscoelastic Response of Epoxy Encapsulants 8
  - 2.1.2 Predicting Cohesive Failure in Epoxy Encapsulants 18
  - 2.1.3 Adhesive Failure in Epoxy Encapsulants 19
  - 2.1.4 Linear Thermoelastic Response of Rigid Foams 22
- 2.2 Underfills 24
  - 2.2.1 Characterization of the Underfills 24
  - 2.2.2 Generic Nonlinear Viscoelastic Model for Epoxies 32
  - 2.2.3 Generic Nonlinear Viscoelastic Model for Epoxies with Hard Fillers 35
  - 2.2.4 Generic Nonlinear Viscoelastic Model for Epoxies with the iM30k Filler 41
- 2.3 Coatings 43
  - 2.3.1 Unfilled Silicone 44
  - 2.3.2 Unfilled Polysulfide 47
  - 2.3.3 GMB-Filled Silicone 51
  - 2.3.4 PMB-Filled Polysulfide 53
- 2.4 Printed Circuit Boards 55
  - 2.4.1 Test Procedure for the 3-D Linear Thermoelastic Properties of PCBs 56
  - 2.4.2 Characterization of a Single Ply of FR04-08 58
  - 2.4.3 Predicting Multi-Ply Response 61
  - 2.4.4 Comparison to Other PCBs 64
- 2.5 Solders 68

3 Finite element Analyses 72
- 3.1 Coating Stresses 77
  - 3.1.1 Epoxy Encapsulant 77
  - 3.1.2 Foam Encapsulant / No Encapsulant 79
- 3.2 Component Stresses 80
  - 3.2.1 Epoxy Encapsulant 80
  - 3.2.2 Foam Encapsulant / No Encapsulant 85
- 3.3 Solder Fatigue 89
  - 3.3.1 Epoxy Encapsulant 89
  - 3.3.2 Foam Encapsulant / No Encapsulant 92
- 3.4 Underfill Stresses 96
  - 3.4.1 Epoxy Encapsulant 96
  - 3.4.2 Foam Encapsulant / No Encapsulant 100
- 3.5 PCB Bending during Thermal Cycles 101

4 Conclusions and Future Studies 103

5 References 109

1 INTRODUCTION

DOE and DoD printed circuit board (PCB) assemblies are often subjected to more severe environments than experienced by commercial assemblies. Historically, Sandia boards have been encapsulated in foam or epoxy to improve survivability in shock and vibration. Unfortunately, the large coefficients of thermal expansion (CTE) of these polymers compared to ceramic components, metal solders, and the fiber mat reinforced boards themselves can generate significant stresses in thermal cycles. A compromise must be achieved between the mechanical stability offered by the encapsulants and the thermal cycling stresses generated by them. The introduction of surface mounted components shown in **Error! Reference source not found.** adds additional complexity due to the more rigid attachment to the PCB potentially increasing component stresses, and underfills or coatings may now be required.

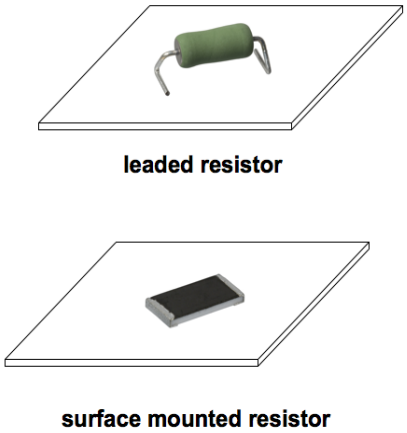

Figure 1-1: Surface mount technology

While past experience can indicate historically successful packaging strategies, new technologies, more complex designs, and less robust components can often cause uncertainty as to the "best" options. The goal of this study focuses on developing general packaging guidelines for generic application as well as methodologies for determining optimal solutions for a specific application. Our approach will combine experimental tests and computational simulations to understand the advantages and disadvantages of coatings/underfills/encapsulants and to identify material properties leading to robust designs. While both quasi-static stresses from manufacturing and thermal cycles and dynamic stresses from vibration and impact are important and will be studied, these first investigations have focused more heavily on the thermal cycle issues. To compare and assess design and material choices, metrics of concern need to be identified. We have chosen to monitor stresses in the board, individual components (e.g., a capacitor), the underfill, possible coating, and solder. Materials used in this study are discussed in Section 2, and preliminary finite element analyses (FEA) are presented in Section 3.

2 MATERIAL CHARACTERIZATION

The variety of materials used in PCB assemblies worldwide is enormous, so no attempt was made to characterize even the more common choices. Rather, we focused on characterization of representatives of different material classes to highlight trends that would guide rational material selection from finite element analysis (FEA) results. As examples of typical encapsulants, we chose an epoxy filled with hollow glass spheres (D32 glass microballoons or GMB from 3M), a 20 lb/ft^3 rigid polyurethane foam, and no over encapsulation. For underfill options, we examined two filler types at various loading levels. As discussed later, no variation in the unfilled epoxy was investigated since the properties of unfilled epoxies are fairly universal when normalized to the glass transition temperature (Tg). For example, the CTE of an unfilled epoxy is roughly 65 ppm/^{o}C for a test temperature that is 50°C below Tg regardless of the polymer composition. In contrast, addition of fillers can greatly affect polymer properties, and filler type can determine which properties are most affected. In particular, "hard" fillers such as glass or alumina significantly lower the CTE but also significantly increase the moduli. GMB decrease the CTE to a lesser extent but can actually decrease the modulus. To identify trends, we limited our study to one base epoxy but investigated the effect of different loading levels for both alumina and GMB fillers.

Coatings can be applied for multiple reasons: stress relief from over-encapsulation, prevention of dielectric breakdown, environmental protection when unencapsulated, and others. Not surprisingly, the range of materials that have been employed is equally broad spanning both glassy and rubbery materials that can be unfilled or filled with "hard" fillers or microballoons at various levels. In these initial studies, we chose two rubbery materials, silicone or polysulfide (since both have very low Tgs), and either unfilled or filled with microballoons. The silicone was filled with a low density GMB while the polysulfide used the phenolic microballoons (PMB) historically used with this material at Sandia. An unfilled glassy epoxy was also examined of the same composition used in the underfills.

While both tin-lead and lead-free solders are currently used, these initial investigations examined only the tin-lead solder. As such, only the historical FR04-08 PCB material was investigated. The higher Tg board materials required for the higher processing temperatures associated with lead-free solders will be added in future studies.

2.1 Encapsulants

2.1.1 Nonlinear Viscoelastic Response of Epoxy Encapsulants

The GMB filled epoxy encapsulant chosen for these studies is the most commonly used system at Sandia: the diglycidyl ether of bisphenol A (Epon 828, Resolution Chemicals) cured with 12 phr diethanolamine (DEA, Fisher Scientific) and filled with 48vol% of GMB (D32/4500, 3M Corp.). The linear and nonlinear behavior of the unfilled epoxy has been characterized previously, and the responses were predicted accurately using a nonlinear viscoelastic constitutive equation developed at Sandia and extensively documented in the literature, the Simplified Potential Energy Clock Model (SPEC model).[1-4] This model employs a new "material clock" describing the dependence of relaxation rates on the potential energy of the system. The Cauchy stress, $\underline{\underline{\sigma}}$, is given by

$$
\begin{aligned}
\underline{\underline{\sigma}} = \frac{\rho}{\rho_{ref}} \Bigg[& K_d(T) \int_0^t ds\, \mathrm{f_v}(\mathrm{t^*\text{-}s^*})\, \frac{\mathrm{dI_1}}{\mathrm{ds}} - L_d(T) \int_0^t ds\, \mathrm{f_v}(\mathrm{t^*\text{-}s^*})\, \frac{\mathrm{dT}}{\mathrm{ds}} \Bigg] \underline{\underline{\mathrm{I}}} \\
& + \frac{2\rho G_d(T)}{\rho_{ref}} \int_0^t ds\, \mathrm{f_s}(\mathrm{t^*\text{-}s^*}) \left[\underline{\underline{R}}(t) \cdot \underline{\underline{\mathrm{d}}}_{dev}(s) \cdot \underline{\underline{R}}(t)^{-1} \right] \qquad (2.1) \\
& + \frac{\rho}{\rho_{ref}} \left[K_\infty(T)\, \mathrm{I_1} - L_\infty(T)\, \{\mathrm{T - T_{ref}}\} \right] \underline{\underline{\mathrm{I}}} + \frac{2\rho G_\infty(T)}{\rho_{ref}} \left[\underline{\underline{R(t)}} \cdot \underline{\underline{\varepsilon}}_{dev} \cdot \underline{\underline{R(t)}}^{-1} \right]
\end{aligned}
$$

There are two relaxation functions, f_V (volumetric) and f_S (shear), represented as stretched exponentials, $\exp[-(t/\tau)^\beta]$, which depend on the "material time interval" shown in Eq. 2.2.

$$
\mathrm{t^* - s^*} = \int_s^t \frac{\mathrm{dx}}{\mathrm{a(x)}} \qquad (2.2)
$$

The classic "viscoelastic shift factor", a, is calculated using Eq. 2.3.

$$
\begin{aligned}
\log \mathrm{a} = -\frac{\mathrm{C_1 N}}{\mathrm{C_2 + N}} \quad & \text{where} \\
\mathrm{N} = & \left[\{\mathrm{T - T_{ref}}\} - \int_0^t \mathrm{ds}\, \mathrm{f_v}(\mathrm{t^*\text{-}s^*})\, \frac{\mathrm{dT}}{\mathrm{ds}} \right] \\
& + \mathrm{C_3} \left[\mathrm{I_1} - \int_0^t \mathrm{ds}\, \mathrm{f_v}(\mathrm{t^*\text{-}s^*})\, \frac{\mathrm{dI_1}}{\mathrm{ds}} \right] \qquad (2.3) \\
& + \mathrm{C_4} \int_0^t \int_0^t \mathrm{ds\, du}\, \mathrm{f_s}(\mathrm{t^*\text{-}s^*, t^*\text{-}u^*})\, \underline{\underline{\mathrm{d}}}_{\mathrm{dev}}(\mathrm{s}) : \underline{\underline{\mathrm{d}}}_{\mathrm{dev}}(\mathrm{u})
\end{aligned}
$$

Variables used in Eqs 2.1-2.3 are defined in Table 2-1.

Table 2-1: Variables used in the SPEC nonlinear viscoelastic model.

variable	definition
ρ	density
T	temperature
T_{ref}	reference temperature where the epoxy is stress free
ρ_{ref}	density at the reference temperature
K_∞	temperature dependent equilibrium (i.e., above Tg) bulk modulus
L_∞	K_∞ times the equilibrium volumetric CTE, α_∞
G_∞	temperature dependent equilibrium shear modulus
K_d	temperature dependent glassy bulk modulus, K_g, minus K_∞
L_d	$K_g\alpha_g - L_\infty$, where α_g is the glassy volumetric CTE
G_d	temperature dependent glassy shear modulus, G_g, minus G_∞
$\underline{\underline{R}}$	rotational component of the deformation tensor
$\underline{\underline{d}}_{dev}$	the deviatoric unrotated rate of deformation tensor
$\underline{\underline{\varepsilon}}_{dev}$	time integral of $\underline{\underline{d}}_{dev}$
I_1	first invariant of $\underline{\underline{\varepsilon}}_{dev}$
C_1	first "WLF" coefficient
C_2	uniquely related to the second "WLF" coefficient
C_3	constant producing the pressure dependence of Tg
C_4	constant producing yield
τ_s	stretched exponential time constant for the shear spectrum
β_s	stretched exponential exponent for the shear spectrum
τ_v	stretched exponential time constant for the volumetric spectrum
β_v	stretched exponential exponent for the volumetric spectrum

A wide range of responses for the base 828/DEA resin cured at 71°C for 24 hours were previously measured and predicted. Examples are shown in Figure 2-1 to Figure 2-3 for the material properties listed in Ref. 4.

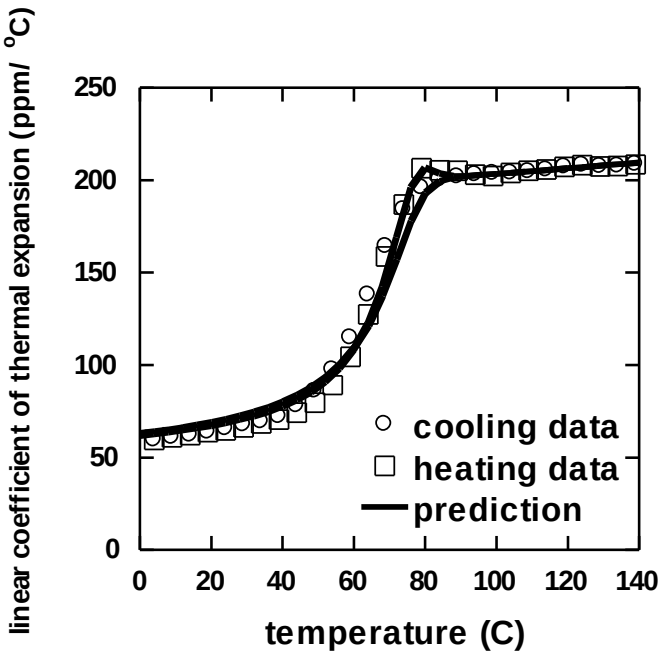

Figure 2-1: Comparison of predictions and data for thermal expansion. Note that the epoxy's Tg is roughly 70°C.

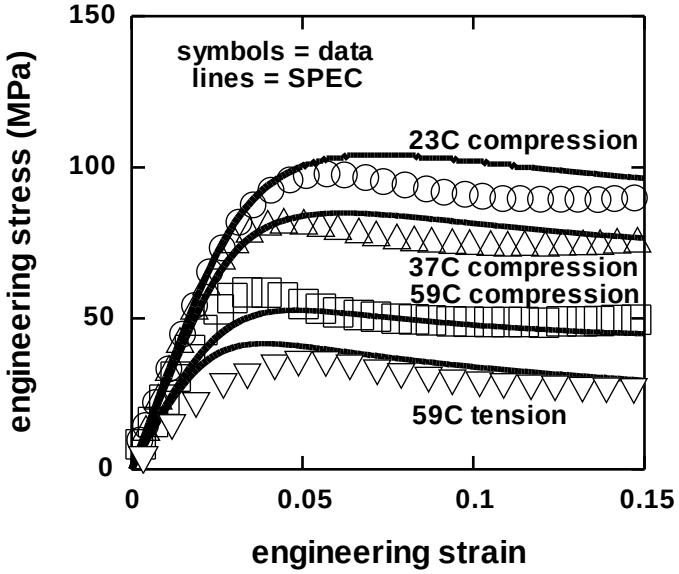

Figure 2-2: Comparison of predictions and data for the temperature dependence of compressive yield and for the difference between tensile and compressive yield at one temperature.

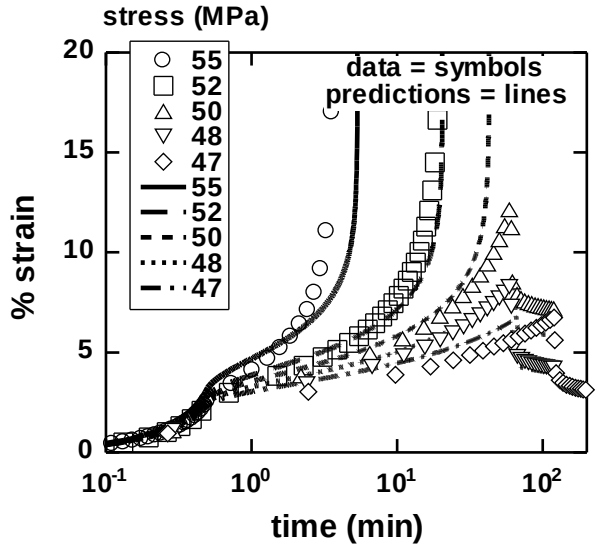

Figure 2-3: Measured and predicted creep at 23°C after a fast quench from 100°C.

The nonlinear response of the 828/DEA epoxy filled with either 30 or 45 vol.% glass spheres (Agsco A3000, ρ=1.2 g/cc, mean diameter of roughly 40 microns) was also predicted previously.[5] The heterogeneous composite was characterized as if it were a one-phase epoxy, and the effective moduli and CTE were directly input into the model. As seen in Figure 2-4 through Figure 2-6, the model also accurately captures the nonlinear response of filled epoxies.

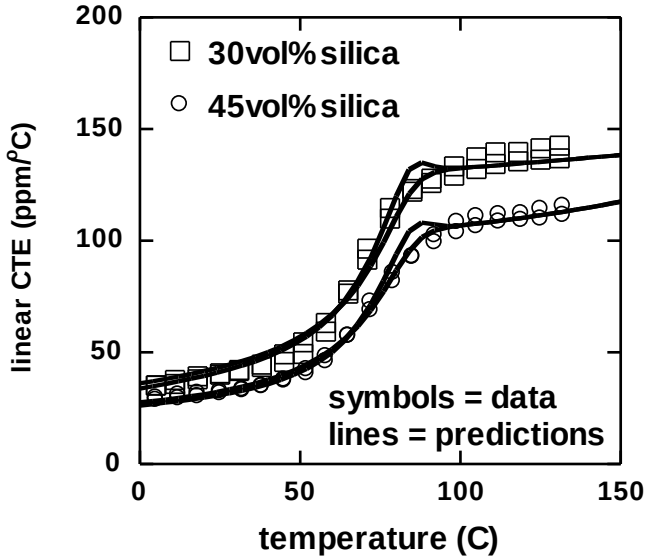

Figure 2-4: Measured and predicted CTE's of silica filled 828/DEA.

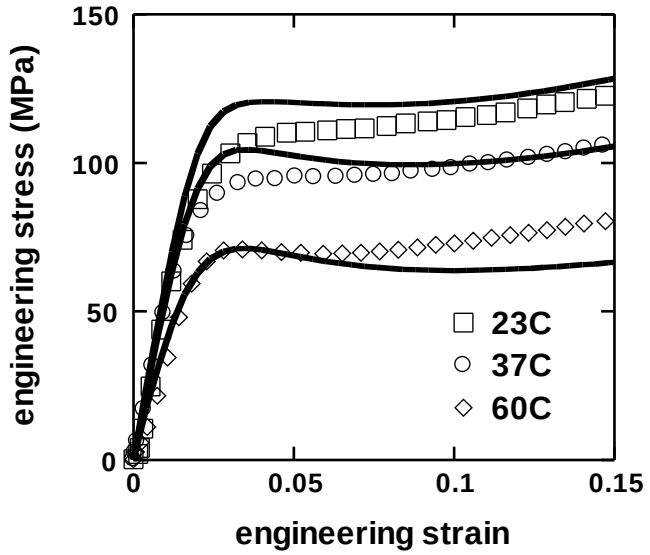

Figure 2-5: Measured and predicted compressive yield stresses of 30 vol% silica filled 828/DEA at various temperatures.

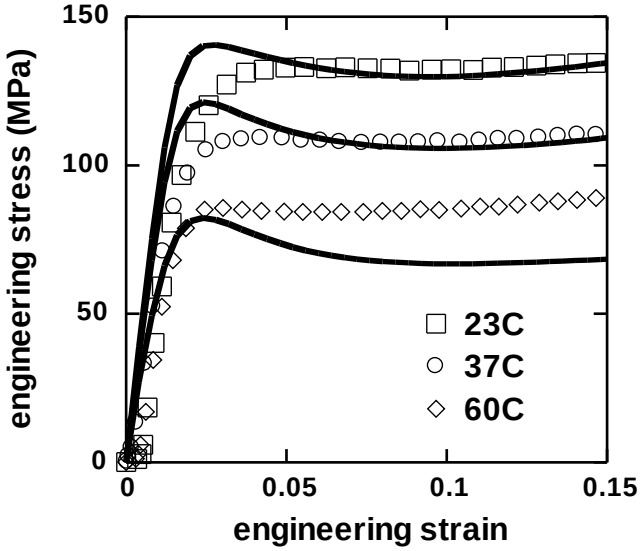

Figure 2-6: Measured and predicted compressive yield stresses of 45 vol% silica filled 828/DEA at various temperatures.

The D32 GMB filled epoxy was characterized for this study. Required inputs for model parameterization are the linear viscoelastic shear master curve (ARES rheometer, TA Instruments using 0.125 x 0.5 x 2.25" torsion rectangular geometry), oscillatory shear modulus as a function of temperature (ARES at a scan rate of 2°C/min), the coefficient of thermal expansion (Q400 thermomechanical analyzer, TA Instruments, at a scan rate of 2°C/min), bulk

modulus (cylindrical specimen with biaxial strain gauge in a pressure vessel), and compressive yield stress (1125 load frame, Instron Corp. at a strain rate of 10%/min). The data are presented in Figure 2-7 through Figure 2-10, and the model parameters are given in Table 2-2. Examples of model predictions are also shown in Figure 2-11 and Figure 2-12. Note that the glassy model parameters need not exactly match the values extracted directly from the experimental data due to the effects of viscoelasticity. In particular, the experimental value of the CTE at Tg is roughly 45 ppm/C, whereas the model input is only 27 ppm/C. Also note that the experimental compressive yield samples in Figure 2-12 failed at about 4-5% strain.

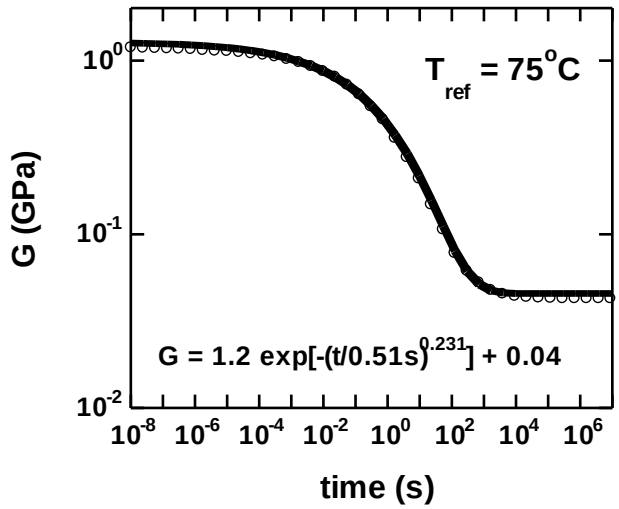

Figure 2-7: Shear stress relaxation master curve at a reference temperature of 75°C constructed from oscillatory data.

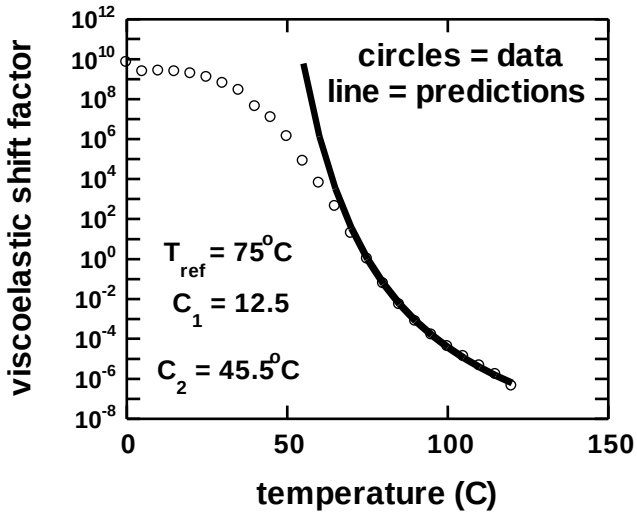

Figure 2-8: Experimental viscoelastic shift factors obtained from the master curve of Figure 2-7. The WLF fit above Tg is shown as well.

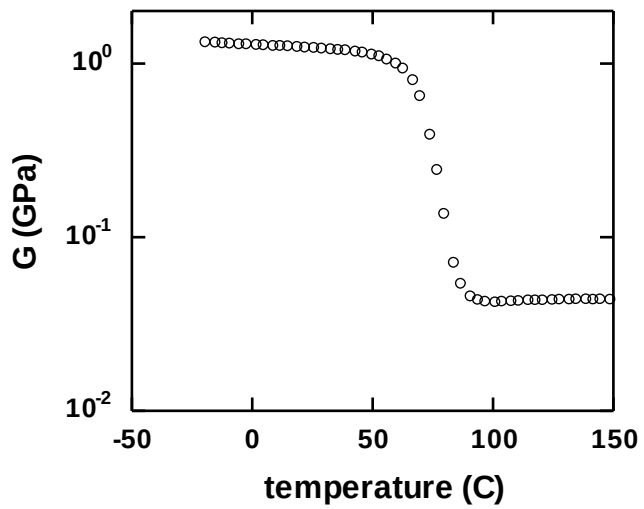

Figure 2-9: Oscillatory shear storage modulus at 1 Hz as a function of temperature.

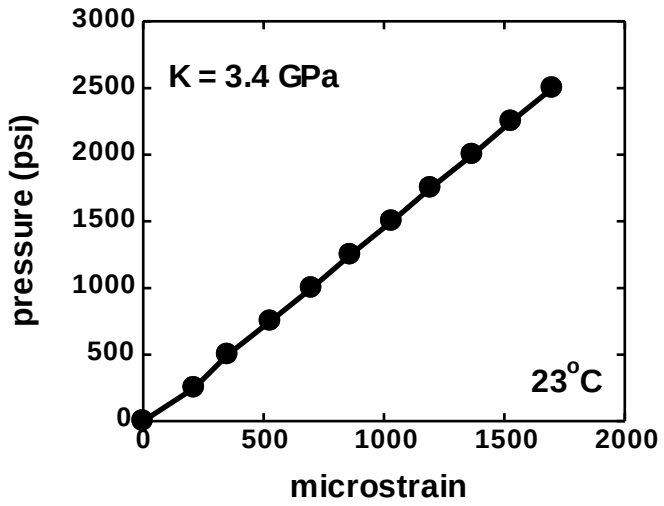

Figure 2-10: Bulk modulus determined from a pressure dilatometer.

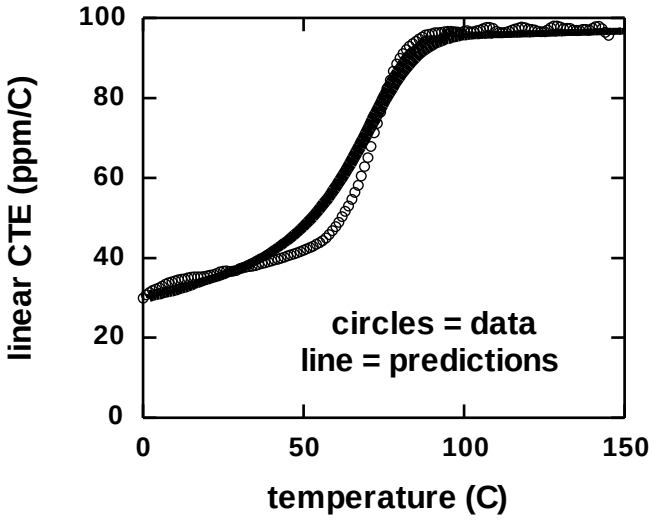

Figure 2-11: Measured and predicted volumetric strains in free expansion.

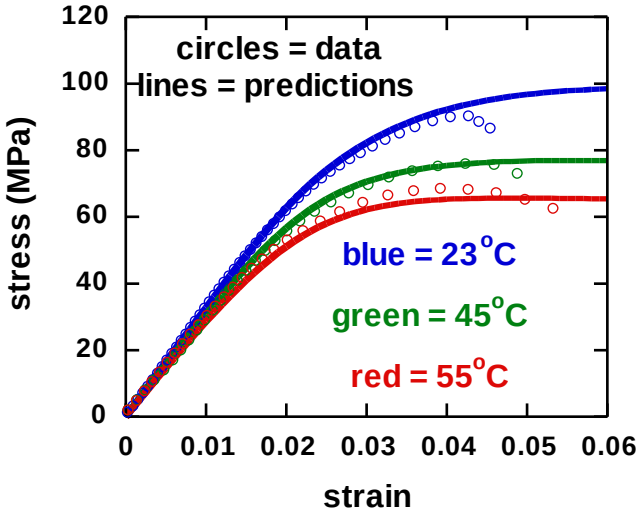

Figure 2-12: Measured and predicted compressive yield at various temperatures.

Table 2-2: Nonlinear viscoelastic model parameters for the 828/DEA/GMB epoxy.

variable	value	units
ρ_{ref}	750	kg/m3
T_{ref}	75	^oC
K_∞ at T_{ref}	3.35	GPa
dK_∞/dT	0	GPa/^oC
linear α_∞ at T_{ref}	95	ppm/^oC
$d\alpha_\infty/dT$	0.023	ppm/$^oC^2$
G_∞ at T_{ref}	40	MPa
dG_∞/dT	0.05	MPa/^oC
K_g at T_{ref}	3.35	GPa
dK_g/dT	0	GPa/^oC
linear α_g at T_{ref}	27	ppm/^oC
$d\alpha_g/dT$	0.033	ppm/$^oC^2$
G_g at T_{ref}	1.2	GPa
dG_g/dT	-1	MPa/^oC
C_1	12.5	
C_2	45.4	^oC
C_3	2000	
C_4	17,500	Pa
τ_s	0.51	sec
β_s	0.231	
τ_v	20	sec
β_v	0.15	

The advantage of these GMB filled encapsulants lies in the variation in thermoelastic properties arising from this unique filler. While most hard fillers (e.g., silica, alumina, titania) lower the CTE, the moduli increase severely. As an example, 40% filler volume fraction of alumina decreases the CTE to 30 ppm/C but increases the shear modulus to 5 GPa. Therefore, the effect of additional hard filler on stresses generated during thermal cycles is unclear and depends on the boundary conditions of that particular problem. As seen in Table 2-3, GMB fillers reduce the CTE and bulk moduli while increasing the shear modulus only slightly. The product of the CTE and either bulk or Young's modulus is lower when GMB are added, so even in highly confined geometries, the stresses generated during thermal cycles are lower.

Table 2-3: Stress quantities for the GMB filled and unfilled 828/DEA epoxy at room temperature.

variable	828/DEA	828/DEA/GMB
linear α (ppm/^{o}C)	65	35
G (GPa)	0.95	1.1
K (GPa)	6.0	3.4
E α (kPa/^{o}C)	176	105
K α (kPa/^{o}C)	390	120

2.1.2 Predicting Cohesive Failure in Epoxy Encapsulants

Perhaps the creep response of the unfilled epoxy in Figure 2-3 provides the best opportunity to understand the physical mechanism underlying cohesive failure. The creep curves have a characteristic shape in which creep rates immediately after application of the constant load are relatively slow but increase as time progresses. Failure is coincident with a sharp increase in the creep rates as the sample lengthens catastrophically. This sharp increase is predicted naturally from the SPEC nonlinear viscoelastic model in which relaxation rates are dependent on potential energy. Since energy is not directly stress but involves strain as well, the relaxation (i.e., creep) rates increase as strain increases. The dramatic lengthening at failure is a consequence of a nonlinear feedback leading to "runaway" nonlinear viscoelastic creep. This same mechanism should now be apparent in the yield stress tests where a similar feedback mechanism occurs as the ramped load increases.

Within a finite element code, this mechanism could be captured by examining the maximum principal strains in all elements. The signature of runaway nonlinear viscoelasticity would coincide with a critical and rather large value of the maximum principal strains. For the unfilled epoxy, a value of roughly 20% seems to be consistent with the data. Failure predictions would be relatively insensitive to the exact value of this critical metric since the strains (e.g., creep in Figure 2-3) nearly diverge at failure, so metrics of 15, 20 or even 40% are almost indistinguishable. From a purely computational perspective, a smaller value would prove more convenient since the codes have difficulty converging when local strains increase rapidly.

The critical maximum principal strain of the GMB-filled epoxy appears smaller, roughly 4-5%. While the data are limited, this observation may be reasonable since the balloons, being hollow, are more fragile than a solid, hard particle. The large increase and localization of the strains near failure could cause the balloons to fail prior to the epoxy failure itself. Once balloons start to fail, the adjacent epoxy strains will increase dramatically causing the epoxy to fail at apparently the same time.

2.1.3 Adhesive Failure in Epoxy Encapsulants

Adhesive strengths of the epoxy encapsulants were measured using the napkin ring geometry shown in Figure 2-13. This test is unique in its ability to produce a uniform state of stress from which the tangential surface traction at failure can be extracted cleanly. A ring of epoxy is bonded to the lower flat plate (1 inch diameter) and the upper thin annulus (0.75 inch outer diameter and 0.1 inch thickness). A low friction dowel adjusted by screws sets the gap (nominally 0.02 inch) during cure. Initial constant angular rotation tests determined the critical tractions as a function of temperature. Later creep tests at room temperature only, determined the time to fail at various sub-critical torques.

Figure 2-13: Napkin ring test geometry.

The critical tractions for the 828/DEA epoxy are shown in Figure 2-14 along with the predicted shear yield stresses. Adhesive de-bonding appears to correlate with the yield of the bulk epoxy. One reasonable physical explanation acknowledges that the Tg of a polymer near an interface is typically depressed by a few degrees.[6] Therefore, that material will yield prior to the bulk polymer, and further bulk displacement will localize strains in the region near the interface. De-bonding could be described by the same "run-away" nonlinear viscoelasticity outlined above but localized to the interface due to the depressed Tg in that region.

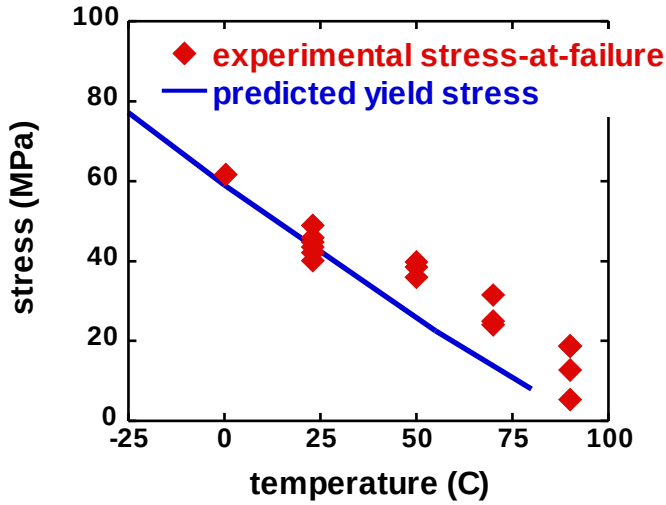

Figure 2-14: Experimental napkin ring stress-at-failure and predicted epoxy yield stresses for the 828/DEA epoxy as a function of temperature.

Typical tensile creep data and predictions[4] on the 828/DEA epoxy at room temperature for an applied stress of 55 MPa are shown in Figure 2-15 for two different cooling profiles: a "fast quench" representing placing the sample on a bench after removal from an oven and a "slow cool" representing turning off the power with the sample in the oven. Note that the creep rates vary by three orders of magnitude, so predictions of the creep response in the napkin ring test will be sensitive to the assumed cooling rate. Since the upper and lower steel plugs are quite massive, we have assumed here the slow cooling rate (0.5^{o}C/min) although it is obviously approximate and thermal gradients may even exist. Nevertheless, the experimental napkin ring times-to-fail match the predicted creep times-to-fail (taken as the time when the sample strain reaches a large value of ~25%) in Figure 2-16. This result seems to validate the "run-away" nonlinear viscoelastic de-bonding mechanism and gives us a method to predict not only stresses in the encapsulant, but allows us to estimate when these stresses become excessive.

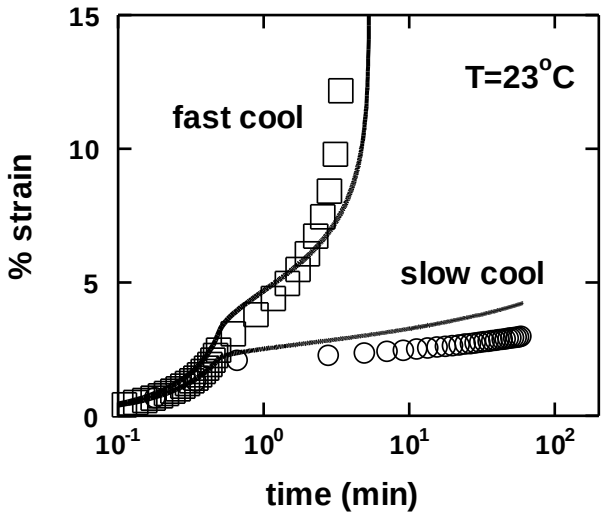

Figure 2-15: Tensile creep data and predictions for the 828/DEA epoxy at 23oC.

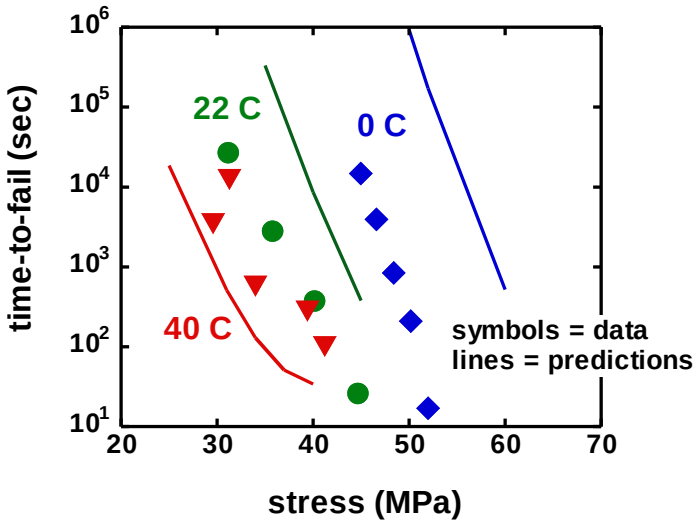

Figure 2-16: Experimental and predicted times-to-fail for the 828/DEA epoxy in napkin ring creep tests at 23oC.

Several sensitivity studies of the napkin ring adhesive strength were performed previously.[7] Of particular interest here, the adhesive strength of the 828 epoxy reacted with a mixture of two amines (an aliphatic amine, Jeffamine D230, Huntsman, at 16.7 phr, and an cycloaliphatic amine, Ancamine 2049, Air Products Allentown, at 16.7 phr) was measured with alumina fillers. The volume fraction of alumina was varied from 43 to 48vol%, which is quite high, and two different types of alumina were investigated (a tabular alumina, T64, Alcoa, and a spherical alumina, AA18, Sumitomo). The adhesive strength was unaffected by filler loading, perhaps due to steric exclusion of the filler from direct interfacial contact (Figure 2-17).

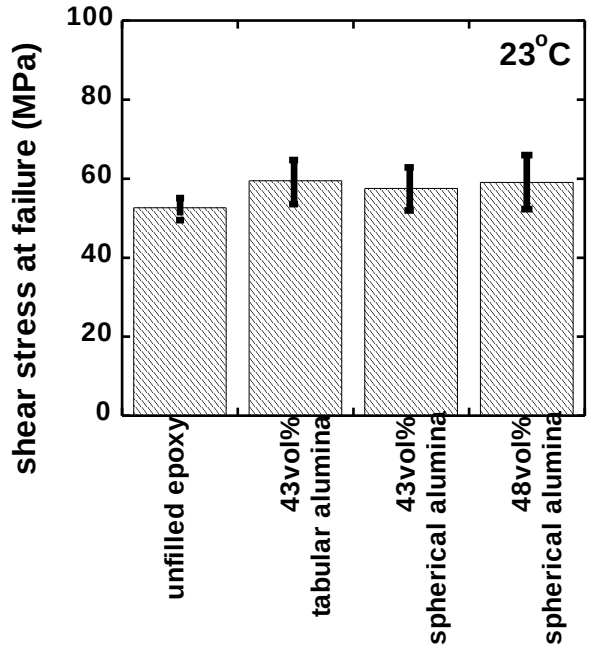

Figure 2-17: The napkin ring stress-to-fail is unaffected by filler particulates.

The GMB filled epoxy adhesive strengths were measured in this study with the napkin ring geometry at room temperature. The average critical shear traction, 45 ± 5 MPa, was slightly less than the average traction for the unfilled epoxy, 50 MPa. It was observed, however, that the GMB floated during processing creating a filler rich region at the napkin ring annulus, the initiation site for de-bonding. Therefore, the volume fraction of filler at the de-bonding interface was locally even greater than the nominal bulk loading level of 48vol%, which was already quite high. It is almost surprising that the de-bonding tractions for the GMB filled system are only 20% less than for the unfilled epoxy.

2.1.4 Linear Thermoelastic Response of Rigid Foams

A 20 lb/ft^3 density polyurethane foam (BKC 44307 cured at 71°C for 24 hrs) was also characterized in this study. The temperature dependent shear modulus was measured using an ARES rheometer in torsional rectangular geometry at a scan rate of 2°C/min. The linear CTE was measured with a thermomechanical analyzer at a scan rate of 2°C/min as well. The compressional modulus and apparent yield stress were measured at room temperature with an Instron 8825 at a displacement rate of 0.2 inch/min. The data are presented in Figure 2-18, Figure 2-19 and Figure 2-20 with linear thermoelastic properties shown at room temperature. Even though the foam does yield at roughly 5 MPa, no attempt was made to model the response with the nonlinear viscoelastic model since this phenomenon is highly localized. That is, at the apparent yield stress of foams, the material near the platens crushes severely while the remaining material is relatively undisturbed, and progressively more material crushes as the strain increases. This strain localization is due to buckling of foam walls and is not captured by the

nonlinear viscoelastic model. Even though the foam nonlinear response is complex, one may expect relatively low stresses due to its low modulus. Therefore, the material was initially modeled as linearly thermoelastic, and predictions of failure within the foam are more complicated than in the solid epoxies. Fortunately, foams rarely fail in thermal cycling since the low foam modulus generates minimal stress. In the subsequent finite element analyses, attention will be placed more on the effect that a foam has on the other materials in the simulation than on the stresses within the foam itself. The dynamic impact simulations proposed for following years will present more severe challenges.

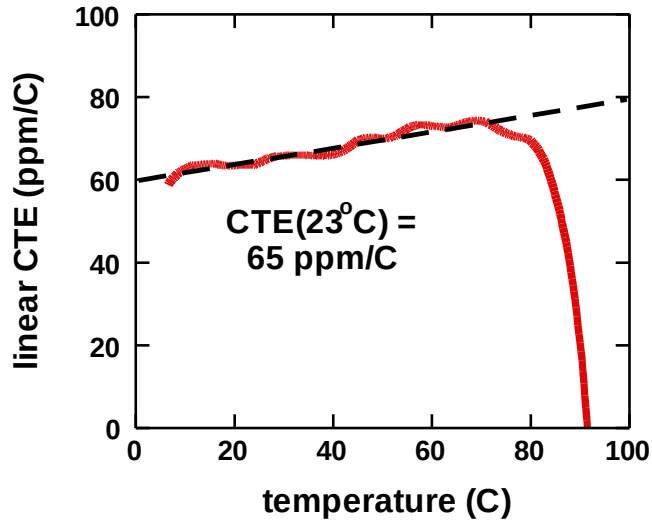

Figure 2-18: Linear CTE of the 20 lb/ft3 polyurethane foam.

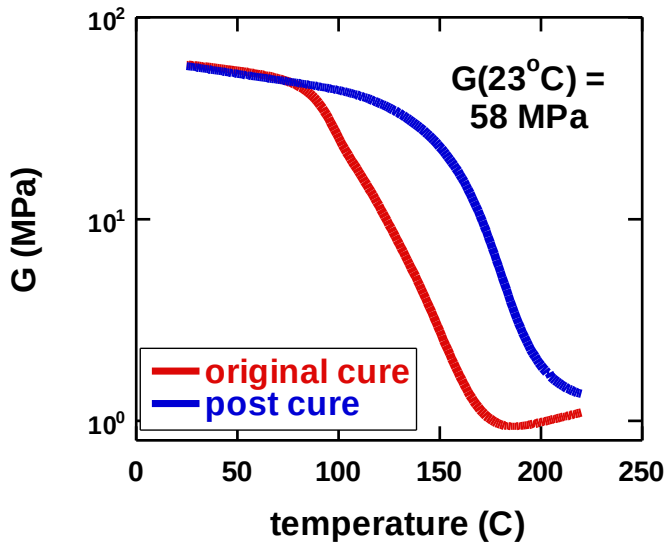

Figure 2-19: Shear modulus of the 20 lb/ft3 polyurethane foam.

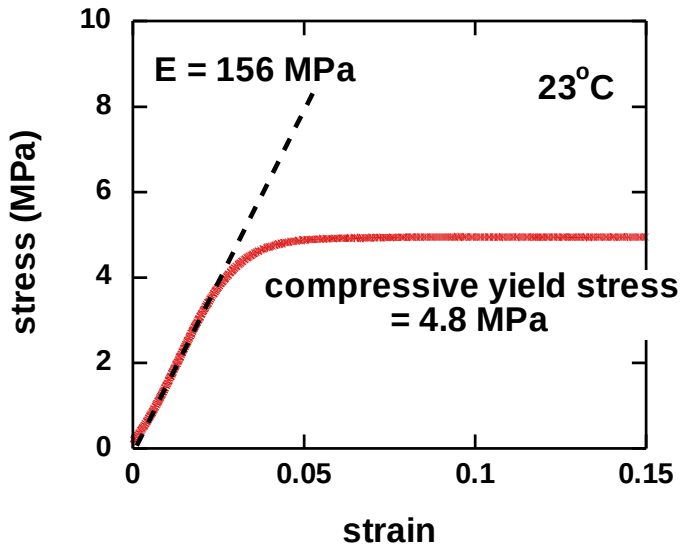

Figure 2-20: Young's modulus and compressive yield stress of the 20 lb/ft^3 polyurethane foam. From the shear and young's moduli, the Poisson's ratio is 0.33, which is typical for polymeric foams.

The precipitous decrease in foam CTE above 80°C is not reflective of the polymer but arises from instability of the foam structure as it increases above Tg for the first time. In fact, the Tg of the as-cured material is roughly 85oC, which is only slightly above the cure temperature as expected since vitrification quenches the reaction. As the foam is taken above 200oC during the test, further reaction is now possible, and the Tg of the fully cured foam rises to roughly 135oC. In actual components, the insulating properties of the foam coupled with the reaction exotherm can cause temperatures inside a large foam volume to increase above the oven temperature thereby creating a foam with variable Tg (i.e., higher in the middle).

2.2 Underfills

2.2.1 Characterization of the Underfills

Even though surface mount and underfill technology is mature in industry, its use in NW applications is relatively new. To date, the only underfill that has actually been used is Hysol FP0107, which is an alumina-filled epoxy (~20 vol% by thermogravimetric analysis) with Tg of roughly 65°C. The linear thermoelastic properties of this underfill using experimental equipment and conditions similar to those used to characterize the 828/DEA epoxy are shown in Figure 2-21 through Figure 2-25.

To expand our underfill options, a new family of filled epoxies was developed based on the diglycidyl ether of bisphenol A (Epon 828, Resolution Chemicals) cured with 32 phr of an aliphatic amine (Jeffamine D230, Huntsman Corp.) and filled with various volume fractions of a new glass microballoon (iM30k, 3M Corp.). The linear thermoelastic properties of the new underfills at 20, 30, and 40vol% iM30k are also shown in Figure 2-21 through Figure 2-25. Note that the unfilled 828/D230 epoxy has a Tg similar to the Hysol FP107 underfill. While the D32

GMB used in encapsulants has an average diameter of 50 microns and can have balloons as large as 100 microns, the iM30k GMB has an average diameter of 18 microns (0.7 mils) thereby making it more attractive for an underfill by decreasing the possibility of particle screening in the small gaps under surface mounted components. The particle size is not small enough, however, to cause aggregation and thereby adversely affect viscosity. In fact, the viscosity of the 828/D230/iM30k epoxy filled at 20vol% (comparable to Hysol) at 23oC immediately after mixing was slightly lower than the Hysol underfill (1.8 vs. 2.6 Pa-s). Figure 2-26 shows the viscosity of the iM30k underfill as a function of filler loading level.

A simple test for GMB screening was performed in which two glass slides were separated by a 2 mil spacer (the smallest anticipated underfill gap). Hysol and 20 vol% 828/D230/iM30k were dispensed on one side of the 1 inch wide top glass slide using a syringe. Both underfills quickly wicked completely under the slide, and samples were extracted from three locations for each material: the syringe, under the slide, and at the filling edge of the slide. If significant screening occurred, one would expect the slide to contain less GMB and the filling edge to contain more GMB than the nominal 20 vol% in the syringe. Figure 2-27 shows that weight losses measured by thermogravimetric analysis (Q800 TGA, TA instruments at a heating rate of 20°C/min) are not affected by location, so no screening is evident in either material.

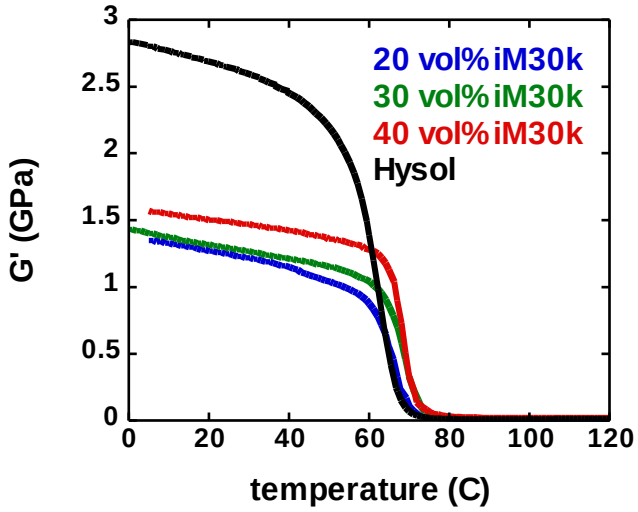

Figure 2-21: Temperature dependent shear moduli of the underfills.

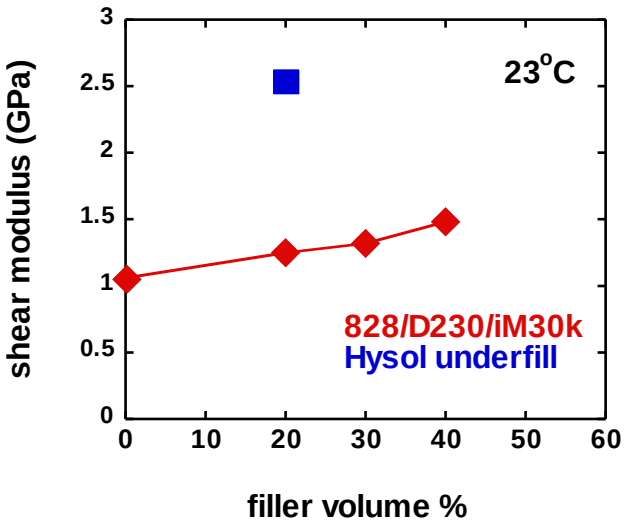

Figure 2-22: Room temperature moduli as a function of filler loading level.

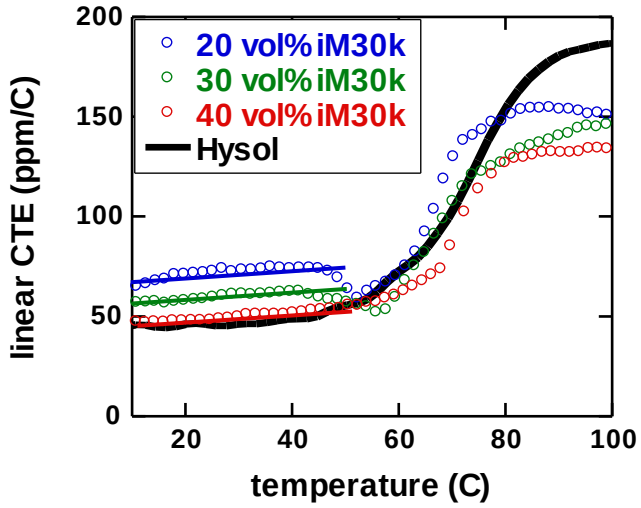

Figure 2-23: Temperature dependent CTEs of the underfills.

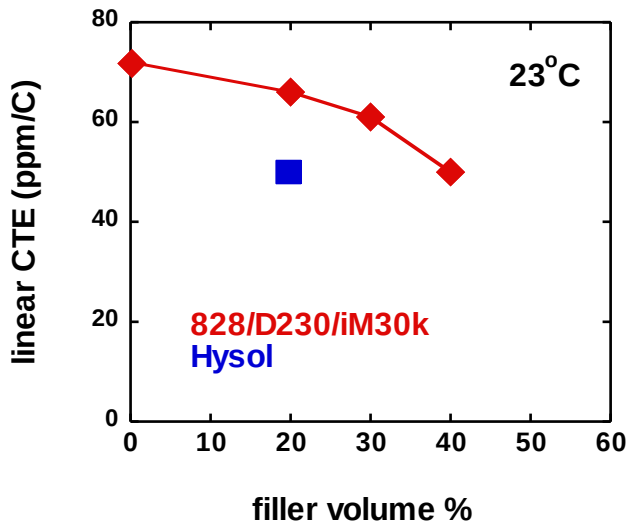

Figure 2-24: Room temperature CTEs as a function of filler loading level.

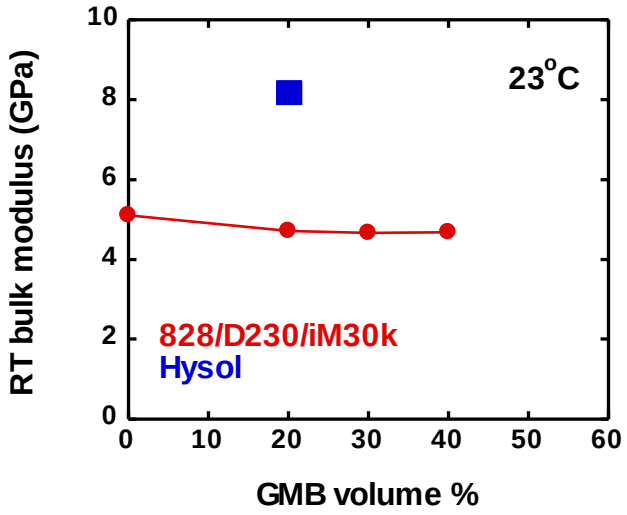

Figure 2-25: Room temperature bulk moduli as a function of filler loading level.

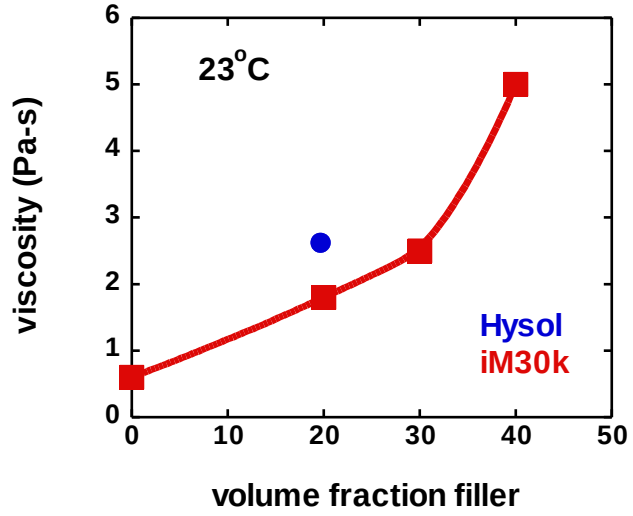

Figure 2-26: Room temperature viscosities of the new underfill at various volume fractions of iM30k compared to the historical Hysol underfill.

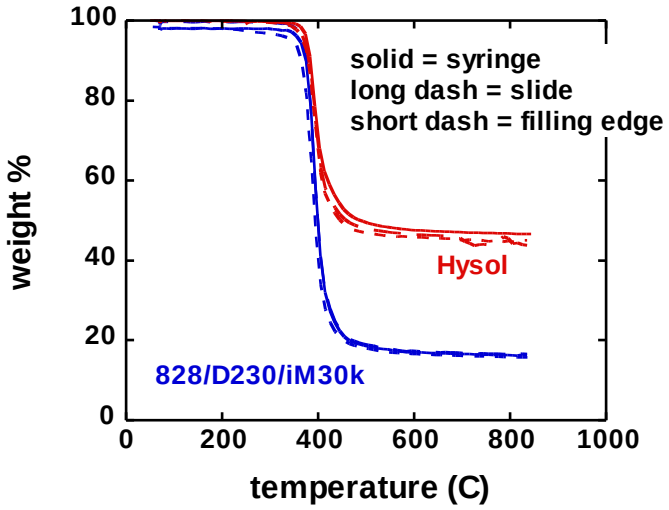

Figure 2-27: No screening of either underfill is evident. However, the weight remaining for the Hysol underfill is consistent with a particle loading level of 20 vol% (3.98 g/cc particle density) while the iM30k measured weight of 16% is larger than the calculated value of 12% based on the vendor supplied particle density of 0.6.

The unfilled 828/D230 epoxy was more extensively characterized, and the responses were fit quantitatively with the nonlinear viscoelastic SPEC model. The model parameters are given in Table 2-4. The measured and predicted master curve (ARES, TA Instruments using torsional rectangular geometry and 5oC increments) at the reference temperature of 85oC and

linear CTE are shown in Figure 2-28 and Figure 2-29. Nonlinear responses for tensile creep and yield (1125 load frame, Instron Corp. at a strain rate of 10%/min) are shown in Figure 2-30 and Figure 2-31. The measured cooling rate of the samples shown in Figure 2-32 was used in the SPEC predictions to define the initial state of the material prior to testing.

Table 2-4: Nonlinear viscoelastic model parameters for the 828/D230 epoxy.

variable	value	units
T_{ref}	85	^oC
K_∞ at T_{ref}	3.29	GPa
dK_∞/dT	-12	MPa/^oC
linear α_∞ at T_{ref}	213	ppm/^oC
$d\alpha_\infty/dT$	0.083	ppm/$^oC^2$
G_∞ at T_{ref}	7.4	MPa
dG_∞/dT	0	MPa/^oC
K_g at T_{ref}	4.9	GPa
dK_g/dT	-12	MPa/^oC
linear α_g at T_{ref}	60	ppm/^oC
$d\alpha_g/dT$	0.1	ppm/$^oC^2$
G_g at T_{ref}	0.854	GPa
dG_g/dT	-2.8	MPa/^oC
C_1	15	
C_2	55	^oC
C_3	9000	
C_4	19,000	Pa
τ_s	0.40	sec
β_s	0.28	
τ_v	6	sec
β_v	0.14	

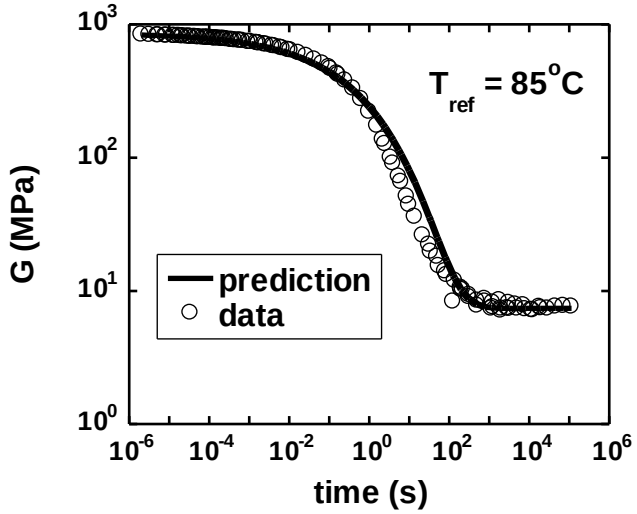

Figure 2-28: Measured and predicted master curves for the 828/D230 epoxy at Tref.

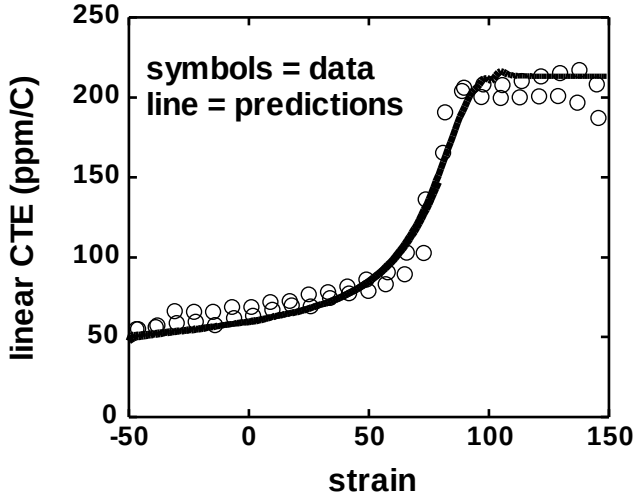

Figure 2-29: Measured and predicted linear CTEs for the 828/D230 epoxy.

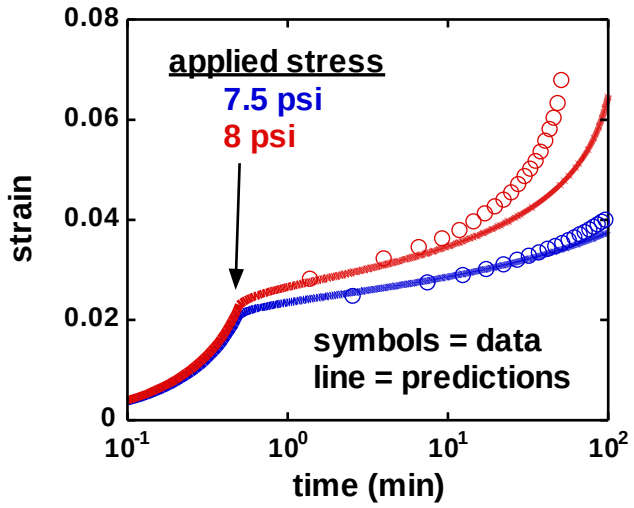

Figure 2-30: Measured and predicted tensile creep for the 828/D230 epoxy at 23°C.

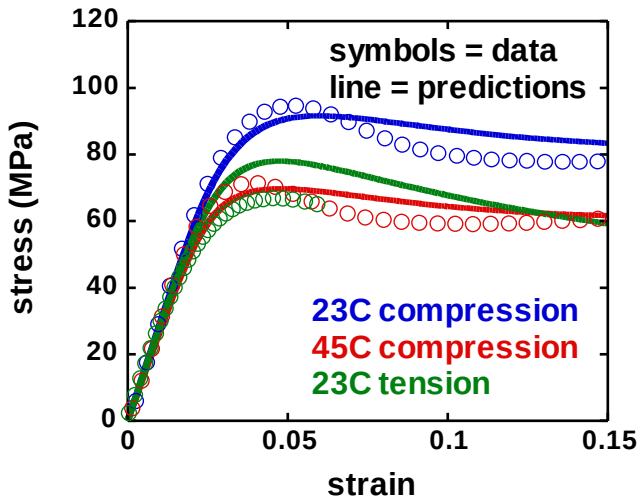

Figure 2-31: Measured and predicted yield in compression and tension at various temperatures for the 828/D230 epoxy.

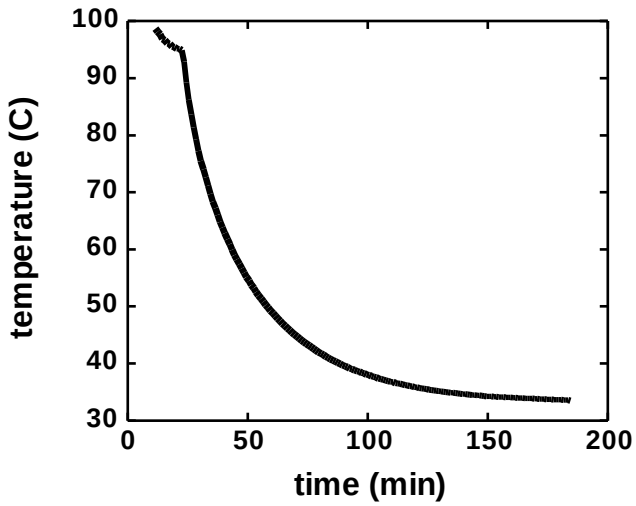

Figure 2-32: Cooling profile measured and used for predictions of nonlinear response for the 828/D230 epoxy.

2.2.2 Generic Nonlinear Viscoelastic Model for Epoxies

Numerous approaches have been developed to predict properties of pure polymers.[8,9] Start by examining the volumetric CTE. The glassy CTE of polyethylene terephthalate (PET, soda bottles) just below Tg (~72°C) is roughly 150 ppm/C whereas the corresponding CTE of polypropylene (Tg ~ -7°C) is roughly 350 ppm/C, which is quite a difference. Attempts to fit the data phenomenogically have been moderately successful.[9]

$$\alpha_g = \frac{1}{T + 9.47Tg} \quad \rightarrow \quad \alpha_g(Tg) = \frac{1}{Tg + 9.47Tg} = \frac{0.0955}{Tg} \qquad (2.4)$$

where Tg is expressed in units of K.

However, if attention is focused on a much more limited set of materials, crosslinked epoxies, while ignoring thermoplastics and semi-crystalline polymers, the variation in CTE is much less dramatic. A wide variety of curatives listed in Table 2-5 were used to crosslink the 828 epoxy resulting in cured Tgs differing by almost 150°C. The volumetric CTEs of these epoxies just below Tg are presented in Figure 2-33 and predicted with Eq. 2.4. For this wide range of curatives, a constant CTE predicts the data as well as Eq. 2.4.

Table 2-5: Nonlinear viscoelastic model parameters for a "generic" unfilled epoxy.

system	source	curative	Tg (^{o}C) by TMA
1	May[10]	metaphenylenediamine	190
2	May	methylenebis(o-chloroaniline)	149
3	May	boron trifluoride-amine complex	141
4	May	diethylenetriamine	122
5	SNL	curing agent "Z" (aromatic amines)	115
6	SNL[2]	TCR 3325	100
7	SNL	D230/Ancamine2049 (a cycloaliphatic amine)	90
8	SNL	diethanolamine	65
9	SNL	D230	75
10	May	aliphatic diamine	47

Figure 2-34 shows similar results for the glassy moduli of these systems measured just below their respective Tgs. Again, a constant value fits the data reasonably well. The temperature dependent compressive yield stresses for a subset of the epoxies are plotted against the temperature difference from Tg in Figure 2-35. While it is clear and expected that the yield stress should vary with temperature, there is no obvious difference between the various curatives ranging from aromatic amines to aliphatic amines to alcohols.

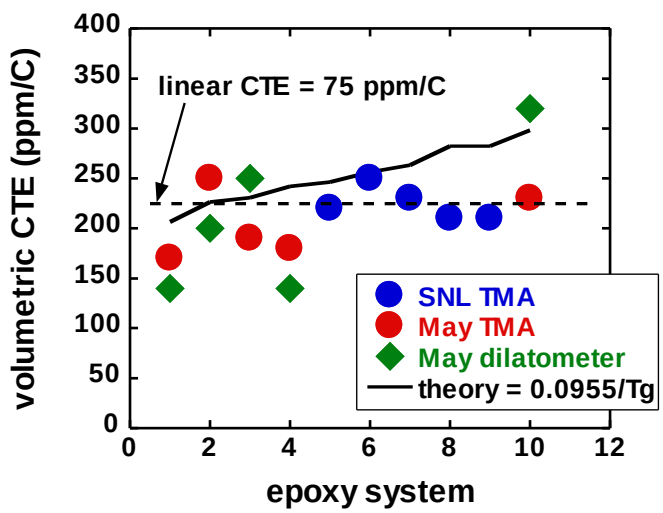

Figure 2-33: Volumetric CTEs in the glass just below Tg for the epoxies listed in Table 2-5.

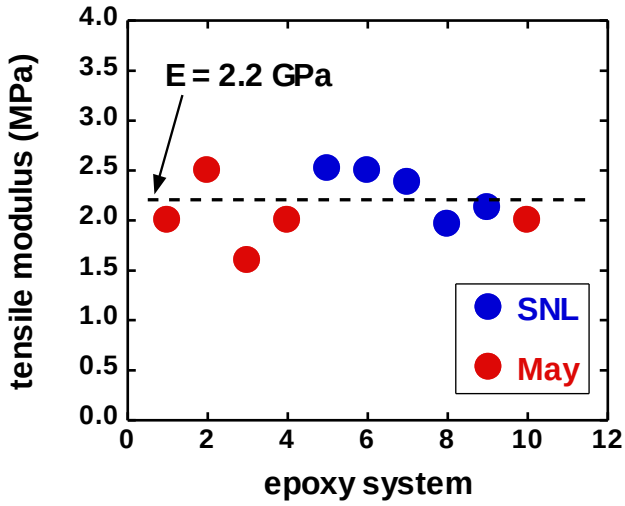

Figure 2-34: Tensile moduli in the glass just below Tg for the epoxies listed in Table 2-5.

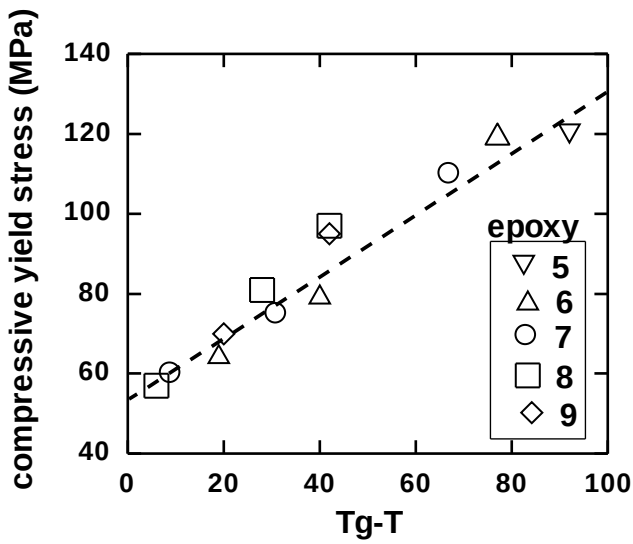

Figure 2-35: Compressive yield stresses in the glass just below Tg for the epoxies listed in Table 2-5.

Therefore, as a rough approximation, the nonlinear viscoelastic properties of the unfilled epoxies that would be input into the SPEC model should be identical except for the reference temperature (e.g., Tg), and the properties given in Table 2-4 for the 828/D230 system could be used. While some differences will exist between systems, the major effect of Tg setting the stress-free temperature for thermal cycling stress predictions should be dominant. For the simple screening tests envisioned in this study to determine trends for identifying the optimal material choices and design strategies, this simple approach is sufficient. Fillers, however, can greatly

affect the effective underfill properties, and methods to determine filler type and loading levels are discussed in the following sections.

2.2.3 Generic Nonlinear Viscoelastic Model for Epoxies with Hard Fillers

Since the properties of unfilled epoxies normalized to Tg were shown to be similar, one wonders if some similar approximation can be employed for filled systems. While theories abound for estimating the effect of fillers on polymer properties, simple and surprisingly accurate bounds on the bulk, K, and shear, G, moduli were determined by Hill[11] and Hashin and Shtrikman[12] decades ago. The lower bounds typically match experimental data better and are given by

$$K = K_e + \frac{\phi(K_f - K_e)}{1 + (1-\phi)\dfrac{(K_f - K_e)}{(K_e + 4G_e/3)}} \qquad (2.5)$$

$$G = G_e + \frac{\phi(G_f - G_e)}{1 + \beta(1-\phi)\left(\dfrac{G_f}{G_e} - 1\right)} \qquad (2.6)$$

$$\text{where} \quad \beta = \frac{2(K_e + 2G_e)}{5(K_e + 4G_e/3)}$$

and the subscripts f and e refer to the filler and epoxy respectively and ϕ is the filler volume fraction. These equations imply, not surprisingly, that the effective composite moduli depend on the ratios of the individual filler and epoxy moduli. However, the composite moduli become independent of the filler moduli when they become much greater than the epoxy moduli. In this limit of "hard" fillers and assuming the epoxy bulk modulus is large compared to its shear modulus, Eqs. 2.5 and 2.6 reduce to

$$K = \frac{K_e}{(1-\phi)} \qquad (2.7)$$

$$G = G_e\left(\frac{1+\phi}{1-\phi}\right) \qquad (2.8)$$

where a typical value of β=1/2 has been assumed for the glassy epoxy.

The predictions of Eqs. 2.5 and 2.6 are plotted in Figure 2-36 assuming a silica filler (K=37 GPa, G=31 GPa). Silica would probably be the "softest" of the "hard" fillers having a bulk modulus roughly 8 times the epoxy bulk modulus. The bulk modulus of alumina fillers, by contrast, is 165 GPa making it truly "hard" filler. Even for silica at a volume loading of 50%, the bulk modulus from Eq. 2.5 is 9.5 GPa whereas the prediction from Eq. 2.7 is 10 GPa assuming an epoxy bulk modulus of 5 GPa. Also plotted in Figure 2-36 are experimental moduli from

several SNL systems listed in Table 2-6 and measured roughly 70°C below each system's Tg. The simple results of Eqs. 2.5 and 2.6 do a very reasonable job of matching the data.

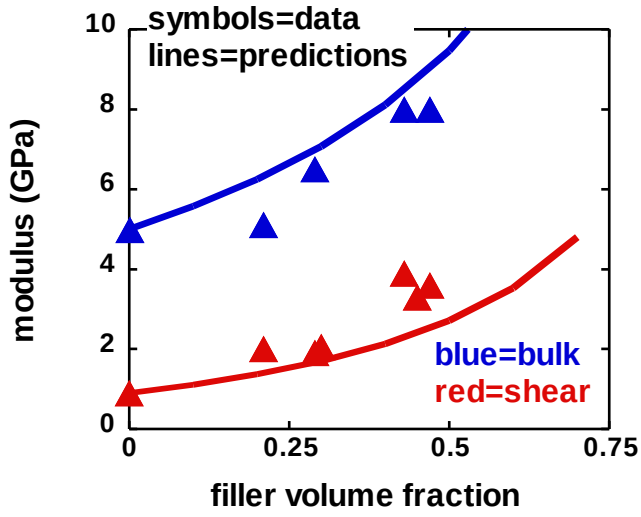

Figure 2-36: Bulk and shear moduli predicted by Eqs. 5 and 6 and measured on the SNL systems listed in Table 2-6.

Table 2-6: Elastic properties for filled epoxy systems measured roughly 70°C below Tg.

system	G (GPa)	K (GPa)	linear CTE (ppm/C)	filler vol.%
828/DEA	0.9	5	60	0
828/D230/alumina	2	5.11	44	21
828/Z/mica	1.9	6.5	38	29
828/DEA/silica	2.05		38	30
828/Z/alumina	3.9	8	25	43
828/DEA silica	3.3		28	45
828/D230/2049/alumina	3.6	8	28	47

Eq. 2.7 states that, in the limit of hard fillers, the composite bulk modulus depends on the quantity (1-ϕ) in a power law fashion. Figure 2-37 suggests that this power law relationship could be used to fit both bulk and shear data phenomenologically. The exponent for the bulk modulus data appears to be roughly the same as the theoretical value of -1. The apparent theoretical exponent for the shear modulus using Eq. 2.8 is -1.5 while the data are bounded by an exponent of -2.5.

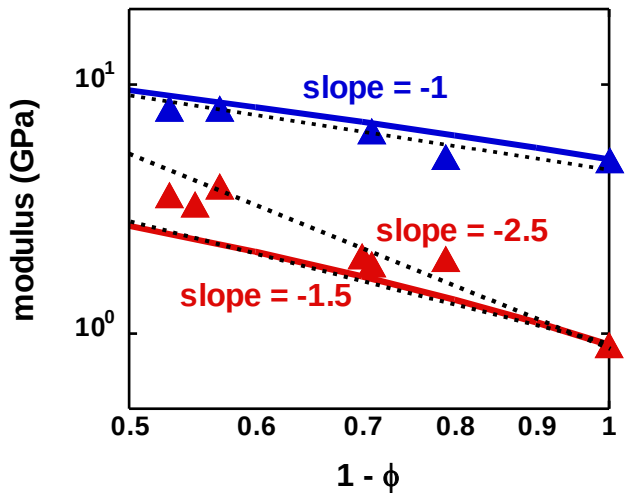

Figure 2-37: Results from Figure 2-36 now plotted logarithmically.

Similarly, a simple rule of mixtures law for the composite CTE reduces to the same power law form in the limit of a filler with negligible CTE compared to the epoxy matrix.

$$\alpha = \alpha_e(1-\phi) + \alpha_f\phi \;\rightarrow\; \alpha_e(1-\phi) \qquad (2.9)$$

CTEs predicted by the limit of Eq. 2.9 and measured at roughly 70°C below Tg for various SNL systems are plotted logarithmically in Figure 2-38 and listed in Table 2-6. The apparent power law exponent for the data is roughly 1.3.

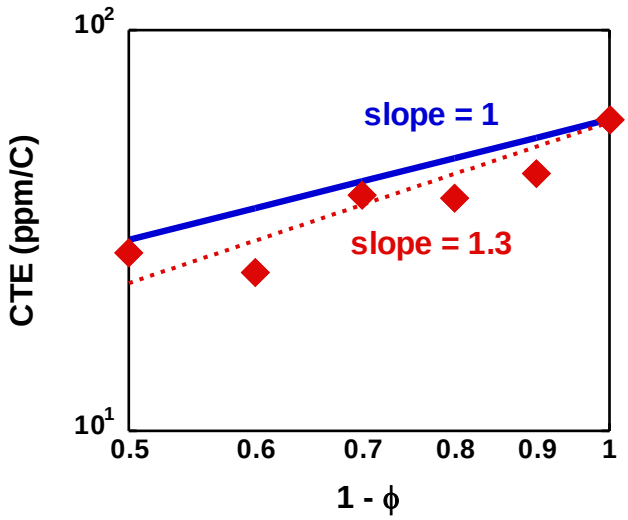

Figure 2-38: CTEs of the filled epoxies listed in Table 2.6 and the predicted values from the rule of mixtures.

In general, the power law function seems to provide a very simple and fairly accurate phenomenological relationship for estimating the elastic properties of filled epoxies.

$$\Psi = \Psi_e (1-\phi)^x \qquad (2.10)$$

for all properties, Ψ. For simulations to be discussed later, it will be more important to predict consistent stress trends as filler fraction is increased rather than to predict precisely the exact value of the stress. Such trends allow us to identify classes of underfills that will perform best in specific applications (e.g., unfilled vs. highly filled). Therefore, the fits provided by Eq. 2.10 are adequate for our purposes.

The SPEC nonlinear viscoelastic model required inputs from Table 2-2 also include the reference temperature (essentially Tg) and the WLF coefficients, C_1 and C_2.[13] However, the effect of hard, large (>1 micron) fillers on the shape of the relaxation spectra and the temperature shifts is negligible.[13] This leaves only the filler fraction dependence of the model parameters, C_3 and C_4, in the "material clock" to be defined. As discussed in Ref. 4, these parameters are approximated by

$$C_3 \approx \frac{T_{ref}\left[K_g\alpha_g - K_\infty\alpha_\infty\right]}{\rho_{ref}\left[C_{P_\infty} - C_{P_\infty}\right]} \qquad (2.11)$$

$$C_4 \approx -\frac{\left[G_g - G_\infty\right]}{\rho_{ref}\left[C_{Pg} - C_{P\infty}\right]} \qquad (2.12)$$

where C_{Pg} and $C_{P\infty}$ are the glassy and rubbery constant pressure heat capacities respectively (cal/g). The rule of mixtures is widely applied to the heat capacity and will be used here

$$\begin{aligned} C_{Pg} - C_{P\infty} &= \left[C_{Pg}^e(1-\omega) + C_P^f\omega\right] - \left[C_{P\infty}^e(1-\omega) + C_P^f\omega\right] \qquad (2.13) \\ &= \left[C_{Pg}^e - C_{P\infty}^e\right](1-\omega) = \left[C_{Pg}^e - C_{P\infty}^e\right]\frac{\rho_{ref}^e}{\rho_{ref}}(1-\omega) \end{aligned}$$

where ω is the filler weight fraction. Accepting the experimental exponents for K, α, and G as -1, 1.3, and -2.5 respectively, the filler fraction dependencies of C_3 and C_4 using Eq. 2.13 are

$$C_3 \sim (1-\phi)^{-0.7} \quad \text{and} \quad C_4 \sim (1-\phi)^{-3.5} \qquad (2.14)$$

In practice, values of 0 and -3.75 seemed to predict temperature dependent yield stresses more accurately and are listed in Table 2-7 with all other exponents used in calculations performed in this study for epoxies with hard particulate fillers.

Table 2-7: Filler exponents from Eq. 2.10 used for the nonlinear viscoelastic model inputs of an epoxy filled with hard particulates.

variable	filler exponent, x
T_{ref}	0
K_∞ at T_{ref}	-1
dK_∞/dT	-1
linear α_∞ at T_{ref}	1.3
$d\alpha_\infty/dT$	1.3
G_∞ at T_{ref}	-2.5
dG_∞/dT	-2.5
K_g at T_{ref}	-1
dK_g/dT	-1
linear α_g at T_{ref}	1.3
$d\alpha_g/dT$	1.3
G_g at T_{ref}	-2.5
dG_g/dT	-2.5
C_1	0
C_2	0
C_3	0
C_4	-3.75
τ_s	0
β_s	0
τ_v	0
β_v	0

Predictions for the compressive yield stress of the 828/DEA epoxy filled with 30 and 45 vol% silica beads (shown previously in Figure 2-5 and Figure 2-6 where the SPEC model was fitted to those particular systems) are shown in Figure 2-39 and Figure 2-40 now using the pure 828/DEA properties[4] modified by Eq. 2.10 and the exponents of Table 2-7. The predictions using the generic filler model of Table 2-7 are not significantly degraded from the best model fits. Most noticeably, the yield stress predictions are comparable but the post-yield softening is more pronounced in the generic fit.

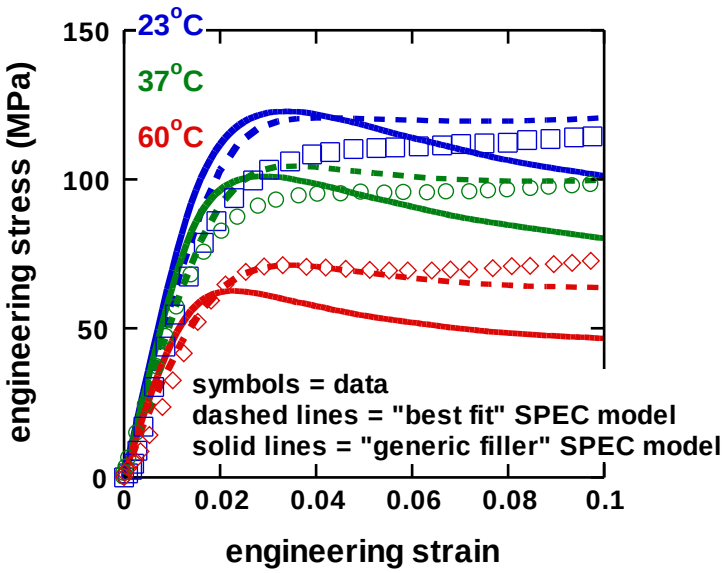

Figure 2-39: Measured and predicted compressive yield stresses for the 828/DEA epoxy filler with 30 vol% silica beads.

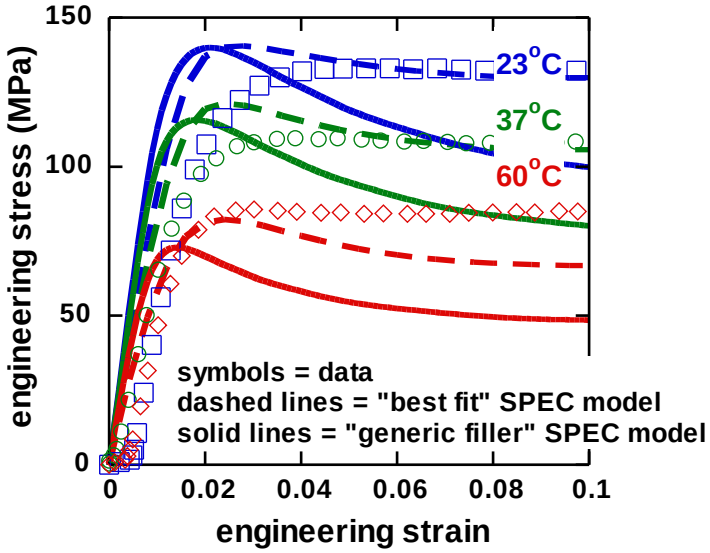

Figure 2-40: Measured and predicted compressive yield stresses for the 828/DEA epoxy filler with 45 vol% silica beads.

Predictions of cohesive and adhesive failure would use the previously discussed metric of a critical maximum principal strain. For these hard fillers, a convenient value for the finite element codes might be 10%, which is probably a bit low for predicting actual failure, but avoids convergence issues and certainly portends failure.

2.2.4 Generic Nonlinear Viscoelastic Model for Epoxies with the iM30k Filler

The properties of the 828/D230/iM30k GMB system were presented previously in Section 2.2.1 and are now plotted logarithmically in Figure 2-41 through Figure 2-43 as the red (glassy) and blue (rubbery) curves. The power law relationship of Eq. 2.10 used for hard fillers seems to apply equally well for this iM30k GMB filled epoxy, and the resulting fitted exponents are listed in Table 2-8. It is clear from comparing the values in Table 2-7 and Table 2-8 that the GMB filler produces quite different composite properties than from hard fillers. While the GMB decreases the dependence of CTE on filler fraction only slightly, the effect on the bulk and shear moduli is dramatic. The bulk modulus is almost independent of iM30k fraction while the exponent from Eq. 2.10 for the glassy shear modulus is decreased from a large value of -3 to a quite small value of -0.5. At a quick glance, then, a hard filler decreases the CTE with increasing filler fraction but increases the modulus even faster. The iM30k filler, again at a quick glance, decreases the CTE with increasing filler fraction but has little effect on the moduli.

Properties for the D32 GMB filled 828/DEA epoxy are also shown in Figure 2-41 through Figure 2-43 in black, and the fitting exponents used in Eq. 2.10 for this system are also listed in Table 2-8. The density of the D32 GMB is 0.32 g/cc while the iM30k GMB density is 0.6 g/cc. The relatively thinner walls of the D32 balloons exaggerates the trends in shear and bulk modulus seen for the iM30k filled epoxies; the shear modulus is now independent of the D32 loading level, and the bulk modulus actually decreases with increasing filler fraction, which is the opposite trend predicted by Eq. 2.7 for hard fillers. GMB filled epoxies are seen to offer an interesting family of underfills to examine in computational stress simulations giving properties much different from underfills with hard particulates. Table 2-8 lists not only the experimental exponents for the iM30k and D32 GMB but "averaged" exponents used in the stress simulations discussed later.

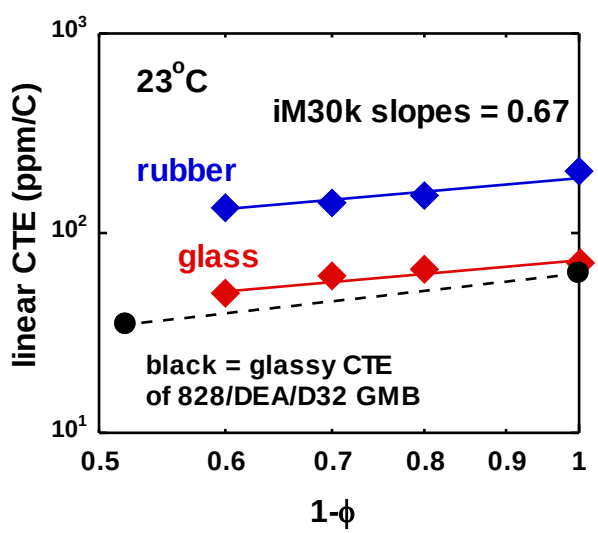

Figure 2-41: Linear CTEs of the iM30k filled epoxy plotted logarithmically.

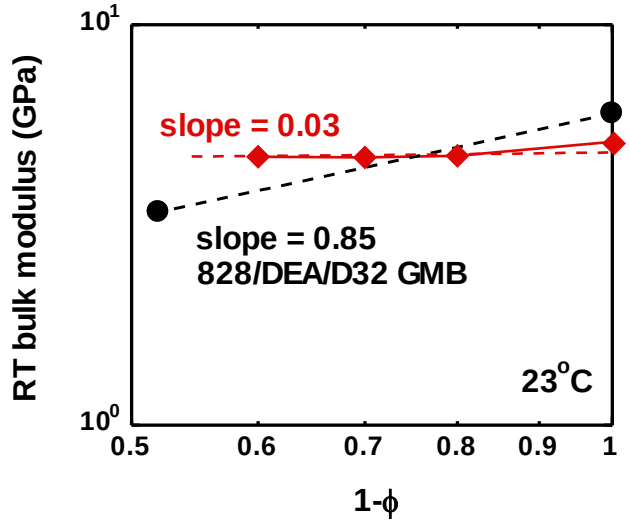

Figure 2-42: Glassy bulk moduli of the iM30k filled epoxy plotted logarithmically.

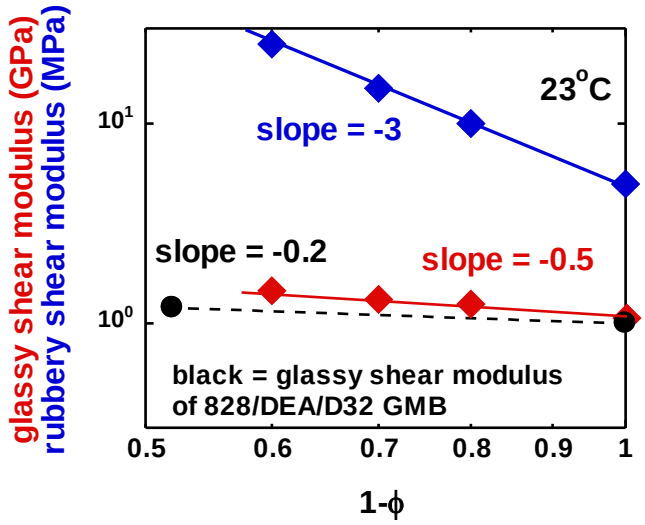

Figure 2-43: Shear moduli of the iM30k filled epoxy plotted logarithmically.

Table 2-8: Filler exponents from Eq. 2.10 for the GMB filled epoxies.

variable	experimental iM30k exponent, x	experimental D32 exponent, x	generic exponent, x, used in simulations
K_∞ at T_{ref}	0	0.8	0
dK_∞/dT	0	0.8	0
linear α_∞ at T_{ref}	0.67	0.9	0.67
$d\alpha_\infty/dT$	0.67	0.9	0.67
G_∞ at T_{ref}	-3	-3	0
dG_∞/dT	-3	-3	0
K_g at T_{ref}	0	0.8	0
dK_g/dT	0	0.8	0
linear α_g at T_{ref}	0.67	0.9	0.67
$d\alpha_g/dT$	0.67	0.9	0.67
G_g at T_{ref}	-0.5	-0.2	0
dG_g/dT	-0.5	-0.2	0
C_1	0	0	0
C_2	0	0	0
C_3	-0.33	0.7	0
C_4	-1.5	-1	0
τ_s	0	0	0
β_s	0	0	0
τ_v	0	0	0
β_v	0	0	0

Failure in these GMB filled underfills would again be predicted by a critical value of the maximum principal strain, which would reside between 5 and 10%.

2.3 Coatings

Elastomeric coatings are often used to coat components on printed circuit boards, although the reasons for their use are often not fully understood. One may be worried about stresses generated from CTE mismatches during thermal cycles causing changes in the performance of individual components (e.g., changes in capacitance from thermal stresses). Perhaps coatings will mitigate shock to the components. Coatings in unencapsulated applications might prevent dielectric breakdown (i.e., arcing), minimize tin whisker growth in lead free solders, prevent environmental contamination, or protect delicate wires from handling abuse. In the stress simulations presented later, we will investigate the effect of coatings on component and underfill stresses and solder fatigue life during thermal cycles to understand if coatings are needed and

what coating properties are optimal. Later simulations will address similar issues in dynamic loading.

2.3.1 Unfilled Silicone

A very simple coating could be an unfilled silicone such as Sylgard 184 (Dow Corning). This is a typical vinyl terminated polydimethylsiloxane cured with a Pt catalyzed silane. The linear thermoelastic properties are shown in Figure 2-44 through Figure 2-47 for samples cured 16 hrs at 70°C. The CTE was again measured with the Q500 TMA, the shear modulus with the ARES using torsional rectangular geometry, and the bulk modulus using a pressure vessel (imparting a hydrostatic stress) with a strain-gauged cylindrical sample. Two strain gauges were used on opposing sides of the sample, and the differences in the two readings arise from a small tilt in the sample faces. Therefore, the averaged reading (dashed line) was used to extract the bulk modulus. The Young's moduli were measured with the 1125 Instron in dogbone (tension) and cylindrical (compression) geometries. In tension, the sample was continuously stretched to failure, but in compression, a ratcheted strain history was applied (straining to 20%, returning to zero, and the re-compressing to 60% strain) to assess the viscoelastic contribution. In shear, the upturn in modulus at roughly -40°C does not arise from the glass transition but from the well-known partial crystallization of the polydimethylsiloxane. Other commercial siloxanes prevent crystallization by incorporating polyphenylmethylsiloxane, which is somewhat more expensive.

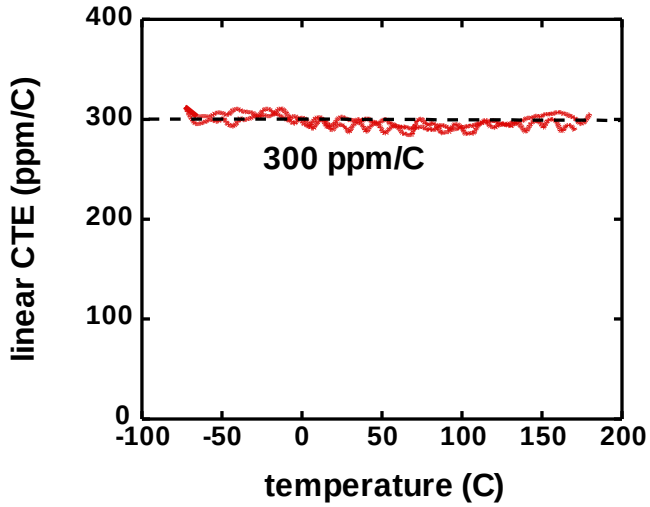

Figure 2-44: Linear CTE of the Sylgard elastomer.

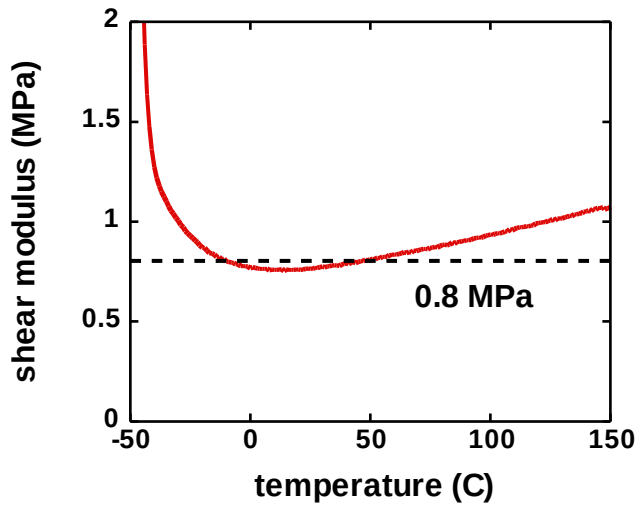

Figure 2-45: Temperature dependent linear shear modulus of the Sylgard elastomer.

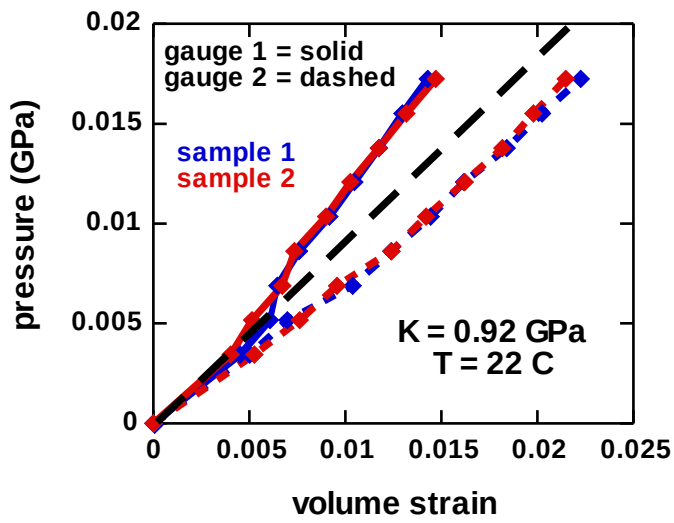

Figure 2-46: Room temperature bulk modulus of the Sylgard elastomer.

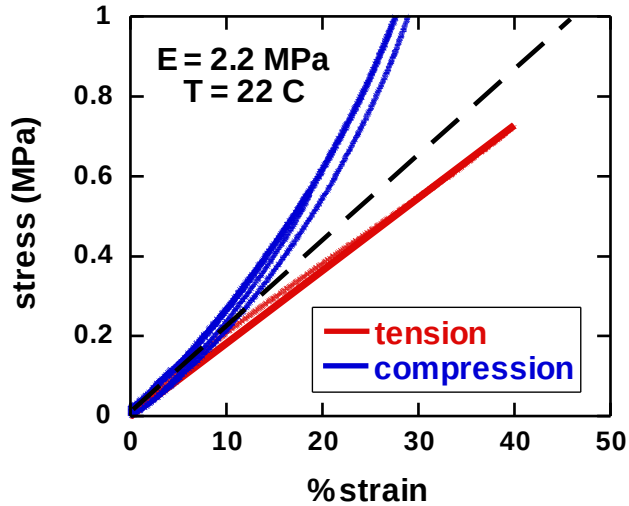

Figure 2-47: Room temperature Young's modulus of the Sylgard elastomer from tension and compression tests.

The curvature in the compressive test results is not necessarily an intrinsic material nonlinearity. A simple neo-Hookean free energy (Eq. 2.15) naturally produces such curvature at finite strains. The neo-Hookean uniaxial Cauchy stress (assuming incompressibility) given in Eq. 2.16 accurately predicts the experimental Sylgard uniaxial response (Figure 2-48). The small viscoelastic hysteresis seen in the ratcheted compression test is negligible and ignored.

$$W = \frac{G}{2}\left(\bar{I}_1 - 3\right) + K\left(J-1\right)^2 \quad \text{where } \bar{I}_1 = J^{-2/3}\,\mathrm{tr}\left(\underline{\underline{C}}\right) \text{ and } J = \det\left(\underline{\underline{F}}\right) \tag{2.15}$$

$$\sigma = G\left(\lambda - \frac{1}{\lambda^2}\right) \tag{2.16}$$

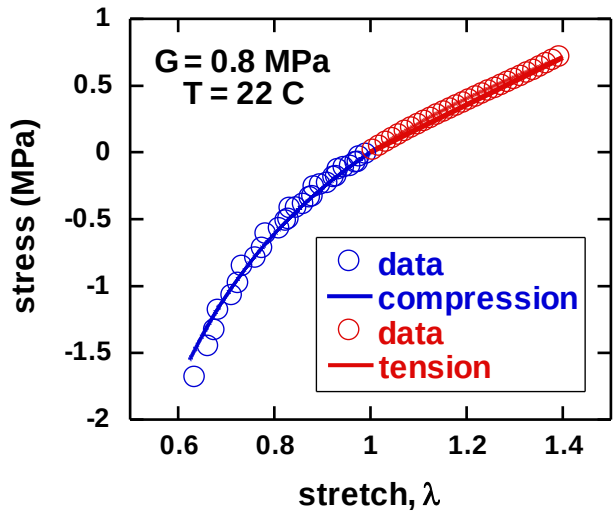

Figure 2-48: A simple neo-Hookean model predicts the uniaxial data accurately.

Beyond determining the thermoelastic properties for Sylgard, it is useful to obtain estimates for failure both cohesive and adhesive. The dogbone tensile test in Figure 2-47 and Figure 2-48 was taken to failure. Failure did occur in the gauge region at a stress of 0.73 MPa and strain of 40%. The silicone was also bonded to the stainless steel napkin ring fixtures discussed in Section 2.1.3. The failures were adhesive in three repeats, and the average stress at de-bonding was 0.5 ± 0.05 MPa. Therefore, adhesive failure precedes cohesive failure, not surprisingly, in these silicones by a considerable margin. Since the temperature dependence of the silicone properties is relatively minimal, a constant value of 0.5 MPa would be a reasonable value that signifies de-bonding. Ideally within the finite element codes, the surface tractions would be compared with this critical value. However, a much simpler approach would involve examination of the stresses normal to a surface in the adjacent element.

2.3.2 Unfilled Polysulfide

Other elastomers typically used at Sandia are electrical grade polysulfides. For this study, an unfilled polysulfide, CS3100 (Flamemaster Corp.), cured at 70°C for 6 hrs was characterized. Unlike silicones with relatively low viscosities, the polysulfides are quite viscous and cannot be degassed after mixing. The CTE and moduli were measured using the techniques described for Sylgard, and the results are shown in Figure 2-49 through Figure 2-52. Except for the bulk modulus, CS3100 and Sylgard 184 appear similar, and the neo-Hookean model of Eq. 2.16 predicts the room temperature, high strain Young's modulus well (Figure 2-53). The bulk moduli for two samples shown in Figure 2-51 display two distinct responses. The initial response up to roughly 2% volumetric strain is quite compliant while the higher strain response gives a typical bulk modulus for rubber polymers. It appears that voids (~2% by volume) are trapped in the polysulfide during mixing and, due to its high viscosity, cannot be eliminated by degassing. Only when these voids are completely collapsed can the compressibility of the pure polymer be probed.

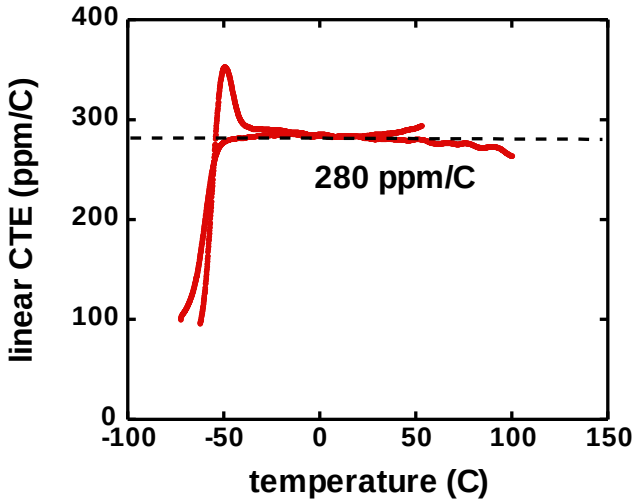

Figure 2-49: Linear CTE of the CS3100 polysulfide.

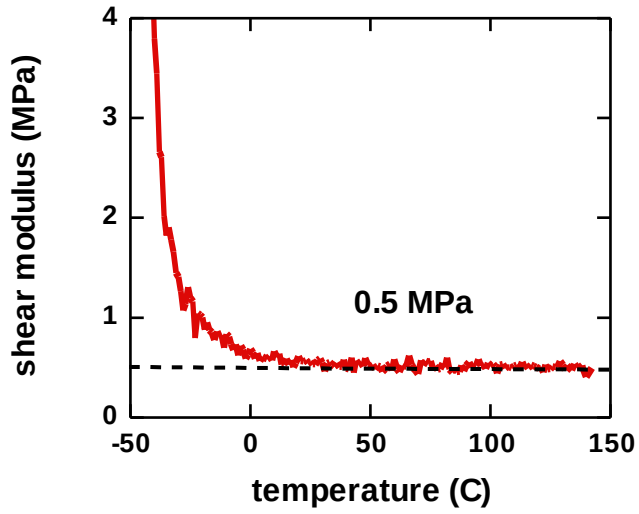

Figure 2-50: Temperature dependent linear shear modulus of the CS3100 polysulfide.

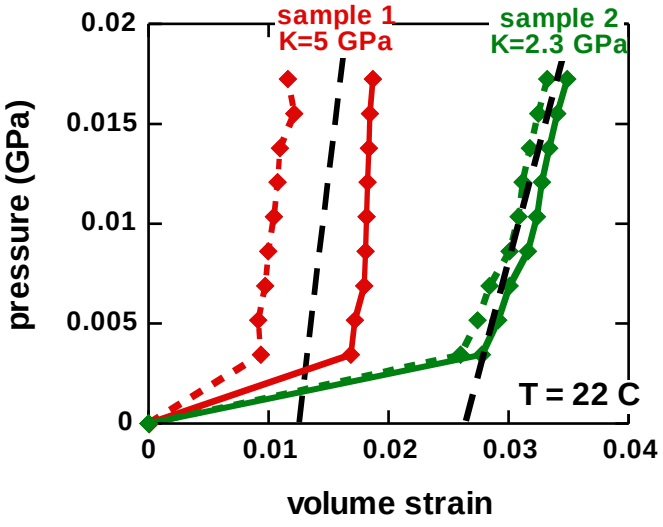

Figure 2-51: Room temperature bulk modulus of the CS3100 polysulfide.

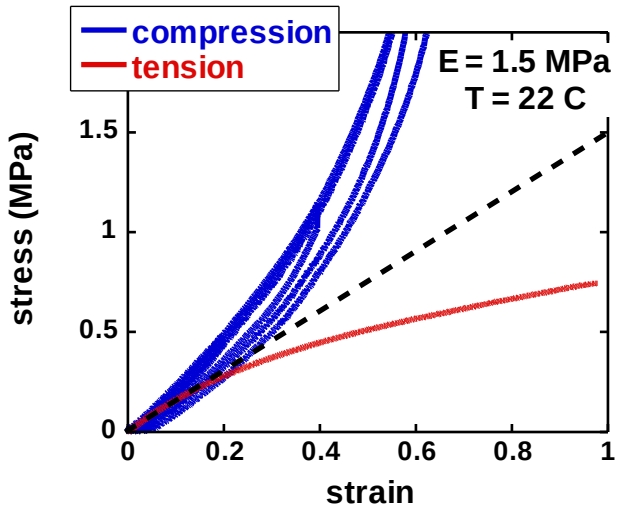

Figure 2-52: Room temperature Young's modulus of the CS3100 polysulfide from tension and compression tests.

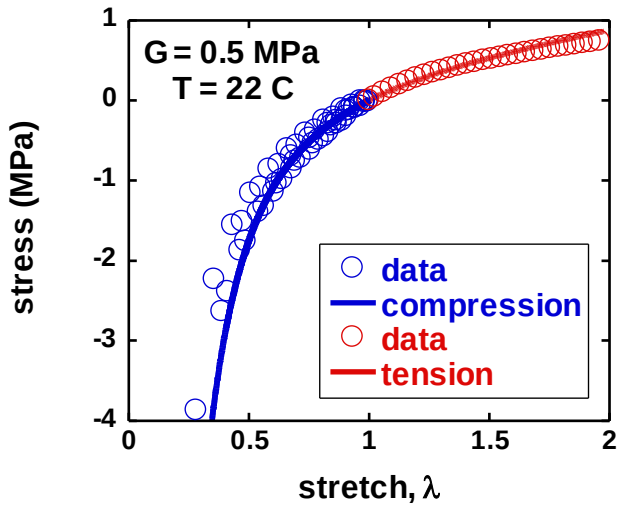

Figure 2-53: A simple neo-Hookean model predicts the uniaxial data accurately.

Measurements of the room temperature shear adhesive strength of the CS3100 were attempted using the napkin ring test giving a value of 1.30 ± 0.14 MPa; however, the failures were cohesive (Figure 2-54). For comparison, the stress at failure of the tensile dogbone was 0.75 MPa. Two butt tensile samples of CS3100 were prepared on stainless steel plugs (1.25" diameter and 60 mil gap) to assess failure in a different geometry. Failure again appeared to be cohesive (Figure 2-55) with a stress at failure of 0.81 ± 0.09 MPa. Since the CS3100 is elastic, failure stresses and strains are uniquely related, so either metric can be used in stress simulations, and a value of roughly 1 MPa for the maximum principal stress appears critical and, again, rather temperature insensitive.

Figure 2-54: Failure in the napkin ring geometry visually appears cohesive.

Figure 2-55: Failure in butt tensile geometry also appears cohesive.

2.3.3 GMB-Filled Silicone

Just as GMB filler is added to epoxies, it can be added to elastomers as well. A historical Sandia formulation with Sylgard 184 uses 8.3 wt% of a different GMB (A16, 3M Corp.) to modify the composite properties. The A16 GMB has much thinner glass walls than the D32 and iM30k GMB having a particle density of 0.16 g/cc vs. 0.32 and 0.6 of the previous GMB respectively. There is still enough glass to lower the CTE and increase the shear modulus of the composite relative to the unfilled silicone as seen in Figure 2-56 and Figure 2-57.

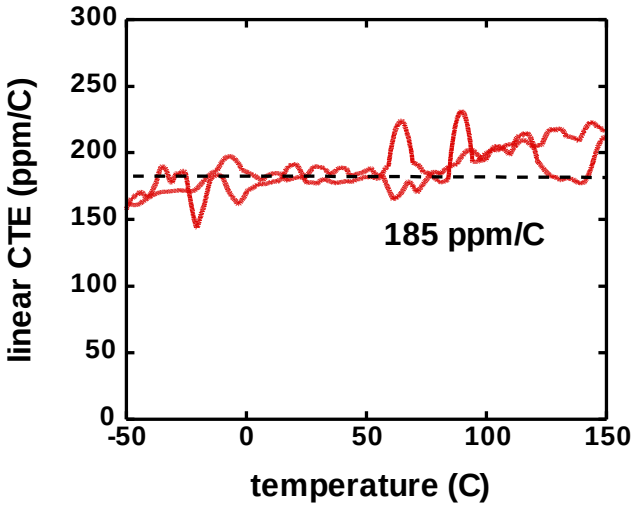

Figure 2-56: Linear CTE of the Sylgard 184/A16 GMB silicone.

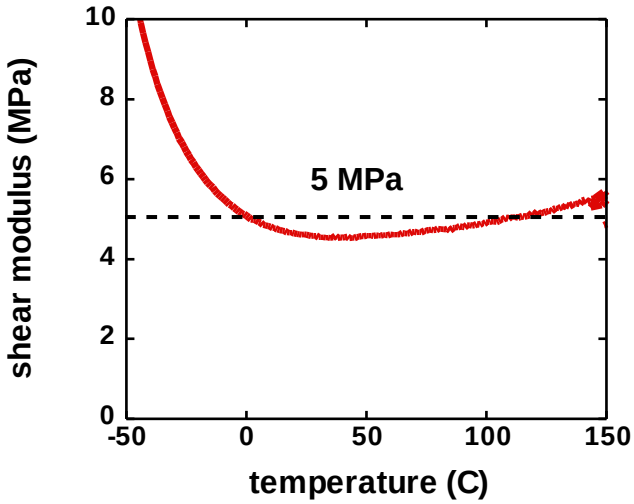

Figure 2-57: Temperature dependent linear shear modulus of the Sylgard 184/A16 GMB silicone.

However, the thin walls break as strain increases as seen in repeat runs of both the room temperature bulk and Young's moduli in Figure 2-58 and Figure 2-59. In Figure 2-58, a cylindrical sample of 184/A16 was compressed with a pressure of 5 MPa in a pressure vessel. The pressure was released and then re-pressurized to 2 MPa, released again and re-pressurized to 7 MPa, released and finally re-pressurized to 1 MPa. The bulk modulus decreased by over an order of magnitude during this sequence from its already low initial value of 71 MPa (compared to 1 GPa for the unfilled silicone).

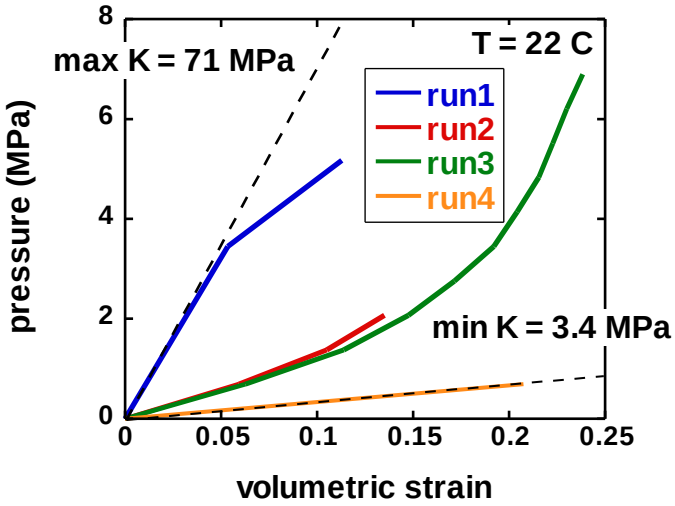

Figure 2-58: Room temperature bulk modulus of the of the Sylgard 184/A16 GMB silicone.

The Young's modulus responded similarly in a ratcheted strain ramp increasing by 20% strain each cycle. The Young's modulus again decreased by over an order of magnitude; however, its initial value was greater than that of the unfilled silicone.

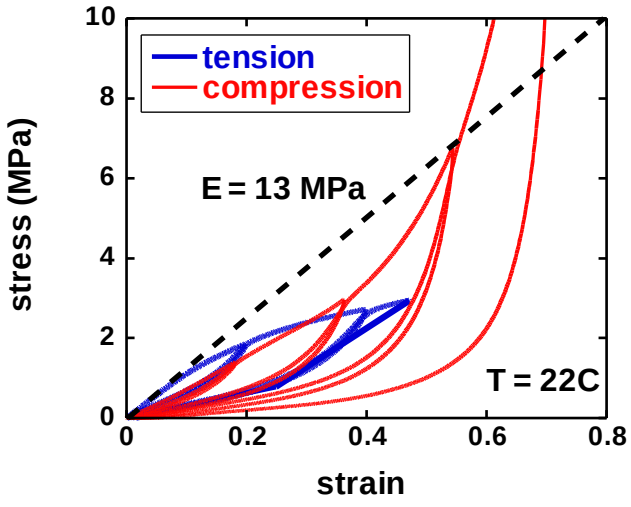

Figure 2-59: Room temperature Young's modulus of the Sylgard 184/A16 GMB silicone from tension and compression tests.

These changes in moduli from balloon breakage could be predicted with a thermoelastic damage model, but it was not attempted in these initial simulations. Instead, elastic properties reflective of some intermediate damage were used as an interesting bound for comparison with the unfilled polymer. All properties used in simulations will be tabulated when discussing the computational results in Section 4. The GMB-filled silicone again de-bonded in room temperature napkin ring tests at a much lower stress (0.21 ± 0.10 MPa) than the maximum tensile stress achieved in the ratcheted tests of Figure 2-59, so it appears the filled silicone will also de-bond prior to failing cohesively.

2.3.4 PMB-Filled Polysulfide

Historically at SNL, polysulfide elastomers are also filled with microballoons but, in this case, with phenolic walls instead of glass (Asia Pacific Microspheres). The phenolic microballoons, PMB, were first pre-baked to thin the walls by oxidizing some pheonolic and were then added to the CS3100 polysulfide at 2.7 wt%. As with the A16 GMB filled Sylgard 184, the CTE decreases (Figure 2-60) and shear modulus increases (Figure 2-61) with the PMB filler, and incremental damage is observed in both the bulk and Young's moduli during ratcheted strain ramp tests (Figure 2-62 and Figure 2-63). This damage was again not modeled in the stress simulations discussed later in Section 4, but elastic properties reflective of some intermediate damage were used instead. As with the unfilled polysulfide, the PMB-filled napkin ring tests failed cohesively rather than adhesively again at a stress of roughly 1 MPa.

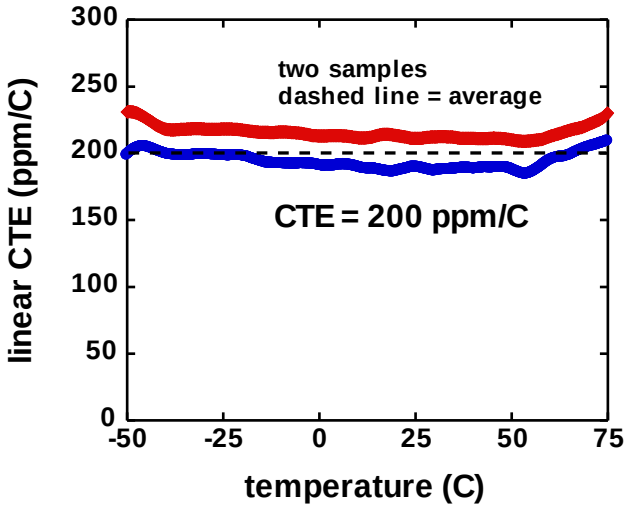

Figure 2-60: Linear CTE of the CS3100/PMB polysulfide.

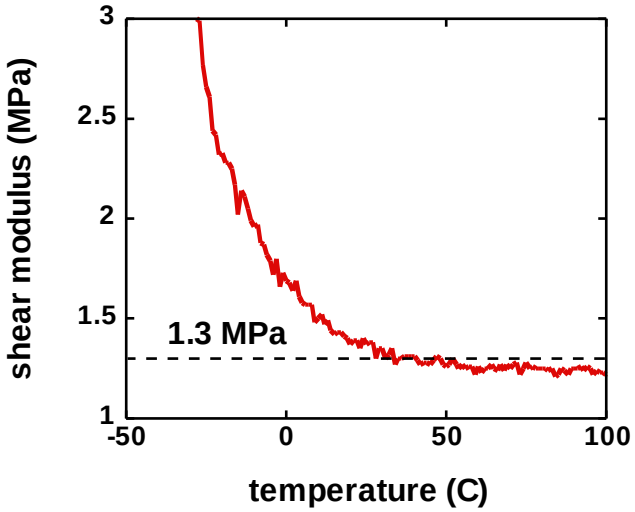

Figure 2-61: Temperature dependent linear shear modulus of the CS3100/PMB polysulfide.

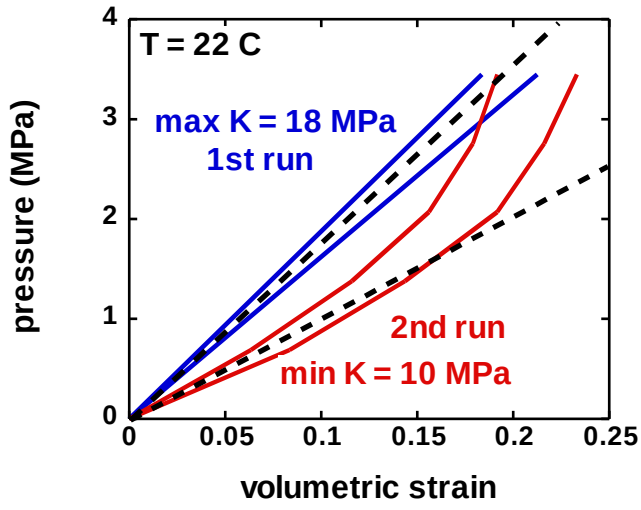

Figure 2-62: Room temperature bulk modulus of the CS3100/PMB polysulfide.

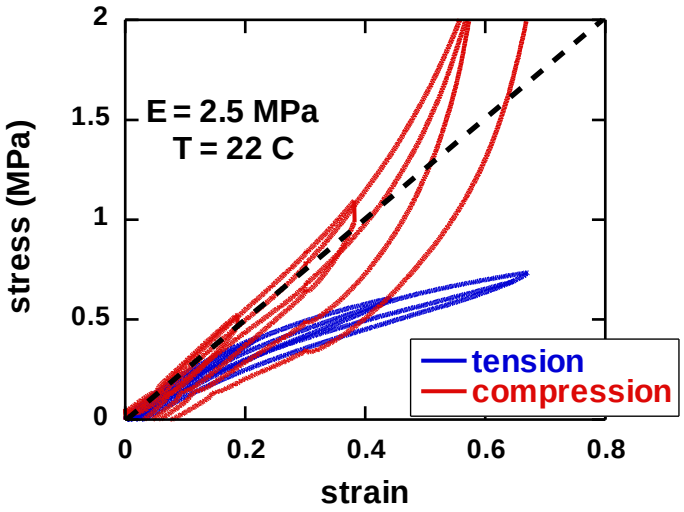

Figure 2-63:. Room temperature Young's modulus of the CS3100/PMB polysulfide from tension and compression tests.

2.4 Printed Circuit Boards

Characterization of the printed circuit boards is inherently more complex since the materials are orthotropic. While PCBs have been characterized extensively for decades, efforts have been almost exclusively limited by plane stress assumptions. That is, the stress in the through-plane direction is assumed constant thereby reducing the number of elastic moduli required from nine (fully three dimensional orthotropic) to six. In particular, the through-plane

moduli (two shear and one longitudinal) are ignored. For our analyses, it is unclear if the plane-stress assumption will be adequate, so a full orthotropic characterization was performed. This atypical experimental procedure is described in Section 2.4.1 and, in Section 2.4.2, is applied to the PCB used in stress simulations (FR04-08, Isola Group). Three-point bend tests in different directions are used to validate the characterization approach. Finally, the properties of this material are compared in Section 2.4.3 to other composites with different reinforcement geometries that were characterized in previous investigations.

2.4.1 Test Procedure for the 3-D Linear Thermoelastic Properties of PCBs

The Tg of FR04-08 stated in the technical data sheet lies between 150 and 200°C. Therefore, the characterization procedure for properties used in stress simulations will be limited to the glassy regime. The linear thermoelastic stress equation is given by Eq. 2.17

$$\underline{\underline{\sigma}} = \underline{\underline{\underline{\underline{C}}}} : \underline{\underline{\varepsilon}} - \underline{\underline{N}}\,\Delta T \qquad (2.17)$$

where $\underline{\underline{\underline{\underline{C}}}}$ is the fourth order stiffness tensor and $\underline{\underline{N}}$ is a second order diagonal tensor incorporating the linear CTEs. The linear CTEs along the three principal axes of the orthotropic composite, α_k, can be measured by the standard thermomechanical analyzer described above (Q400 thermomechanical analyzer, TA Instruments). 1 and 2 are the in-plane axes and 3 is the through-plane axis.

Determination of the glassy elastic moduli is more complicated. Since Eq. 2.17 is quite cumbersome involving fourth order tensors, it is typically simplified by taking advantage of the symmetry of the stress and strain tensors.

$$\underline{\sigma} = \underline{\underline{C}} : \underline{\varepsilon} - \underline{N}\,\Delta T$$

$$\text{where} \quad \underline{\sigma} = \begin{bmatrix} \sigma_{11} \\ \sigma_{22} \\ \sigma_{33} \\ \sigma_{13} \\ \sigma_{23} \\ \sigma_{12} \end{bmatrix}, \quad \underline{\varepsilon} = \begin{bmatrix} \varepsilon_{11} \\ \varepsilon_{22} \\ \varepsilon_{33} \\ \varepsilon_{13} \\ \varepsilon_{23} \\ \varepsilon_{12} \end{bmatrix}, \quad \underline{N} = \begin{bmatrix} N_1 \\ N_2 \\ N_3 \\ 0 \\ 0 \\ 0 \end{bmatrix} \quad \text{with } N_i = \sum_{k=1}^{3} C_{ik}\alpha_k$$

$$\text{and} \quad \underline{\underline{C}} = \begin{bmatrix} C_{11} & C_{12} & C_{13} & 0 & 0 & 0 \\ C_{12} & C_{22} & C_{23} & 0 & 0 & 0 \\ C_{13} & C_{23} & C_{33} & 0 & 0 & 0 \\ 0 & 0 & 0 & G_{13} & 0 & 0 \\ 0 & 0 & 0 & 0 & G_{23} & 0 \\ 0 & 0 & 0 & 0 & 0 & G_{12} \end{bmatrix} \qquad (2.18)$$

where all tensors have been reduced in order.

The three entries of the stiffness matrix ignored by the standard plane-stress assumption are C_{33} and the two through-plane shear moduli, G_{13} and G_{23}. Interestingly, these three quantities are very easily and directly measured by ultrasonic techniques,[14] C_{33} requiring a longitudinal transducer and G_{13} and G_{23} requiring a shear transducer. The moduli, C_{ij}, are related to the wavespeeds, V_{ij}, and sample density by Eq. 2.19.

$$C_{33} = \rho V_{33}^2 \,,\;\; G_{13} = \rho V_{13}^2 \,,\;\; G_{23} = \rho V_{23}^2 \qquad (2.19)$$

The remaining moduli can be evaluated by the standard techniques used with the plane-stress assumption.[15] Rectangular samples of an individual ply (6" x 0.5" x 0.052") were pulled in tension at a constant rate of 0.2"/min at room temperature. Strains in all three dimensions were measured using an extensional extensometer and two transverse extensometers giving the Poisson's ratios, ν_{ij}. In this fashion, all stresses and strains in that test are known so the only unknowns are the applicable moduli. This test was performed along the 1 and 2 principal in-plane axes and at a 45° angle, which produces enough information to populate the remaining entries of the stiffness matrix.

Interestingly, the uniaxial stresses and strains directly populate the inverse stiffness matrix or compliance tensor $\underline{\underline{S}}$ as shown in Eq. 2.20.

$$\underline{\varepsilon} = \underline{\underline{S}} : \underline{\sigma}$$

$$\text{and } \underline{\underline{S}} = \begin{bmatrix} 1/E_1 & -\nu_{12}/E_1 & -\nu_{13}/E_1 & 0 & 0 & 0 \\ -\nu_{21}/E_2 & 1/E_2 & -\nu_{23}/E_2 & 0 & 0 & 0 \\ -\nu_{31}/E_3 & -\nu_{32}/E_3 & 1/E_3 & 0 & 0 & 0 \\ 0 & 0 & 0 & 1/G_{23} & 0 & 0 \\ 0 & 0 & 0 & 0 & 1/G_{13} & 0 \\ 0 & 0 & 0 & 0 & 0 & 1/G_{12} \end{bmatrix} \qquad (2.20)$$

where the thermal terms have been ignored. The E_i are the uniaxial moduli along the i-th principal axis, and $\nu_{ij} = -\,\varepsilon_j/\varepsilon_i$. Note that by symmetry, $E_i\,\nu_{ji} = E_j\,\nu_{ij}$. G_{12} can be determined from the 45° pull data as

$$G_{12} = \frac{E_{45}}{2(1+\nu_{45})} \qquad (2.21)$$

where E_{45} is the uniaxial modulus from that test and $\nu_{45} = -\,\varepsilon_{in}/\varepsilon_{pull}$ with ε_{in} being the transverse strain in the 1-2 plane and ε_{pull} being the uniaxial strain in the 45° test.

Since the through-plane modulus and Poisson's ratios are not measured in this standard plane-stress testing procedure, there is not enough information to invert the upper 3x3 sub-matrix

of the compliance tensor to obtain the required stiffness tensor. However, the ultrasonic measurements provide that information directly. Hence, an iterative convergence strategy can be employed whereby a uniaxial tensile modulus, E_3, is assumed, the compliance matrix is inverted, the resulting stiffness modulus, C_{33}, is compared to the experimental value from ultrasonic measurements, and a new guess for E_3 is made. Note that thermodynamic stability requires the stiffness matrix to be positive definite, so a quick check that all eigenvalues are positive is both easy and wise.

2.4.2 Characterization of a Single Ply of FR04-08

The CTEs of FR04-08 are shown in Figure 2-64 and are intuitively consistent. The magnitude of the through-plane CTE is close to a value expected for a particulate filled composite of the same volume fraction, while the in-plane CTEs are dominated by the woven glass mat. The measured values are also in good agreement with the values tabulated in the material data sheets of 13 and 65 ppm for the in- and out-of-plane CTEs.

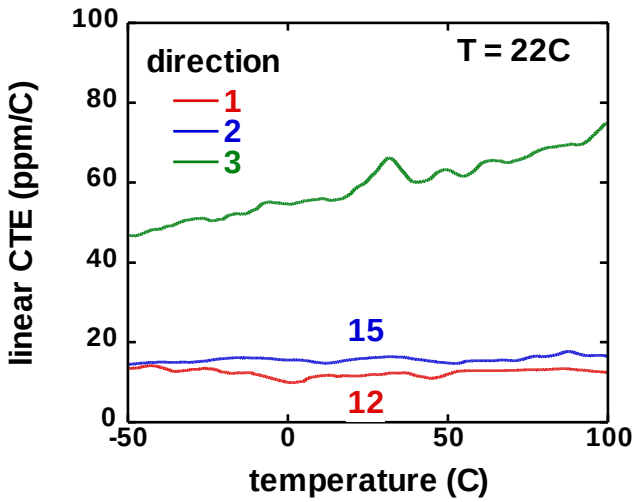

Figure 2-64: Temperature dependent glassy CTEs of FR04-08. Directions 1, 2, and 3 are along the grain, fill, and through axes respectively.

The response in a uniaxial tensile ramp test at room temperature is more interesting. While linear elastic behavior is seen for tests along the two principal in-plane axes, the response for testing at a 45 degree angle is very nonlinear (Figure 2-65 and Figure 2-66). An Instron 8865 load frame was used for these tests using a constant displacement rate of 0.2”/min on a single 0.5” x 6” composite ply (52 mils thick), and strains were measured with an extensometer. The curvature could arise from progressive damage, but tests on previous composites have demonstrated that the nonlinearity arises from yield of the polymer matrix. More detail will be provided in the following section.

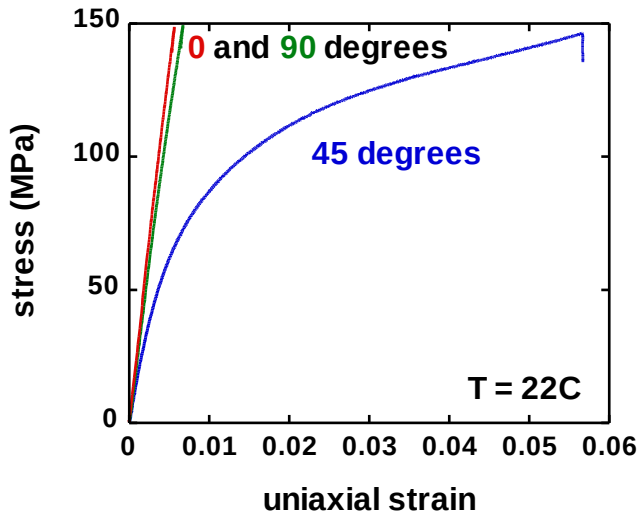

Figure 2-65: Responses to uniaxial tensile tests performed at room temperature at various orientations.

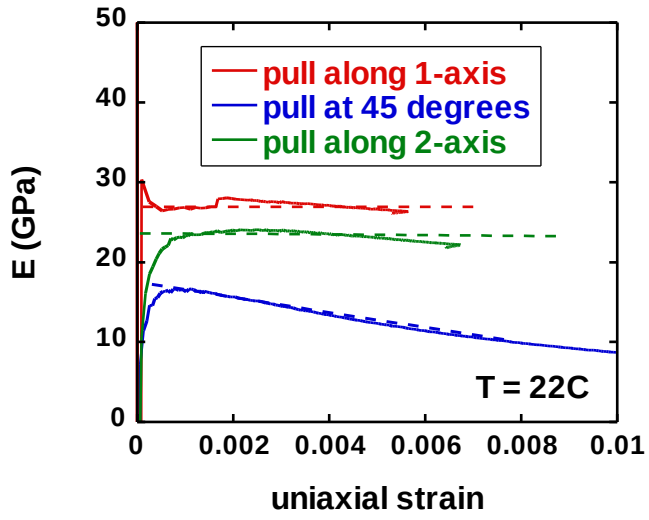

Figure 2-66: Tensile moduli extracted from Figure 2-65.

The Poisson's ratios obtained in these tensile tests from two transverse extensometers are shown in Figure 2-67 and Figure 2-68. Both the measured moduli and Poisson's ratios are in good agreement with the vendor supplied values of 24 / 21 GPa and 0.16 / 0.13 along the 1 and 2 axes respectively. While the vendor data seem accurate, insufficient characterization is supplied to allow for full three-dimensional modeling.

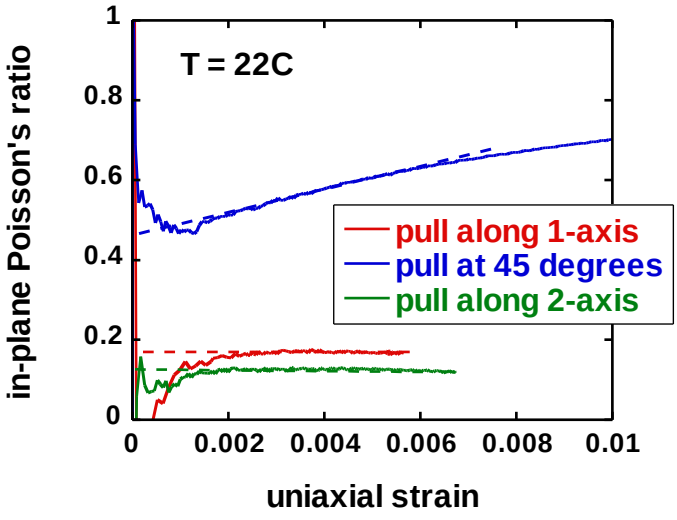

Figure 2-67: In-plane Poisson's ratios for a FR04-08 ply at room temperature.

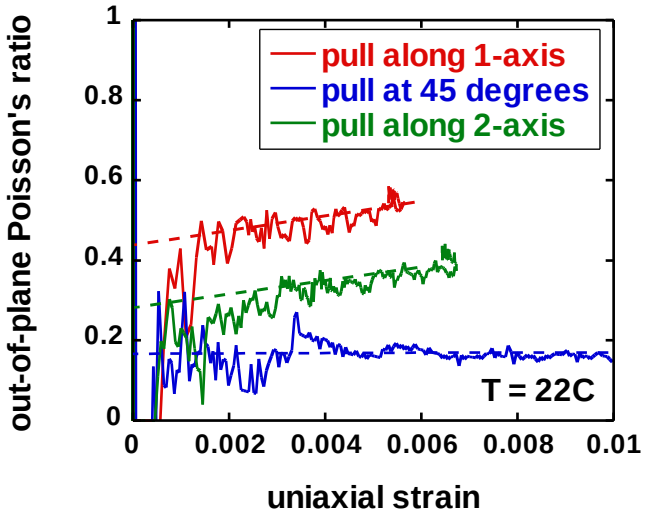

Figure 2-68: Out-of-plane Poisson's ratios for a FR04-08 ply at room temperature.

The stiffness matrix for FR04-08 is given in Eq. 2.22

$$\underline{\underline{C}} = \begin{bmatrix} 31 & 5.8 & 4.9 & 0 & 0 & 0 \\ 5.8 & 27 & 3.6 & 0 & 0 & 0 \\ 4.9 & 3.6 & 10 & 0 & 0 & 0 \\ 0 & 0 & 0 & 6.4 & 0 & 0 \\ 0 & 0 & 0 & 0 & 6.4 & 0 \\ 0 & 0 & 0 & 0 & 0 & 7.7 \end{bmatrix} \text{GPa} \tag{2.22}$$

which is positive definite with eigenvalues of 37, 9, and 23.

2.4.3 Predicting Multi-Ply Response

The characterization data presented above describes the response of a single composite ply. However, actual circuit boards can contain multiple plies with etched copper separating them. To assess the ability to use the single ply data for prediction of multi-ply response, a series of simple three-point bend tests were performed on the Instron 8865 at room temperature. In the first tests, a single ply (1 inch wide) was deformed at a rate of 0.1 inch/min on knife edge supports separated by either 1.75 or 3.75 inches. The deforming anvil had a radius of 0.05 inches. The experimental data (symbols) are shown in Figure 2-69 and Figure 2-70. The tests on the shorter span ended at sample failure, but the samples slipped on the larger span. Also shown in these figures are the predictions of these tests (lines) using an linear elastic orthotropic material model for the composite ply assuming a stress-free condition at the start of the test. The mesh accurately reflected the experimental geometry and was quite refined employing 200 elements along the length of the sample and 12 elements through the thickness. The simulations predicted the linear stiffnesses quite well to displacements of 100 mils. Loads at higher displacement were not computed since they become unreasonable for practical applications, any slippage at the supporting structures is not modeled, and most importantly the inherent viscoelastic nonlinearities of the epoxy seen in Figure 2-65 are not captured by a linear elastic material model.

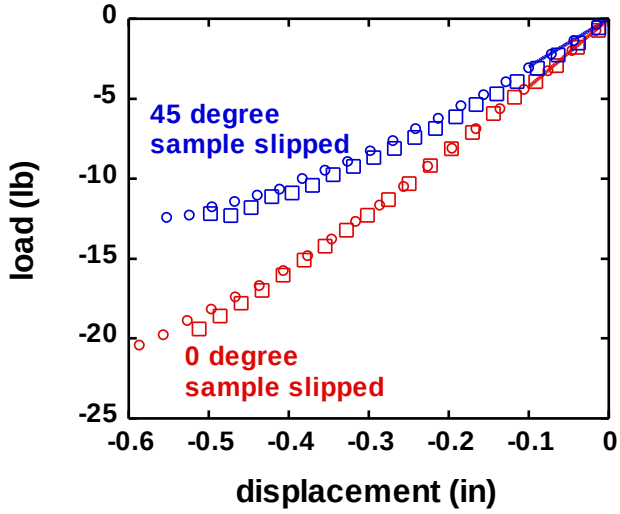

Figure 2-69: Three-point bend test with a span of 3.75 inches at room temperature for a single ply (52 mils) of FR04-08. Symbols are data, and lines are predictions.

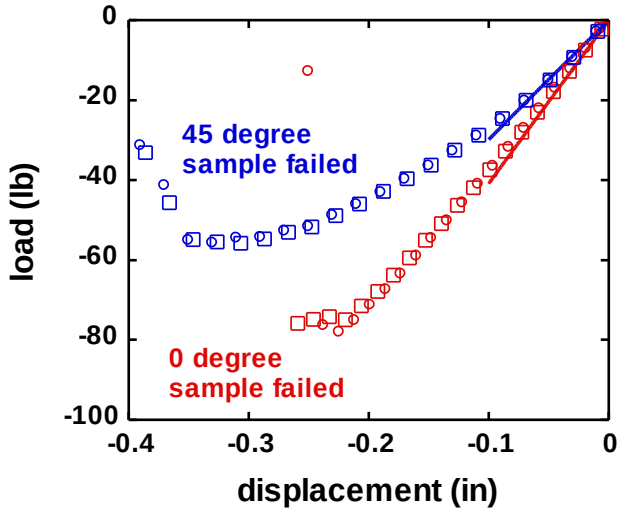

Figure 2-70: Three-point bend test with a span of 1.75 inches at room temperature for a single ply (52 mils) of FR04-08. Symbols are data, and lines are predictions.

Double ply samples (1 inch wide) were also obtained in which two copper-plated (4 mil thick plating per side), 52 mil thick composite individual plies (principal axes aligned) were laminated together with a 5 mil thick pre-preg of the same FR04-08. The same three-point bend results for the 125 mil thick structure are shown in Figure 2-71 and Figure 2-72, and again the predicted initial stiffnesses are in good agreement with the experimental data. The copper was modeled with the visco-plastic constitutive equation and parameters described in the following section.

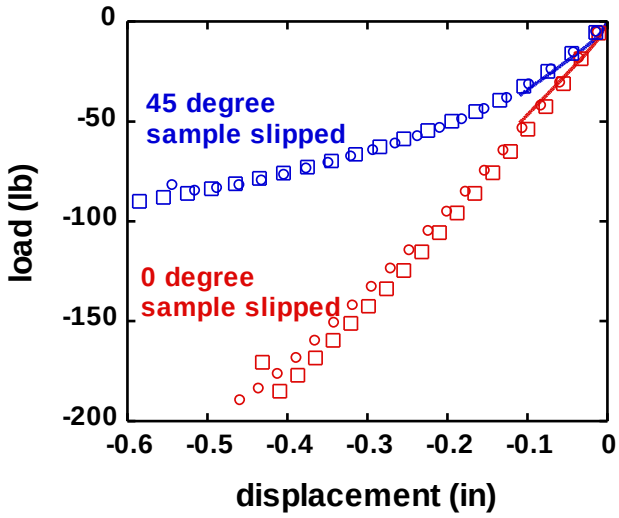

Figure 2-71: Three-point bend test with a span of 3.75 inches at room temperature for the two ply, copper plated FR04-08 lay-up (125 mils total). Symbols are data, and lines are predictions.

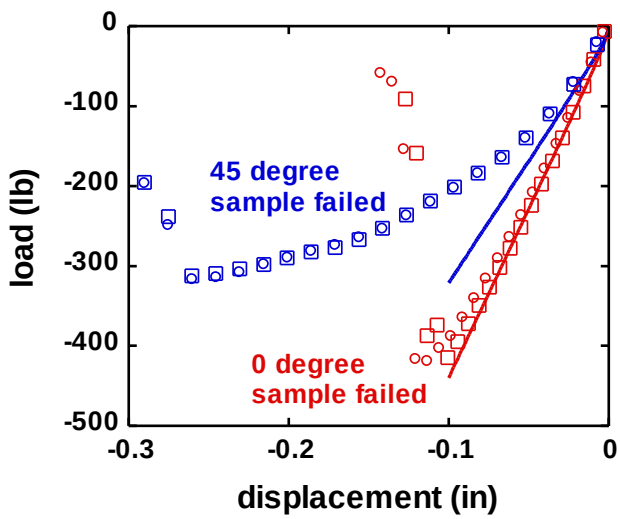

Figure 2-72: Three-point bend test with a span of 1.75 inches at room temperature for the two ply, copper plated FR04-08 lay-up (125 mils total). Symbols are data, and lines are predictions.

The data of Figure 2-72 are re-plotted in Figure 2-73 along with the predicted stress (green line) in the element at the midpoint length and on the bottom of the beam, which is the location of maximum tensile stress. The element response is linear as expected from the material model used. The 45 degree data (blue symbols) begins to depart from linear response at a predicted element stress of roughly 150 MPa, as indicated in Figure 2-73. Comparing this value to the experimental uniaxial response of the single ply in Figure 2-65 indicates that significant nonlinearity occurs near 150 MPa. Therefore, one would expect differences in predictions and

experiments to arise. For possible future predictions, the nonlinear viscoelastic model for isotropic epoxies described previously has been extended to orthotropic systems.

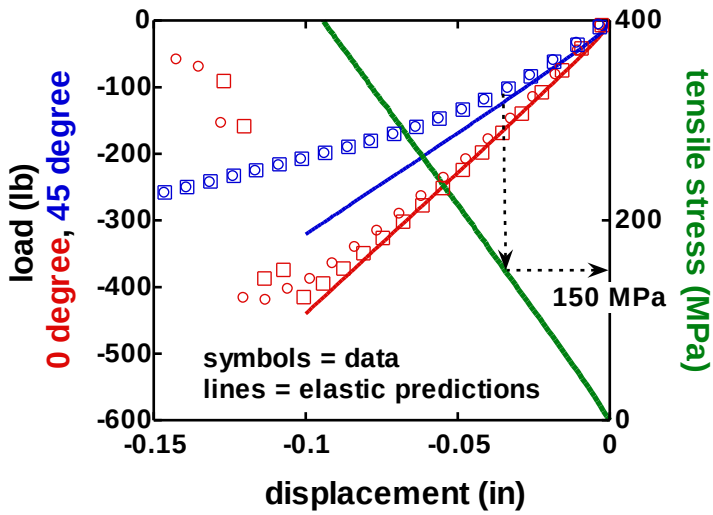

Figure 2-73: Deviations in the predicted and experimental 45 degree responses (blue lines and symbols respectively) arise at a predicted linear elastic stress of 150 MPa in the element experiencing maximum tension. The data in Figure 2-65 shows that significant material nonlinearity occurs near this value explaining the difference.

2.4.4 Comparison to Other PCBs

Previous studies[16] with SNL and New Mexico Tech characterized the full three-dimensional properties of two different composites using the same techniques. Two lay-ups of GF0103 8-harness satin weave E-glass (Hexcel Corp.) vacuum infused with 35wt% VTM 264 epoxy (Advanced Composites Group Inc.) were prepared; the first sample (#1) aligned the 1-axis of twelve mats while the second sample (#2) alternated the 1- and 2-axes. Total thickness of each sample was 90 mils. The stiffness matrices at room temperature are given in

$$\underline{\underline{S}}_{\#1} = \begin{bmatrix} 32 & 6.7 & 5.7 & 0 & 0 & 0 \\ 6.7 & 29 & 5.7 & 0 & 0 & 0 \\ 5.7 & 5.7 & 11 & 0 & 0 & 0 \\ 0 & 0 & 0 & 3.0 & 0 & 0 \\ 0 & 0 & 0 & 0 & 3.0 & 0 \\ 0 & 0 & 0 & 0 & 0 & 5.3 \end{bmatrix} \text{GPa} \qquad (2.23)$$

$$\underline{\underline{S}}_{\#2} = \begin{bmatrix} 31 & 6.1 & 5.9 & 0 & 0 & 0 \\ 6.1 & 28 & 5.7 & 0 & 0 & 0 \\ 5.9 & 5.7 & 11 & 0 & 0 & 0 \\ 0 & 0 & 0 & 4.0 & 0 & 0 \\ 0 & 0 & 0 & 0 & 4.0 & 0 \\ 0 & 0 & 0 & 0 & 0 & 5.4 \end{bmatrix} \text{GPa} \qquad (2.24)$$

The diagonal longitudinal entries (C_{11}, C_{22}, and C_{33}) of both lay-ups are within 10% of the FR04-08 values even though the glass mats are different. The off-diagonal longitudinal entries are within 15% of the FR04-08 values while the shear moduli differ by 50%. One would expect the shear and, to a lesser extent, the off-diagonal longitudinal moduli to be influenced more by the polymer resin, which in this case has a Tg of roughly 120°C vs. 180°C for the FR04. It is possible this Tg difference accounts for the larger variation in shear moduli for the systems.

The temperature dependence of the diagonal longitudinal moduli was measured for sample #2 and is shown in Figure 2-74. Also plotted are the effective moduli of a sample (0.09 x 0.25 x 2 inch) cut at a 45 degree in-plane angle and subjected to a torsional deformation on the ARES rheometer. Multiple elements of the stiffness matrix affect this apparent modulus. Yet all four responses indicate that the glassy stiffnesses are relatively temperature independent, so the room temperature values can be employed across a much wider temperature range.

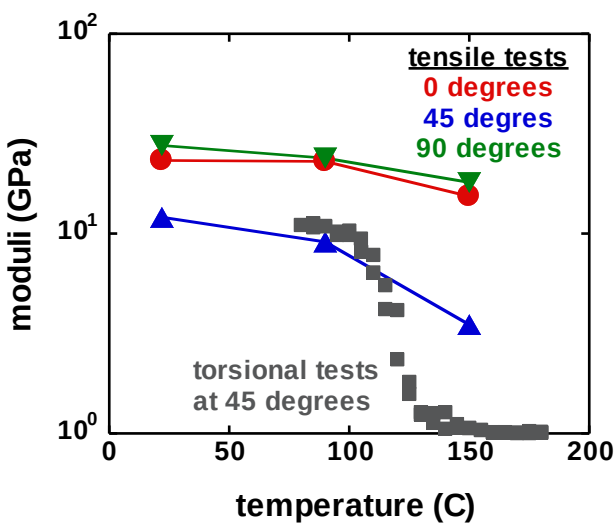

Figure 2-74: Temperature dependent moduli for sample #2.

The temperature dependent CTEs were also measured for sample #2 and are plotted in Figure 2-75. The values again are similar to those measured for FR04-08. Note that the CTE of the pure polymer is also plotted and the rubbery in- and out-of plane CTE's of the composite may appear confusing. The through-plane composite CTE is actually higher than the isotropic rubbery CTE of the pure polymer, and the composite in-plane CTE decreases as temperature is increased through Tg. Such response, while at first surprising, is not uncommon for composites

and can be explained by micromechanics simulations that account for the discrete properties of the constituents.

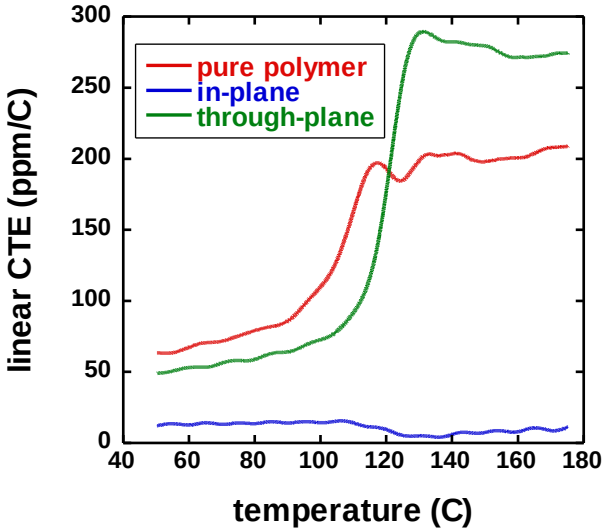

Figure 2-75: Temperature dependent CTEs for sample #2.

The compressive yield stress of sample #2 (alternating 1- and 2-axes) was measured at 22°C on a sample oriented at an in-plane angle of 45 degrees (Figure 2-76). Significant curvature is observed for this sample that is similar to the observations on the FR04-08 tensile tests at 45 degrees in Figure 2-65. To distinguish between epoxy resin yield and composite damage, the sample after initial yield testing (red curve in Figure 2-76) was taken above its Tg to anneal the stress history, cooled back to room temperature, and subjected to the identical yield test. The response (blue curve in Figure 2-76) is identical implying a reversible phenomenon such as resin yield rather than irreversible damage. The sample failed at 9% strain so the downturn at roughly 8% strain does probably indicate the onset of damage.

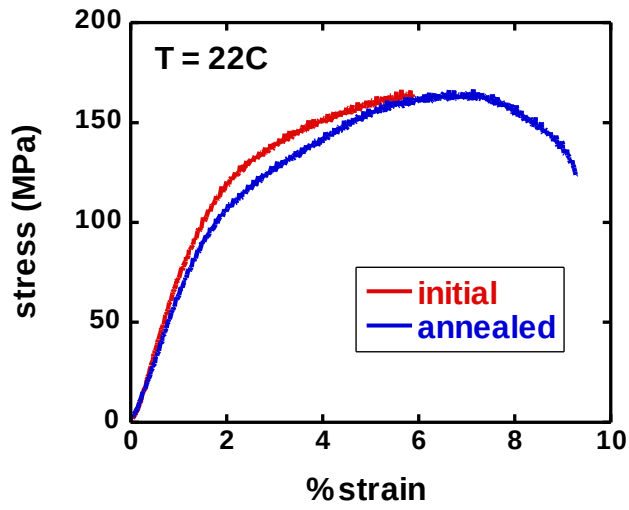

Figure 2-76: Compressive yield for sample #2 at room temperature oriented at an in-plane angle of 45 degrees.

To reinforce the contention that the nonlinear ramp response arises from viscoelasticity rather than damage, compressive creep tests were also performed on sample #2 at room temperature in the 45 degree orientation. Various loads were applied at a rate of 150 MPa/min with the Instron 1125 load frame on samples with dimensions 2.3 x 3.8 x 8.9 mm, and creep was monitored with an extensometer attached to a sub-press. The resulting compliances are shown in Figure 2-77 and are quite nonlinear both in magnitude (larger compliance as the load increases) and shape (note the logarithmic scale). A similar response is typically seen for nonlinear creep of unfilled epoxies.

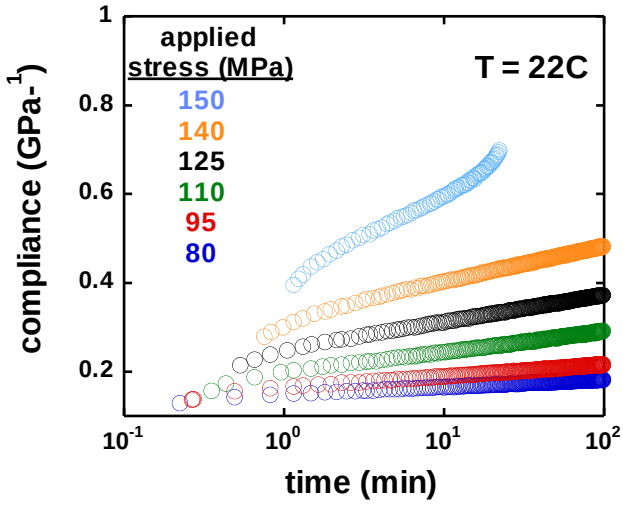

Figure 2-77: Tensile creep for sample #2 at room temperature oriented at an in-plane angle of 45 degrees.

2.5 Solders

Stephens and Frear[17] studied the creep behavior of near-eutectic 60Sn-40Pb solder and found that this solder, as expected, exhibits significant creep at stress levels well below the yield strength for this material. This occurs because even at room temperature the solder is at a high homologous temperature. Stephens and Frear[17] found that the minimum or steady state creep rate, $\dot{\gamma}_{\min}$, could be described using

$$\dot{\gamma}_{\min} = Ae^{\frac{-Q}{RT}}\left[\sinh(\alpha\sigma)\right]^{p} = 2.48x10^{4}e^{\frac{-56,944}{RT}}\left[\sinh(0.0793\sigma)\right]^{3.04} \qquad (2.25)$$

where R is the gas constant, 8.314 J/mole-K, T is absolute temperature, σ is true stress in MPa. Boyce eta al.[18] used a high-rate servo-hydraulic method to characterize the temperature and strain-rate dependent stress-strain behavior of eutectic Sn-Pb solder over a wide range of strain rates (10^{-4} to 10^{2} per second) and temperatures (-60 °C to +100 °C)[18]. By plotting the inelastic strain rate from the Boyce et al.[18] experiments as a function of applied true stress at steady state, it can be seen that the Zener-Holloman plot obtained by Stephens and Frear for 60Sn-40Pb solder also provides a reasonably good fit to Boyce et al.'s steady state data for 63Sn-37Pb solder (Figure 2-78). This suggests that a unified creep plasticity model with a kinetic equation for inelastic rate that uses a hyperbolic sine function of effective stress should be able to describe the behavior of solder over a wide range of temperatures and strain rates.

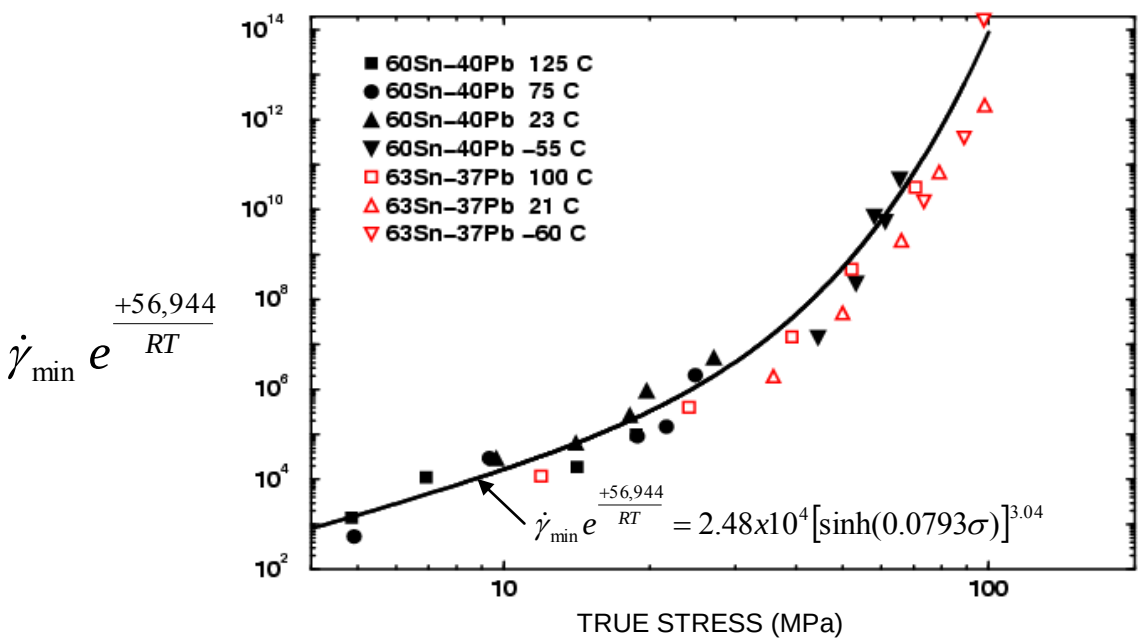

Figure 2-78: Zener-Holloman plot of the temperature compensated minimum or steady state strain rate as a function of stress for Sn-Pb solder. Solid symbols are Stephens and Frear17 data for 60Sn-40Pb and hollow symbols are Boyce et al.18 data for 63Sn-37Pb solder.

The unified creep plasticity model developed here is based on the unified creep plasticity model for braze alloys developed by Neilsen et al.[19]. For small elastic strains, the total strain rate, $\dot{\boldsymbol{\varepsilon}}$, can be additively decomposed into elastic, $\dot{\boldsymbol{\varepsilon}}^{e}$, and inelastic (creep + plastic), $\dot{\boldsymbol{\varepsilon}}^{in}$, parts as follows

$$\dot{\boldsymbol{\varepsilon}} = \dot{\boldsymbol{\varepsilon}}^{e} + \dot{\boldsymbol{\varepsilon}}^{in} \tag{2.26}$$

It is assumed that the elastic response is linear and isotropic such that the stress rate is given by the following equation

$$\dot{\boldsymbol{\sigma}} = \mathbf{E} : \dot{\boldsymbol{\varepsilon}}^{e} = \mathbf{E} : (\dot{\boldsymbol{\varepsilon}} - \dot{\boldsymbol{\varepsilon}}^{in}) \tag{2.27}$$

where **E** is the fourth-order isotropic elasticity tensor. A kinetic equation for the inelastic strain rate, $\dot{\boldsymbol{\varepsilon}}^{in}$, with the following form is used

$$\dot{\boldsymbol{\varepsilon}}^{in} = \frac{3}{2}\dot{\gamma}\,\mathbf{n} = \frac{3}{2} f \,\sinh^{p}\left(\frac{\tau}{D}\right)\mathbf{n} \tag{2.28}$$

where f is a (typically Arrhenius) function of temperature, D is an internal state variable which accounts for isotropic hardening and recovery, **n** is the normalized stress difference tensor which is given by,

$$\mathbf{n} = \frac{\mathbf{s} - \frac{2}{3}\mathbf{B}}{\tau} \tag{2.29}$$

where **s** is the stress deviator, **B** is the second-order state tensor which accounts for kinematic hardening and recovery, and τ is a scalar measure of the stress difference magnitude as follows

$$\tau = \sqrt{\frac{3}{2}\left(\mathbf{s} - \frac{2}{3}\mathbf{B}\right) : \left(\mathbf{s} - \frac{2}{3}\mathbf{B}\right)} \tag{2.30}$$

Competing non-linear hardening and thermal recovery mechanisms are captured by the evolution equations for the internal state variable D and the internal state tensor **B**. Evolution of the internal state variable D is given by

$$\dot{D} = \frac{A_1 \dot{\gamma}}{(D - D_0)^{A_3}} - A_2 (D - D_0)^2 \tag{2.31}$$

where D_0, A_1, A_2, and A_3 are material parameters. Evolution of the second-order state tensor **B** is given by

$$\dot{\mathbf{B}} = \frac{A_4\,\dot{\boldsymbol{\varepsilon}}^{in}}{b^{A_6}} - A_5 b\mathbf{B} \qquad (2.32)$$

where A_4, A_5, and A_6 are material parameters and b is the magnitude of **B** as follows

$$b = \sqrt{\frac{2}{3}\mathbf{B}:\mathbf{B}} \qquad (2.33)$$

Selection of material parameters for a unified creep-plasticity constitutive model can be quite complex[20]. Parameters for eutectic SnPb solder were obtained from a non-linear least squares fit to the uniaxial tension data presented in Figure 2-79. The non-linear least squares fit to this data was performed using the Levenberg and Marquardt Nonlinear Least Squares Algorithm[21] and a driver program for the constitutive model. Initial estimates for the material parameters were based on the steady state creep correlations presented in the previous section. Material parameters obtained from the non-linear least squares fitting process are summarized in Table 2.9. Since, the uniaxial tension data was monotonic, separation of kinematic hardening and recovery from isotropic hardening and recovery was not possible. For the fits tabulated here, purely isotropic hardening and recovery was assumed.

Finally, Boyce et al.'s uniaxial tension experiments were simulated using a finite element code with this unified creep plasticity model and the material parameters given in Table 2-9. As expected, the model predictions match the experimental results for a wide range of test temperatures and strain rates (Figure 2-79). The model predictions are represented by solid lines in Figure 2-79.

Table 2-9: Eutectic Sn-Pb Solder – Unified Creep Plasticity Model Parameters.

Temperature (^oC)	-60	21	100
Young's Modulus (MPa)	48,276	43,255	36,860
Poisson's Ratio	0.380	0.400	0.430
Flow Rate ln(f)	-44.63	-20.09	-10.72
Sinh Exponent, p	7.1778	4.2074	3.7151
Isotropic Hardening, A_1 (MPa^{A3+1})	270.67	193.44	167.76
Isotropic Recovery, A_2 (1/MPa-sec)	0.37891×10^{-3}	1.8074×10^{-3}	8.3128×10^{-3}
Isotropic Exponent, A_3	0.970		
Kinematic Hardening, A_4 (MPa^{A6+1})	0.0		
Kinematic Recovery, A_5 1/(MPa-sec)	0.0		
Kinematic Exponent, A_6	1.0		
Flow Stress, D_0 (MPa)	8.2759		
Thermal Expansion Coefficient (1/C)	25.0×10^{-6}		

Solomon[22] studied low cycle fatigue of Sn-Pb solder and developed a Coffin Manson failure criterion in which cycles to failure, N_f, is based on the plastic shear strain range, $\Delta\gamma_p$, which can

be estimated from the increment in equivalent plastic strain from one complete thermal cycle, $\Delta EQPS$, as follows

$$N_f = \left(\frac{1.14}{\Delta\gamma_p}\right)^{\frac{1}{0.51}} \approx \left(\frac{1.31636}{\Delta EQPS}\right)^{1.96078} \qquad (2.34)$$

This criterion was used to generate lifetime predictions from the finite element analyses in the next section.

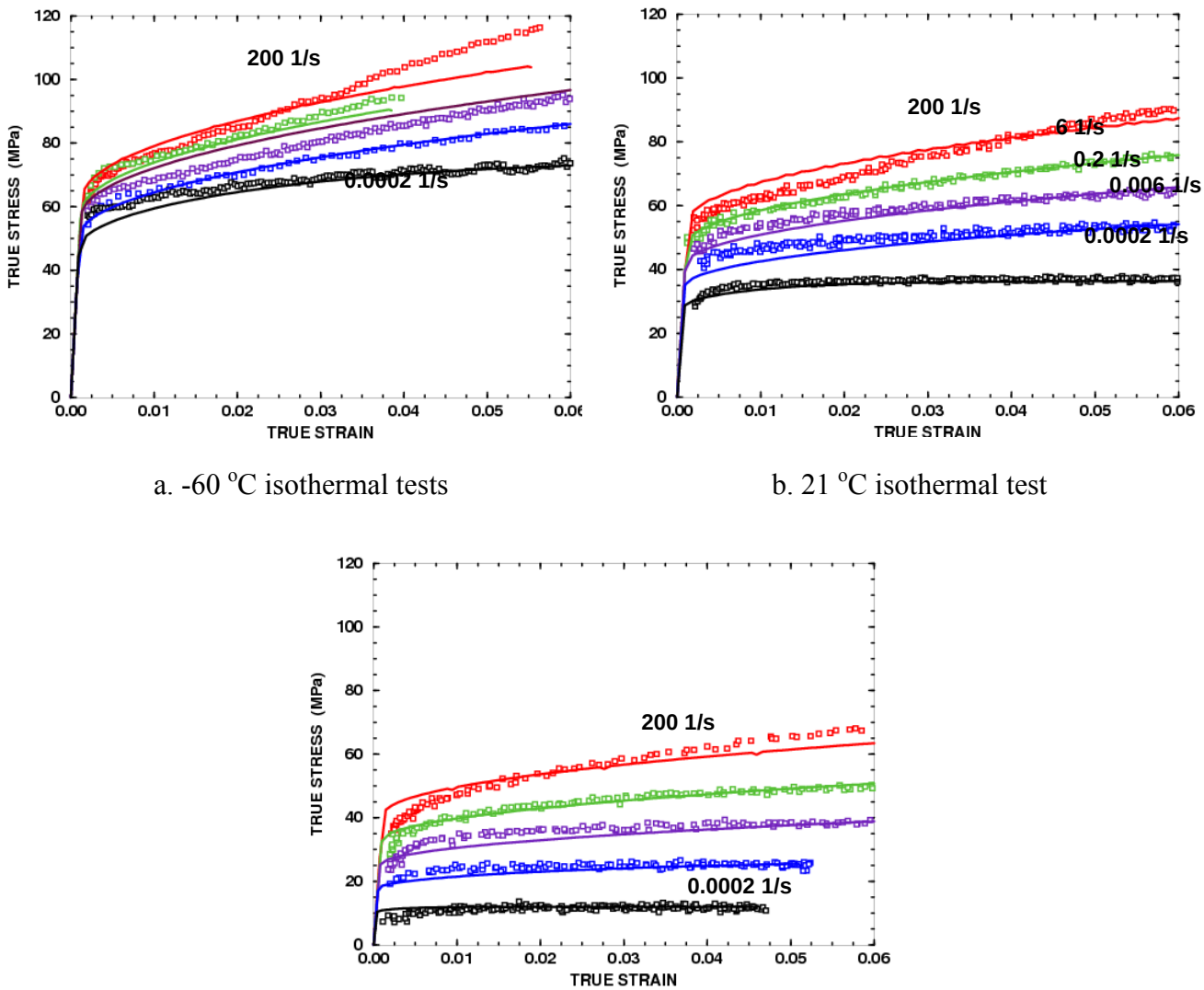

a. -60 °C isothermal tests

b. 21 °C isothermal test

c. 100 °C isothermal tests

Figure 2-79: Comparison of unified creep plasticity model predictions (solid lines) with experimental data (symbols) from Boyce et al.[18] for strain rates from 0.0002 per second to 200.0 per second.

3 FINITE ELEMENT ANALYSES

When designing printed circuit boards (PCBs) to survive operational environments, it is important to understand the stresses and strains generated during manufacturing, thermal cycling and dynamic loading. Cracking of encapsulants or ceramic components, underfill debonding, and solder fatigue are just a few of the potential failure mechanisms that must be avoided. The previous sections described work done to characterize and model the polymers and solders used to package electronic components. In this section, finite element analyses are applied to evaluate design options for generic surface mounted components subjected to thermal cycling only.

Surface mount technology is quite common in modern electronics industry. To increase the reliability of these electronics, glassy thermosets are sometimes used as underfills. By adding filler to the polymer, underfill mechanical properties such as the bulk and shear moduli and the coefficient of thermal expansion (CTE) can be tailored. Filler options include glass micro-balloons (GMB) or hard fillers such as silica or alumina. The presence of underfills can affect the solder reliability and component failure during dynamic environments as well. Solder fatigue is an issue due to strains generated by the mismatch in coefficients of thermal expansion between dissimilar materials in the assembly. Deformation and cracking of solder have been an important subject for many numerical investigations. If a low CTE ceramic component is soldered to a higher CTE epoxy glass circuit board, thermal cycling may result in plastic solder deformation. With subsequent thermal cycling, solder fatigue can initiate cracks that ultimately produce an open circuit. Addition of an underfill increases the complexity of the stress state in the assembly, sometimes in a non-intuitive way. However, the generic filled Simplified Potential Energy Clock (SPEC) model of the underfill when combined with a unified creep plasticity model for the solder and the Coffin-Manson solder fatigue criterion, provides an excellent tool for investigating the sensitivity of solder fatigue life in surface mounted components attached by various underfill filler materials and filler volume fractions (FVF). Given that the SPEC model, the unified creep plasticity model, and the Coffin-Manson criterion have been extensively validated and documented, the numerical approach adopted in this study is believed to be useful for providing trends in stress evolution and fatigue resistance. This is valuable information that can build simulation-based intuition and provide guidelines for design practices.

Two components with significantly different geometries were chosen for the study. First, a “large” capacitor, seen in Figure 3-1, was selected because of its stiff block-like geometry. The second was a small resistor shown in Figure 3-2. Not only is the resistor significantly smaller than the capacitor (0.365”×0.02”×0.125” vs. 0.55”×0.265”×0.5”), the length to thickness ratio also is quite different resulting in more flexible “diving-board” like geometry. The underfill gaps of these components were chosen to represent workable geometries that may be underfilled without screening out the filler because the gap is too small and without requiring damming around the component because the gap is too large. The gaps assumed in the analyses were 0.381 mm for the capacitor and 0.127 mm for the resistor, where the gap is height that the component sits off the board. The various encapsulation coating configurations investigated are summarized in **Error! Reference source not found.** thru **Error! Reference source not found.**.

Implicit, quasi-static, 3D finite element models of the two representative surface mount components were utilized to model the residual stress and strain due to underfilling and thermal cycling. The assemblies were assumed to be stress free at the underfill cure temperature, and the response of the components as a function of temperature was computed using Sandia National Laboratories’ finite element code ADAGIO.

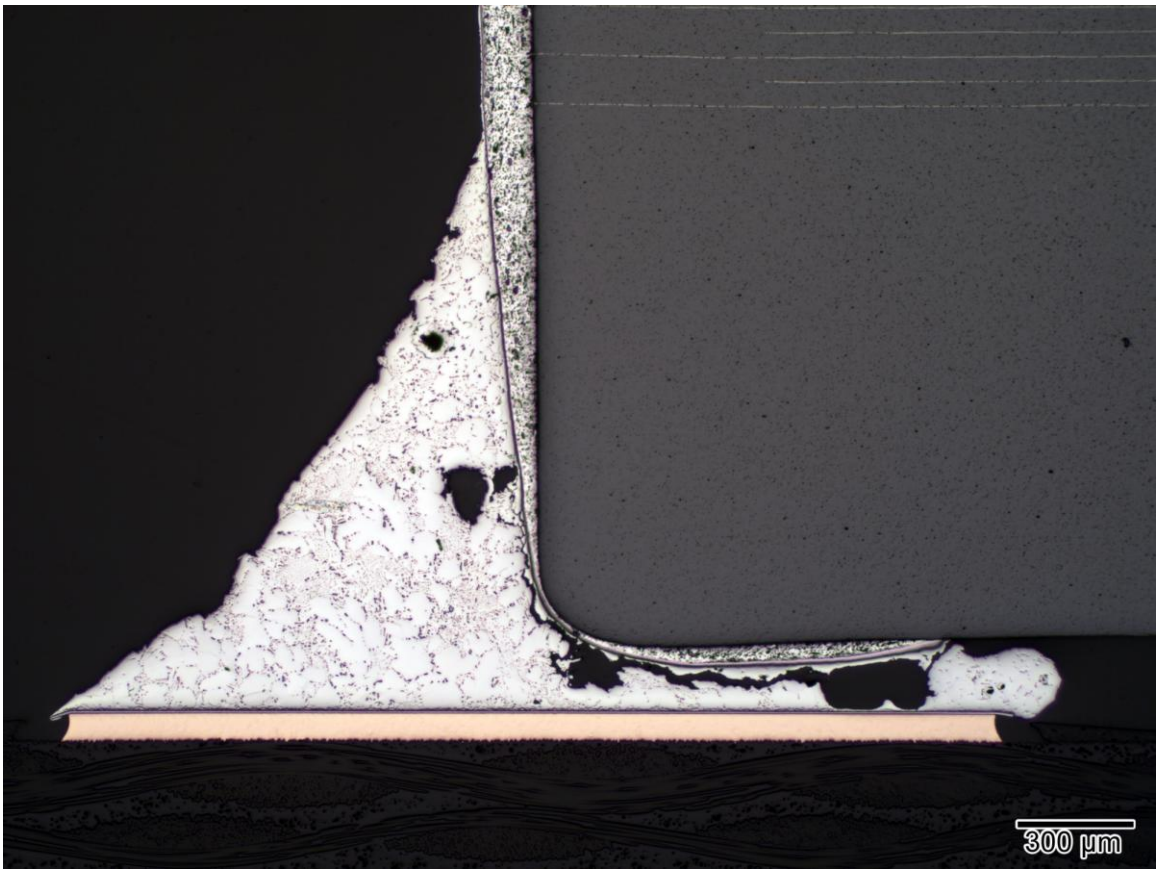

Figure 3-1: Cross-sectioned “large” capacitor with cracked solder joint

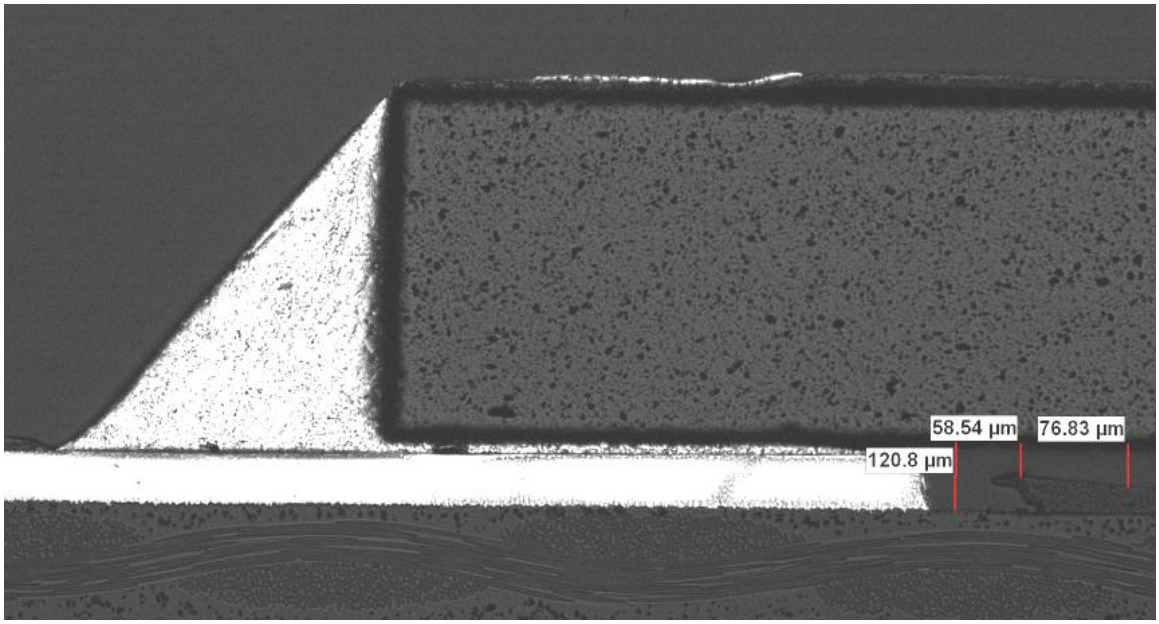

Figure 3-2: Cross-sectioned “small” resistor with intact solder joint

Table 3-1: Packaging variations examined for a GMB-filled epoxy encapsulant.

underfills → coatings ↓	no underfill	unfilled epoxy underfill	filled with 10-40vol% alumina	filled with 10-40vol% GMB
no coating	X	X	X	X
unfilled silicone	X	X	X	X
silicone filled with GMB	X	X	X	X
unfilled polysulfide	X	X	X	X
polysulfide filled with PMB	X	X	X	X

Table 3-2: Packaging variations examined for a foam encapsulant.

underfills → coatings ↓	no underfill	unfilled epoxy underfill	filled with 10-40vol% alumina	filled with 10-40vol% GMB
no coating	X	X	X	X
unfilled silicone	X	X	X	X
unfilled epoxy	X	X	X	X

Table 3-3: Packaging variations examined for no encapsulant.

underfills → coatings ↓	no underfill	unfilled epoxy underfill	filled with 10-40vol% alumina	filled with 10-40vol% GMB
no coating	X	X	X	X
unfilled silicone	X	X	X	X
unfilled epoxy	X	X	X	X

The finite element models of a "large" capacitor and "small" resistor are shown in Figure 3-3 and Figure 3-4 respectively. The models were restrained normal to vertical sectioning planes to approximate a 1/4 symmetry boundary condition (i.e., the xy and yz planes are symmetry planes). To reduce the number of required elements, a fine mesh of each component was inserted into a coarse mesh of the encapsulated printed circuit board using tied contact boundary conditions at the adjacent interfaces. Thermal stresses were generated in each model by cooling the assembly from the underfill cure temperature of 80°C to -55°C, where -55°C is approximately the minimum temperature environment that this component might be expected to experience during its service duration. The assembly was then reheated to 70°C and cooled to -55°C to complete the thermal cycle.

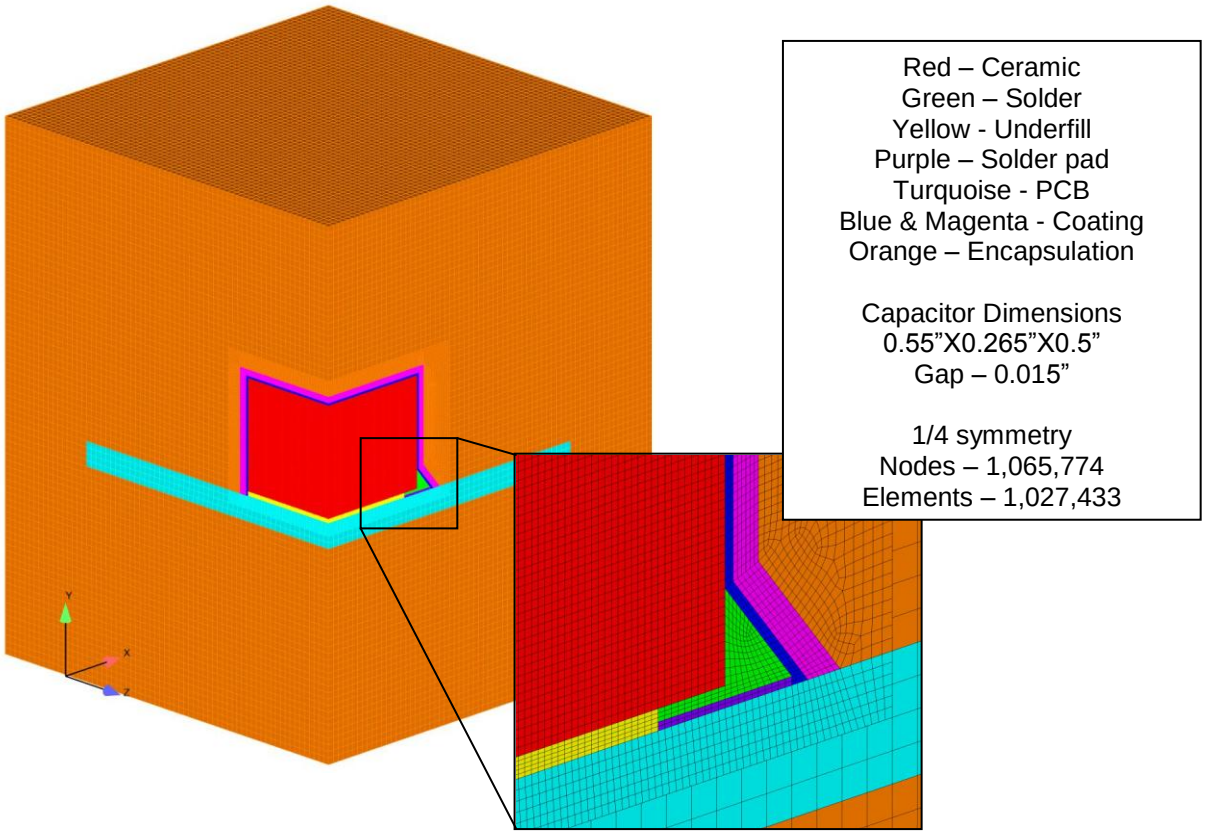

Figure 3-3: Capacitor quarter symmetry finite element mesh used in the finite element analysis

The capacitor and resistor were modeled as an elastic ferrite ceramic. A power law hardening plasticity model was used for the copper solder pads, and an isotropic elastic model was used to simulate the FR4 printed circuit board. The Pb-Sn solder was modeled using unified creep plasticity model described in Section 2.5. Elastomer coating materials were modeled using Mooney-Rivlin fits of the properties described in Section 2.3. The epoxy over-encapsulation was modeled using the Simplified Potential Energy Clock Model described in Section 2.1.1, and the actual inputs used for the 828/DEA/GMB epoxy in the model are given in Table 2-2. An elastic model was assumed when foam was modeled for the encapsulation. Many constants and

CTE's used for various materials in the simulations are listed in Table 3-4. The underfill properties are based on those of iM30k glass micro balloons or alumina filled 828/D230 epoxy, with the FVF varied from 0 to 40%. The generic nonlinear viscoelastic model was used to represent the filler variations in the underfill. This is described in Section 2.2.3 and Section 2.2.4. The model inputs are listed in Table 2-7and Table 2-8.

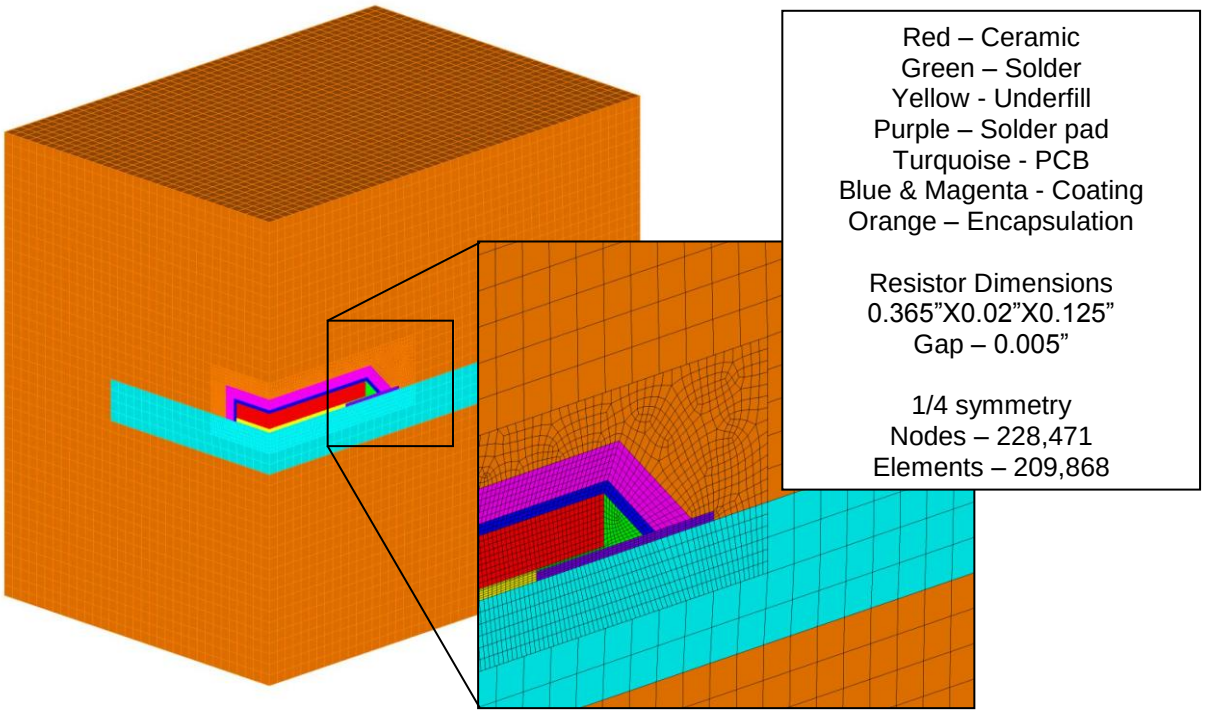

Figure 3-4: Resistor quarter symmetry finite element mesh used in the finite element analysis

Table 3-4: Constants and CTE's for various analysis materials.

Material	Young's Modulus (GPa)	Poisson's Ratio	CTE (/°C)	Yield Stress (MPa)	Hardening Constant (MPa)	Hardening Exponent
Ferrite	161.0	0.25	10.4E-6	NA	NA	NA
Copper	117.0	0.34	16.9E-6	0.689	458.7	0.364
FR4	17.2	0.3	16.0E-6	NA	NA	NA
20# Foam	0.11	0.297	45.0E-6	NA	NA	NA

3.1 Coating Stresses

3.1.1 Epoxy Encapsulant

For contiguously meshed geometry with 828/DEA/GMB epoxy over-encapsulation, the unfilled elastomeric coatings result in high calculated tensile stresses during the cool-down of the thermal cycle at the low temperature of -55°C. This was found to be true for both the thick and thin coatings, and for both the capacitor and resistor. The peak values of the calculated maximum principal tensile stresses can be seen in Figure 3-5.

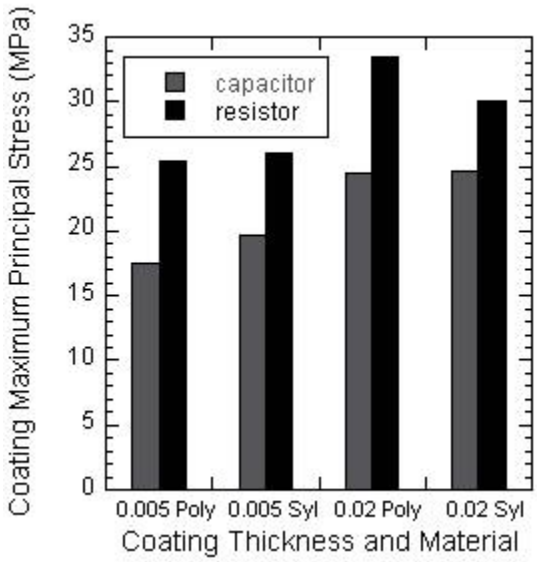

Figure 3-5: Plot of max principal stress in unfilled elastomer coatings for contiguously meshed resistor and capacitor models

The calculated maximum principal tensile stresses in the polysulfide ranged from 15 MPa in the 0.005" thick coated capacitor to 34 MPa in the 0.02" thick coated resistor. The calculated maximum principal tensile stresses in the Sylgard ranged from 20 MPa in the 0.005" thick coated capacitor to 30 MPa in the 0.02" thick coated resistor. The experimentally determined failure tensile strengths for the unfilled elastomeric coatings in Section 2.3 were found to be on the order of 1 MPa. Because these calculated stresses exceed the failure tensile strengths of the materials by an order of magnitude one could expect that the elastomeric coatings will fail cohesively (polysulfide) or adhesively (Sylgard). This result is consistent with sectioned electronic devices as seen in Figure 3-6, where the unfilled polysulfide in a penetrator fuze has failed cohesively.

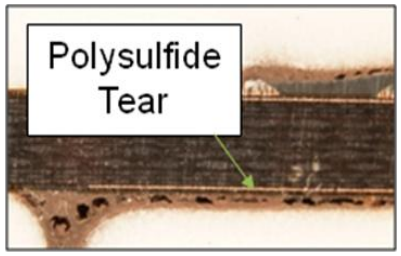

Figure 3-6: Sectioned Penetrator Fuze with cohesively failed, unfilled polysulfide, elastomer coating.

As a result, to avoid modeling failure and failure propagation, the elastomer elements in the models were detached from the surrounding epoxy elements creating a debonded interface. The models were then rerun using this new geometry, and further analysis with unfilled elastomer coatings assume a debonded interface. An image at -55°C depicting the predicted deformed mesh of the debonded elastomer in the resistor model can be seen in Figure 3-7. The model assumes a 0.02" thick elastomer coating.

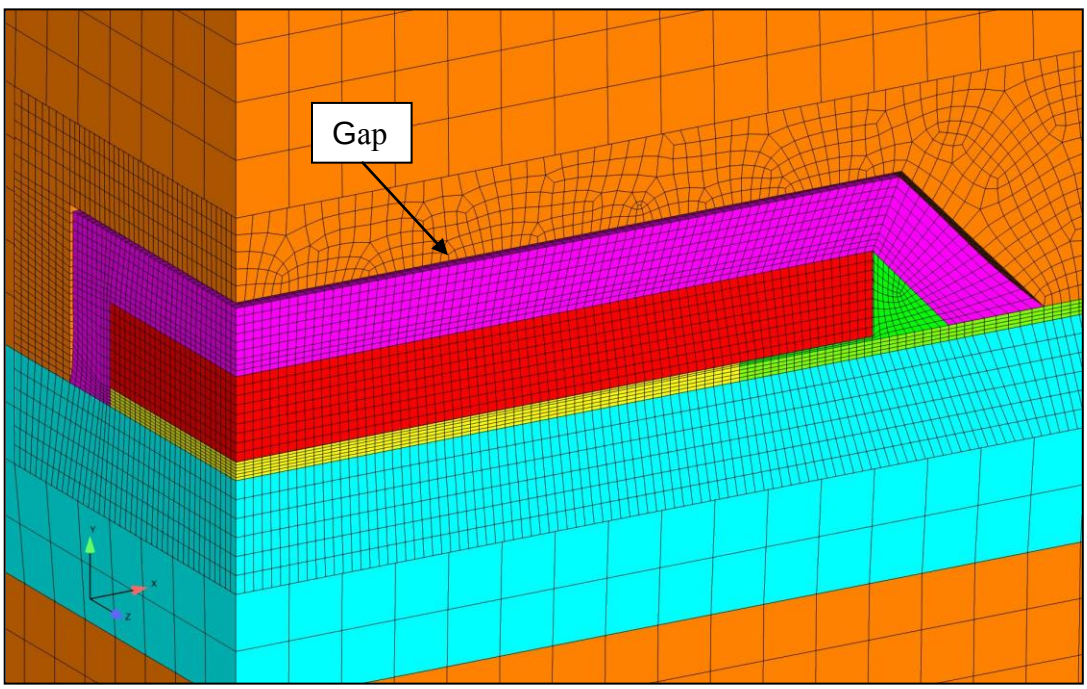

Figure 3-7: Resistor model (1/4 symmetry) with debonded elastomer coating at -55°C.

The filled elastomeric coatings resulted in significantly lower calculated tensile stresses during the cool-down of the thermal cycle. The peak values of the calculated maximum principal tensile stresses for the contiguously meshed geometries can be seen in Figure 3-8. As seen in the figure, the calculated maximum principal tensile stresses in the phenolic micro balloon (PMB) filled polysulfide ranged from 0.6 MPa in the 0.005" thick coated capacitor to 0.7 MPa in the 0.005" thick coated resistor. The calculated maximum principal tensile stresses

in the glass micro balloon (GMB) filled Sylgard ranged from 0.3 MPa in the 0.02" thick coated resistor to 0.8 MPa in the 0.005" thick coated capacitor. As with the unfilled elastomers, the experimentally determined failure tensile strengths for the filled elastomeric coatings in Section 2.3 were found to be on the order of 1 MPa, thus failure of the filled elastomeric coatings was not considered likely, and a contiguous mesh was a reasonable assumption.

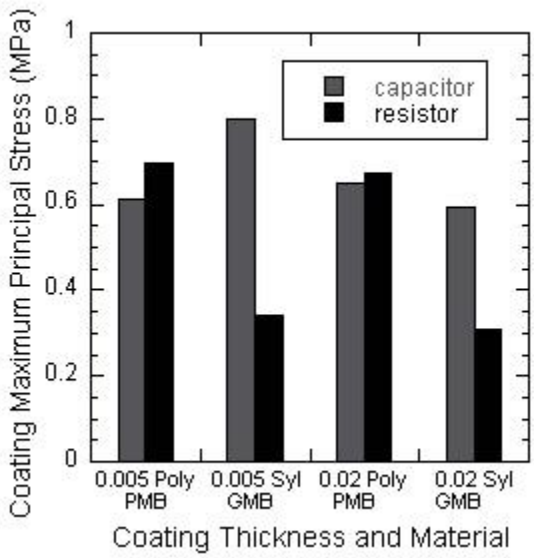

Figure 3-8: Plot of max principal stress in filled elastomer coatings for contiguously meshed resistor and capacitor models

3.1.2 Foam Encapsulant / No Encapsulant

Only two conformal coating cases were investigated for foam encapsulation. The first, assumed a 0.005" thick unfilled Sylgard. The maximum principal tensile stress in the Sylgard was calculated to be 5.0 MPa. As with the other unfilled elastomer coatings, this stress may result in debonding of the coating, however, additional calculations assuming debonded coatings were not performed for foam encapsulation. The second coating case involving foam encapsulation assumed unfilled 0.005" thick 828/D230 epoxy coating. The maximum principal tensile stress in this glassy coating was calculated to be 54 MPa at -55°C. This stress is lower than the measured room temperature tensile yield stress of 75 MPa from Figure 2-31. Since the yield stress at -55°C would be even higher and the strength of the material scales with yielding, cracking of the coating is considered unlikely.

As with the foam encapsulation, only two conformal coating cases were investigated for unencapsulated components. Again, 0.005" thick unfilled Sylgard and unfilled 828/D230 were assumed for the coating materials. At -55°C, the peak maximum principal tensile stress in the Sylgard was calculated to be 5.6 MPa, and the peak maximum principal stress in the epoxy was calculated to be 56.0 MPa. As in Section 3.1.1, debonding of the elastomer coating may be expected, but cracking of the epoxy is unlikely.

3.2 Component Stresses

3.2.1 Epoxy Encapsulant

Effect of Elastomeric Coating

The elastomer coating cases investigated for 828/DEA/GMB epoxy over-encapsulated components included debonded polysulfide and Sylgard and contiguously meshed PMB filled polysulfide and GMB filled Sylgard. The effects of the elastomeric coating on component stresses can be seen in Figure 3-9, where PMB refers to PMB filled polysulfide and GMB to GMB filled Sylgard and 0.005 and 0.02 refer to the coating thickness in inches. In all cases, the capacitor experiences higher stresses than the resistor. This may be explained by the size and stiffness disparity between the components. The capacitor is larger and stiffer.

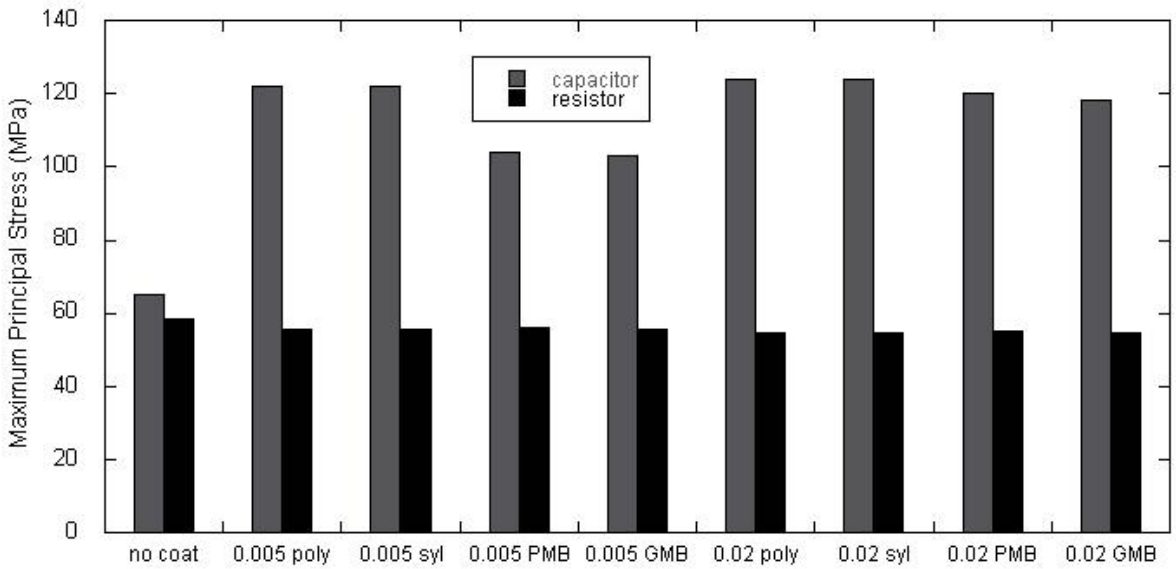

Figure 3-9: Peak ceramic maximum principal stress in capacitor and resistor for various elastomer coating cases with 0.2 hard filler volume fraction in underfill.

As can be seen in the figure, the coatings have little effect on the peak maximum principal tensile stress in the ceramic resistor. The highest resistor stress was calculated to be 58 MPa in the uncoated configuration and ~55 MPa in the coated configurations. A significant stress increase was experienced by the capacitor due to the addition of the coatings. The uncoated capacitor peak maximum principal stress was calculated to be 65 MPa. The coated ceramic stresses however ranged from ~103.5 MPa for the 0.005" thick filled elastomer cases to between 118 and 124 MPa for the other cases. It is worth noting that the capacitor experienced a worst case 92% increase in localized maximum principal stress by the addition of the elastomeric coating, and an 81.5% increase in stress as the best case.

After seeing the significant increase in the ceramic maximum principal stresses in the capacitor by the addition of the elastomeric coatings, one might wonder why a coating would be

necessary at all. To investigate further, the average hydrostatic stress in the ceramic for each component was calculated by summing the stress from each element and dividing by the number of ceramic elements. The results are plotted in Figure 3-10.

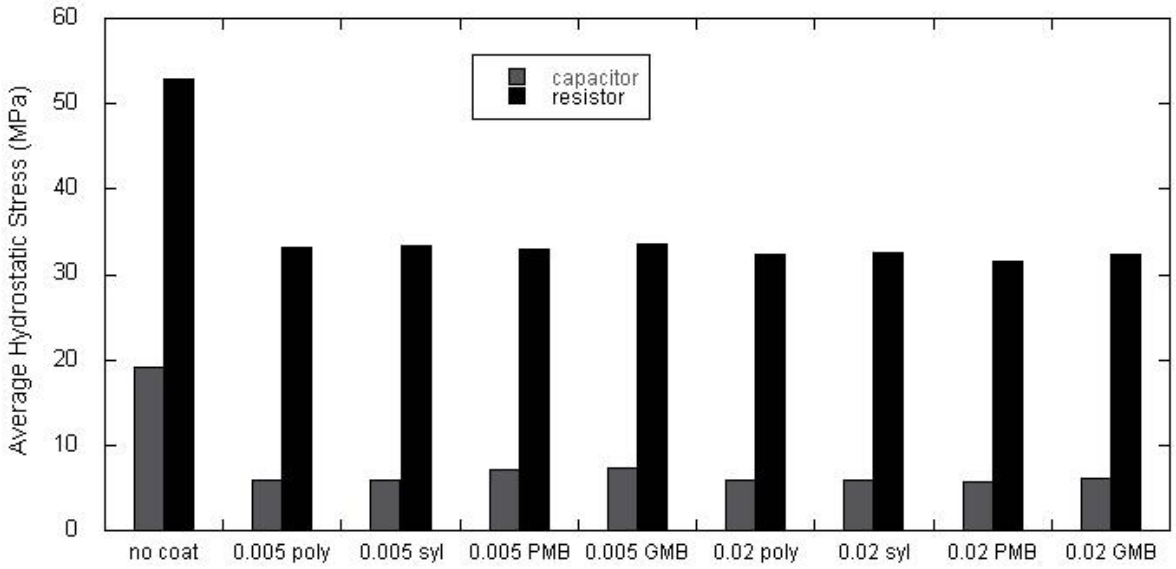

Figure 3-10: Average ceramic hydrostatic stress in capacitor and resistor for various elastomer coating cases with 0.2 hard filler volume fraction.

As can be seen in the figure, the hydrostatic stress is significantly decreased by the addition of the coating. The average stress for the capacitor decreased from 19 MPa to 6 MPa, and decreased from 53 MPa to 33 MPa for the resistor. The elastomer coating material and thickness do not appear to significantly affect the stresses in the ceramic.

Stress contour plots illustrating the effect of the elastomeric coating can be seen in Figure 3-11. In the figure, the calculated maximum principal stress increases from 65 MPa to 135 MPa with the addition of the coating. The hydrostatic stress at the center of the capacitor however decreases from 40 MPa to 4 MPa with the addition of the coating. These results imply that coatings should be applied to components that are sensitive to externally applied loading. In some components, externally applied stress may result in electrical “drift” or even cracking if the component is hollow.

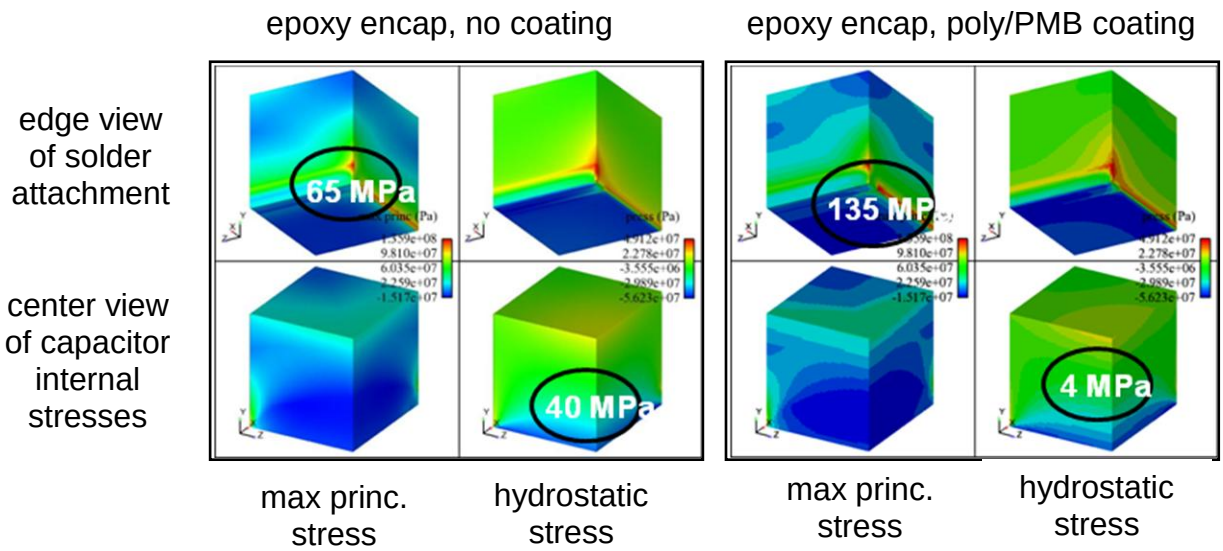

Figure 3-11: Stress contour plots for encapsulated ceramic capacitor with and without elastomeric stress relief coating.

Effect of Underfill Filler Volume Fraction

The effect on peak maximum principal stress in the ceramic component for various underfill filler volume fractions can be seen in Figure 3-12 for the uncoated, epoxy encapsulated components.

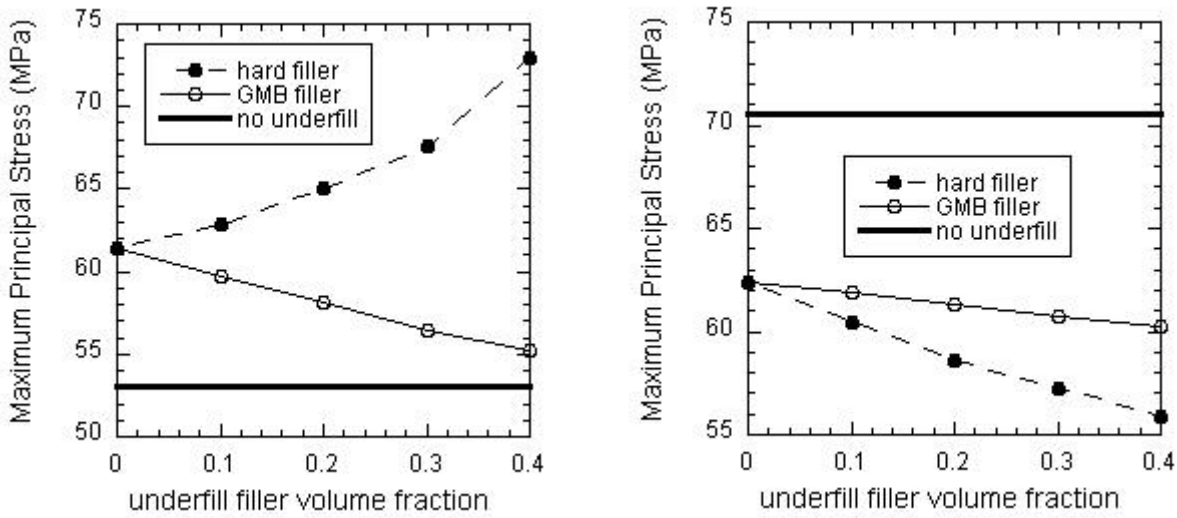

Figure 3-12: Ceramic maximum principal stress for various underfill filler volume fractions in epoxy encapsulated capacitor (left) and resistor (right) with no coating.

As seen in the figure, some "trends" may be identified. For both the resistor and capacitor, adding GMB filler to the underfill almost linearly reduced the ceramic stress. The capacitor peak maximum principal stress was reduced from 61.3 MPa to 55.2 MPa, and the resistor peak stress was reduced from 62.4 MPa to 60.2 MPa with the addition of 40% GMB filler. The solid hard filler results were more complicated. The addition of hard filler to the capacitor increased the ceramic stress from 61.3 MPa to 72.9 MPa, while adding hard filler to the resistor decreased the stress from 62.4 MPa to 55.9 MPa. The addition of GMB filler to the underfill reduces the underfill CTE but only slightly changes the moduli, resulting lower thermal stress. Adding hard filler reduces the CTE, but increases the moduli. This coupled with the stiffer capacitor geometry results in a higher stress state. The loss of stiffness produced by the absence of underfill increases the resistor stresses noticeably.

Changes in the peak maximum principal stress for the capacitor and resistor due to the addition of an underfill and filler are depicted in Figure 3-13 and Figure 3-14 for elastomer coated, epoxy encapsulated components. Results were calculated for all the various elastomer coating cases however, PMB polysulfide is the only coating presented in the plots. The results from the debonded unfilled elastomer coatings and GMB filled Sylgard were found to be very similar to those of the PMB polysulfide.

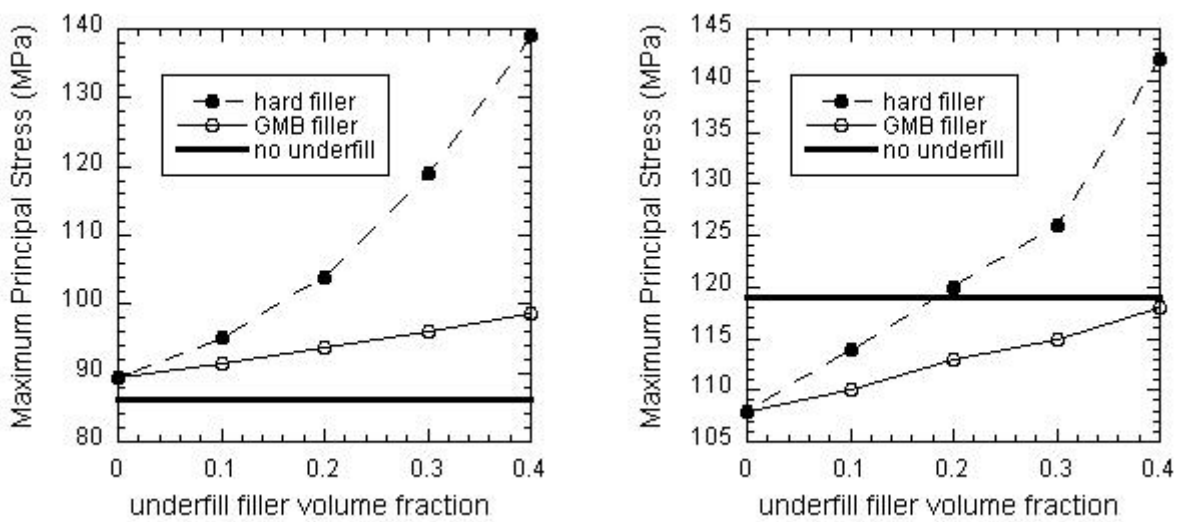

Figure 3-13: Capacitor maximum principal stress for various underfill filler volume fractions with 0.005" (left) and 0.02" (right) thick PMB polysulfide coatings over-encapsulated with epoxy.

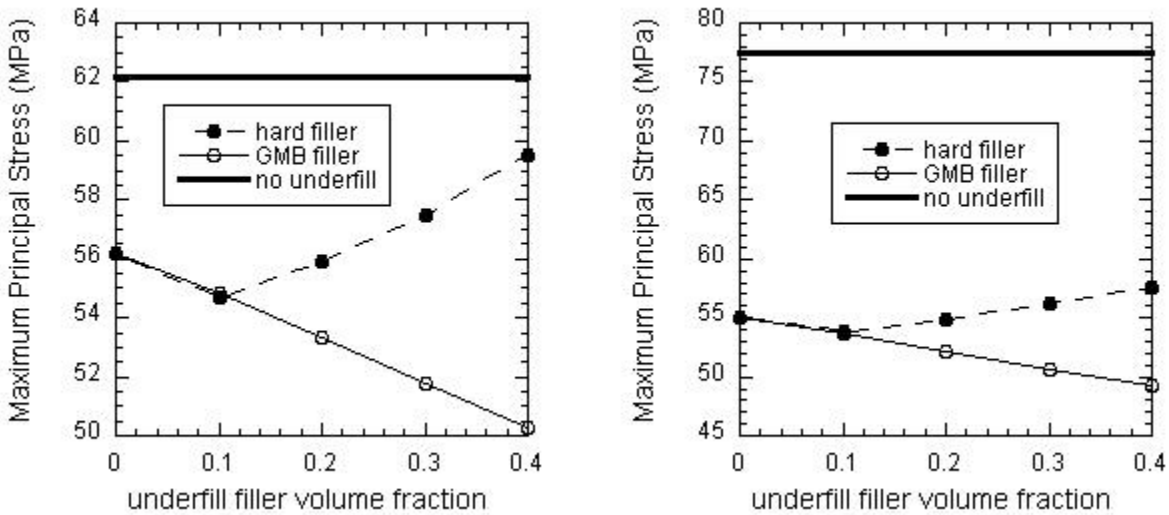

Figure 3-14: Resistor maximum principal stress for various underfill filler volume fractions with 0.005" (left) and 0.02" (right) thick PMB polysulfide coatings over-encapsulated with epoxy.

As seen in the figures, "trends" are not necessarily obvious. One unusual trend in the resistor data is the decrease in stress from the unfilled case to the 10% hard filled case followed by a consistent increase in stress with the addition of more hard filler. This indicates an optimum hard filler volume fraction of 10% for this particular geometry and encapsulation state. Other such optimums can be identified by further analyses involving other over-encapsulated and unencapsulated states. Another unusual observation is that for the capacitor, the addition of filler to the underfill in all cases with the elastomer coating increases the component stress. With the resistor however, the addition of GMB filler decreases the stress in the ceramic component. The opposite trends lead one to believe that "general" design guides with respect to optimizing underfill filler volume fraction may not exist. This implies that details likely matter.

Adding an underfill to the resistor, decreased the peak maximum principal stress from 62 MPa to as low as 50 MPa for the 40% FVF GMB case with the thin coating (Figure 3-14, left), and decreased the stress from 77.5 MPa to 49.5 MPa for the 40% FVF GMB case with the thick coating (Figure 3-14, right). The capacitor however, had more mixed results. The addition of underfill resulted consistently in higher stress with the thin coating, the best case being an increase from 86 MPa to 89 MPa for the unfilled underfill, and the worst case being an increase to 140 MPa for the 40% FVF solid hard underfill (Figure 3-13, left). A stress decrease from 119 MPa to 107 MPa was experienced with the addition of unfilled underfill for the thick coating, however at ~20% hard filler, the stress exceeded the no underfill case and increased to 144 MPa with a 40% FVF solid hard filled underfill (Figure 3-13, right).

3.2.2 Foam Encapsulant / No Encapsulant

Effect of Elastomeric or Epoxy Coating

A significant decrease in ceramic stress was experienced by omitting epoxy encapsulation. Figure 3-15 depicts the peak ceramic maximum principal stress in the capacitor and resistor with a 20% hard filled underfill for various coating and encapsulation configurations. The highest stress calculated was found to be 65.6MPa for the foam encapsulated, Sylgard coated capacitor. By comparison, a similarly configured epoxy encapsulated capacitor resulted in a peak stress of 122 MPa, an 86% increase. As expected, little difference was found between the stress results for the unencapsulated uncoated and elastomer coated cases. Roughly a 32% stress decrease was realized by adding an epoxy coating to both the resistor and capacitor regardless of encapsulation. A slight increase in stress was experienced with addition of the Sylgard coating to the foam encapsulated components. This however is most likely an effect of assuming a contiguous mesh even though debonding may occur. As stated in Section 3.1.2, the tensile stresses in the Sylgard are ~5 MPa.

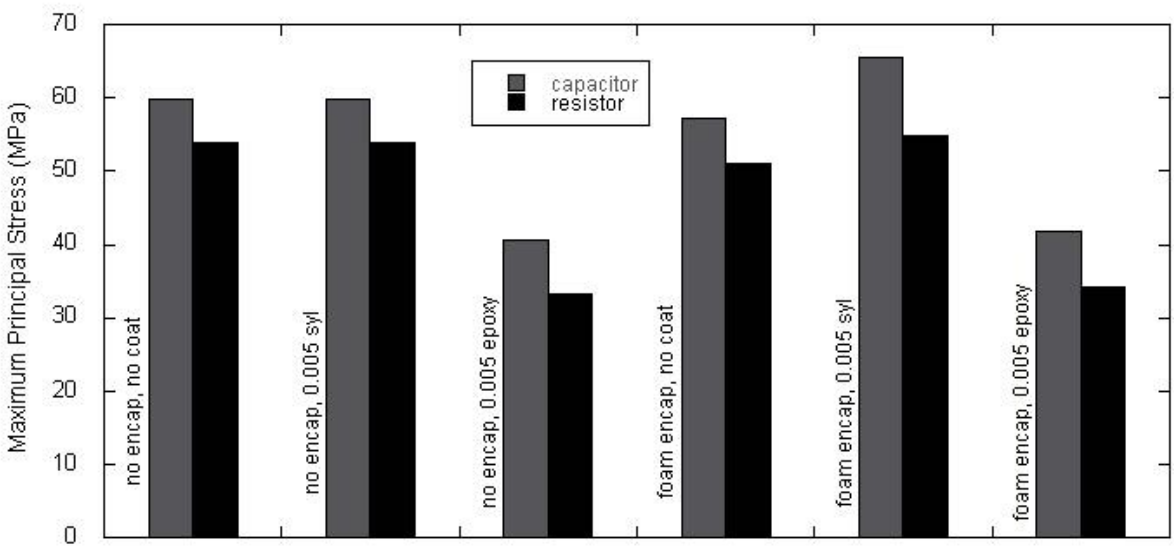

Figure 3-15: Peak ceramic maximum principal stress in capacitor and resistor for various encapsulation and elastomer coating cases with 20% hard filler in underfill.

Effect of Underfill Filler Volume Fraction

The stress results for the elastomer coated unencapsulated components were not plotted because they were almost identical to those of the uncoated components. The stress results for the unencapsulated capacitor and resistor are plotted in Figure 3-16 and Figure 3-17 respectively. As with the 828/DEA/GMB epoxy encapsulated components, design guidelines for generic components are not immediately apparent. In the left plot of Figure 3-16, it can be seen that the addition of an unfilled underfill to the unencapsulated capacitor significantly decreases the peak

maximum principal stress from 73 MPa to 57 MPa. Adding filler to the underfill however linearly increases the stress to 63 MPa for hard filled and 61 MPa for GMB filled underfills. An opposite trend, however, was experienced by the resistor in the left plot of Figure 3-17, where the stress in the resistor increases from 50.8 MPa to 57.5 MPa with the addition of an unfilled underfill, but continuously decreased with addition of filler to 52.4 MPa for a 40% FVF hard filled underfill and 53.9 MPa for a 40% FVF GMB filled underfill.

The stress response due to the application of a 0.005" thick unfilled epoxy coating was even more unpredictable. While the stress increased with the addition of filler for the unencapsulated, uncoated capacitor, the opposite trend was exhibited with the addition of an epoxy coating. In the right plot of Figure 3-16, it can be seen that the peak stress decreases from 45 MPa with an unfilled underfill to lows of 39.8 MPa for hard filled and 40.6 MPa for GMB filled underfills. The peak ceramic stress with no underfill was calculated to be 41.8 MPa. This result was unusual because it lies within the span of the stresses achieved by varying the underfill filler volume fraction from 0 to 40%. The results for the epoxy coated resistor were also interesting. In the right plot of Figure 3-17, optimum filler volume fractions for stress reduction were found for both hard and GMB filled underfills. From a peak stress of 36 MPa for an unfilled underfill, a 20% hard filled underfill reduced the stress to 33 MPa, and a 30% GMB filled underfill reduced the stress to 31.5 MPa. The peak ceramic stress for the resistor with no underfill was calculated to be 31.5 MPa as well.

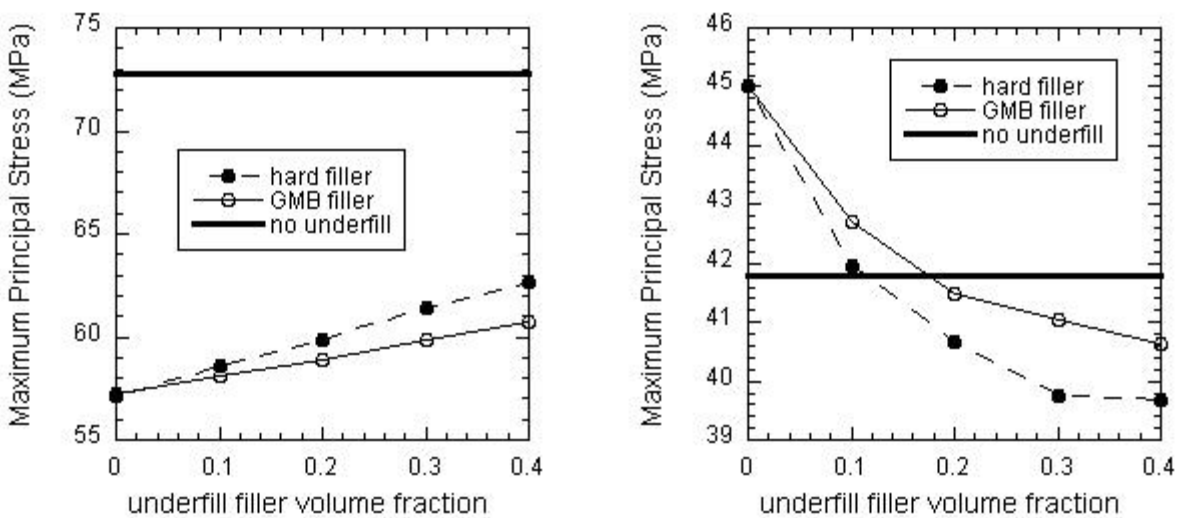

Figure 3-16: Unencapsulated capacitor maximum principal stress for various underfill filler volume fractions with no coating (left) and 0.005" thick unfilled epoxy coating (right).

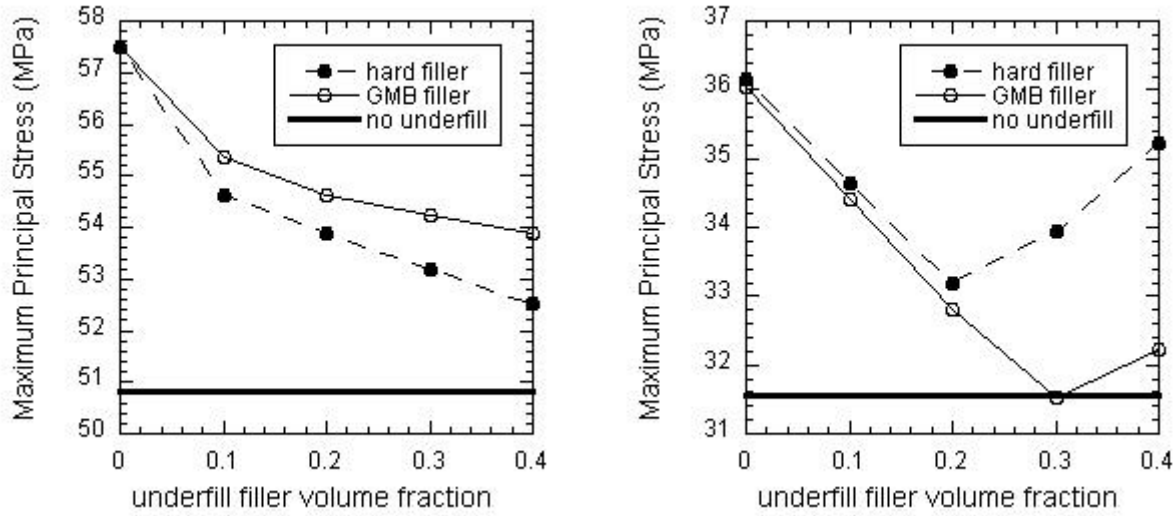

Figure 3-17: Unencapsulated resistor maximum principal stress for various underfill filler volume fractions with no coating (left) and 0.005" thick unfilled epoxy coating (right).

Plots of the peak maximum principal stresses in the capacitor and resistor for the foam encapsulated cases can be seen in Figure 3-18 and Figure 3-19, respectively. The ceramic stress results from the foam encapsulated and unencapsulated components are fairly similar, especially the results without the epoxy coating (left plots). The capacitor experienced a decrease in stress from 63.3 MPa to 53.7 MPa with the addition of an unfilled underfill, but a linear increase in stress from 53.7 MPa to 57.9 MPa with the addition of 40% FVF GMB, and an increase to 61.0 MPa with the addition of 40% hard filler (Figure 3-18, left). The resistor experienced an increase in stress from 49.3 MPa to 53.4 MPa with the addition of an unfilled underfill, but a decrease in stress from 53.4 MPa to 51.0 MPa with the addition of 40% FVF GMB, and a decrease to 49.6 MPa with the addition of 40% hard filler (Figure 3-19, left).

One difference between the unencapsulated and foam encapsulated cases was the lack of an optimum stress reducing filler volume fraction in the underfill. For the foam encapsulated cases with the epoxy coating, stress reduction linearly continued in the ceramic with the addition of filler to the underfill. The addition of an unfilled underfill increased the ceramic stress in the capacitor from 37.8 MPa to 46.8 MPa; however, the addition of 40% FVF hard filler to the underfill linearly decreased the stress to 35.6 MPa. The addition of 40% FVF GMB to the underfill linearly decreased the stress to 38.4 MPa (Figure 3-18, right). The addition of an unfilled underfill to the resistor increased the ceramic stress from 27.2 MPa to 37.3 MPa, but the addition of 40% FVF hard filler to the underfill linearly decreased the stress to 30.4 MPa, and the addition of 40% FVF GMB to the underfill linearly decreased the stress to 31.2 MPa (Figure 3-19, right).

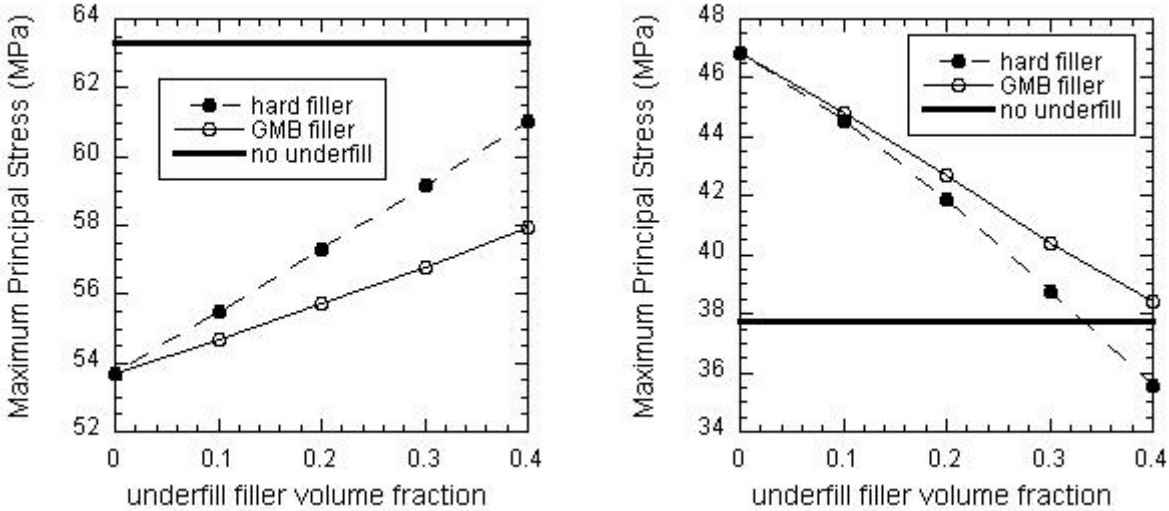

Figure 3-18: Foam encapsulated capacitor maximum principal stress for various underfill filler volume fractions with no coating (left) and 0.005" thick unfilled epoxy coating (right).

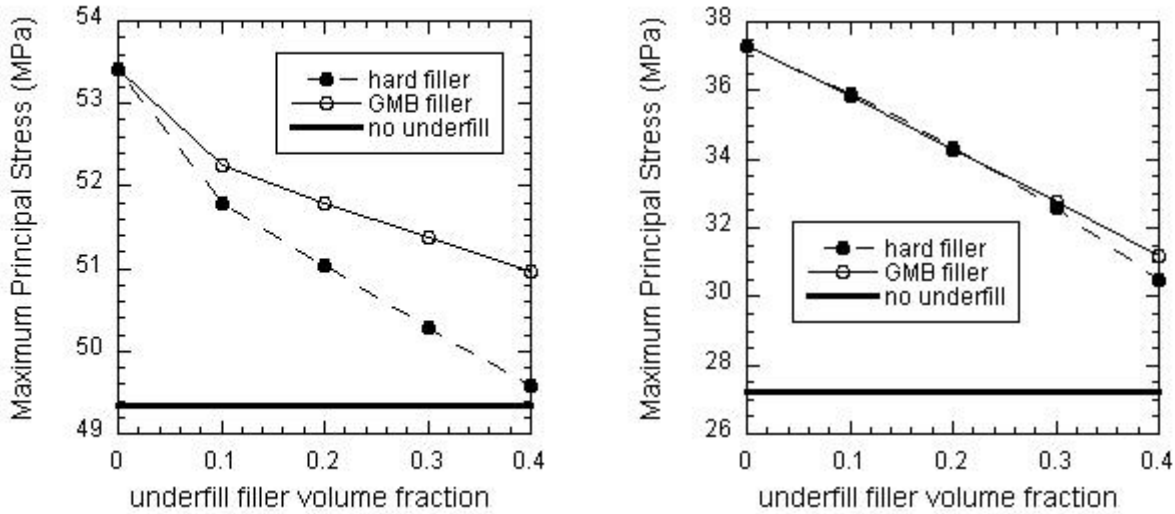

Figure 3-19: Foam encapsulated resistor maximum principal stress for various underfill filler volume fractions with no coating (left) and 0.005" thick unfilled epoxy coating (right).

While the 0.005" Sylgard results are not plotted, it was found that there was ~13% increase in stress by adding the 0.005" Sylgard coating to the foam encapsulated capacitor. This is consistent for all of the underfill cases. For the resistor, it was found that there was a ~7% increase in stress by adding the 0.005" Sylgard coating to the foam encapsulation. Note however, these results assume a contiguous mesh. This was also consistent for all of the underfill cases except for the unencapsulated case where there was only a 2.7% increase.

3.3 Solder Fatigue

The thermal-mechanical fatigue life of the solder joints was assessed using the Coffin-Manson fatigue criterion discussed in Section 2.5 based on the change in plastic strain increment accrued in the eutectic SnPb over a thermal cycle from -55ºC to 71ºC and back to -55ºC. The solder fatigue life is defined as the number of thermal cycles required to initiate a crack in the solder.

3.3.1 Epoxy Encapsulant

Effect of Elastomeric Coating

The effects of elastomer coatings on solder fatigue life for epoxy encapsulated components were also studied. As in Section 3.2.1, the elastomer coating cases for 828/DEA/GMB epoxy over-encapsulated components included debonded polysulfide and Sylgard and contiguously meshed PMB filled polysulfide and GMB filled Sylgard. The effects of the elastomeric coating can be seen in Figure 3-20, where PMB refers to PMB filled polysulfide and GMB to GMB filled Sylgard and 0.005 and 0.02 refer to the coating thickness in inches. Interestingly, the calculated fatigue lives in all the cases are fairly similar even with the size/stiffness disparity of the components. This indicates that the surrounding epoxy is the dominating factor with respect to solder fatigue life.

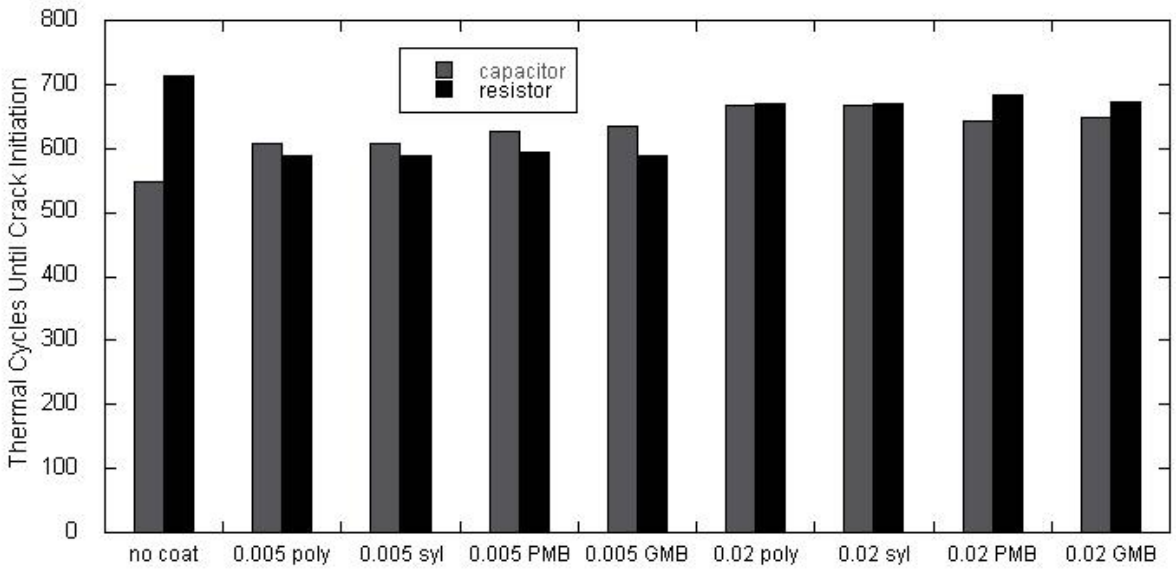

Figure 3-20: Thermal cycles until solder crack initiation for epoxy encapsulated capacitor and resistor with various elastomer coating cases and 20% hard filler in the underfill.

As can be seen in the figure, the coatings have a minimal effect on the calculated fatigue life in either the capacitor or resistor. For the capacitor, the highest fatigue life was calculated to be 549 cycles in the uncoated configuration and 668 cycles in the coated configurations. The minimum coated capacitor fatigue life was calculated to be 609 cycles. The highest fatigue life

for the resistor was calculated to be 714 cycles for the uncoated configuration and 684 cycles in the coated configurations, and the minimum fatigue life was calculated to be 588 cycles. It is interesting to note that the addition of the elastomer coatings increased the fatigue life of the capacitor by as much as 22%, but decreased the life of the resistor by as much as 18%.

Effect of Underfill Filler Volume Fraction

The effect of underfill filler volume fraction on solder fatigue for the capacitor and resistor can be seen in Figure 3-21. In this plot, the components are epoxy encapsulated with no conformal coating.

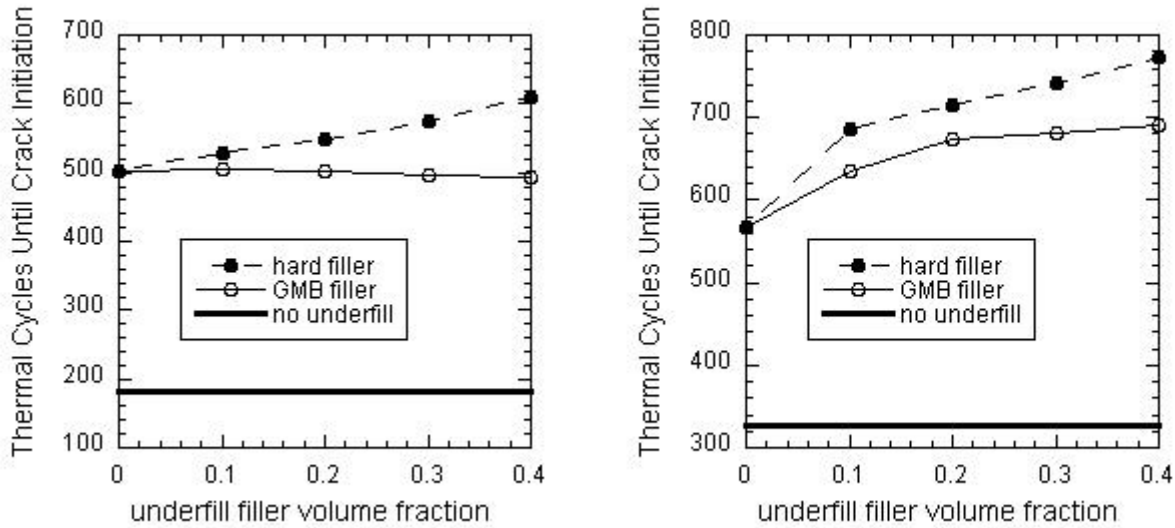

Figure 3-21: Thermal cycles until solder crack initiation for various underfill filler volume fractions in epoxy encapsulated capacitor (left) and resistor (right) with no coating.

One obvious "trend" can immediately be identified in the figure. A void under the component significantly reduces the fatigue life. By adding an unfilled underfill, the fatigue life for the capacitor was increased by 177% from 181 cycles to 501 cycles, and the fatigue life for the resistor was increased by 73% from 328 cycles to 566 cycles. The addition of hard filler linearly increased the fatigue life by another 21% with an increase to 609 cycles with 40% FVF, but the addition of GMB filler to the capacitor underfill had almost no effect on the fatigue life. The resistor however experienced an increase in fatigue life with the addition of any filler to the underfill. The addition of 40% FVF solid hard filler increased the fatigue life by 37% from 566 cycles to 773 cycles, and the addition of 40% FVF GMB increased the fatigue life by 22% to 690 cycles.

The predicted fatigue lives for the elastomer coated capacitor and resistor due to the addition of an underfill and filler are depicted in Figure 3-22 and Figure 3-23. Being that the results from the debonded unfilled elastomer coatings and GMB filled Sylgard were very similar to those of the PMB polysulfide, PMB polysulfide was the only coating case presented in the plots (as in previous sections).

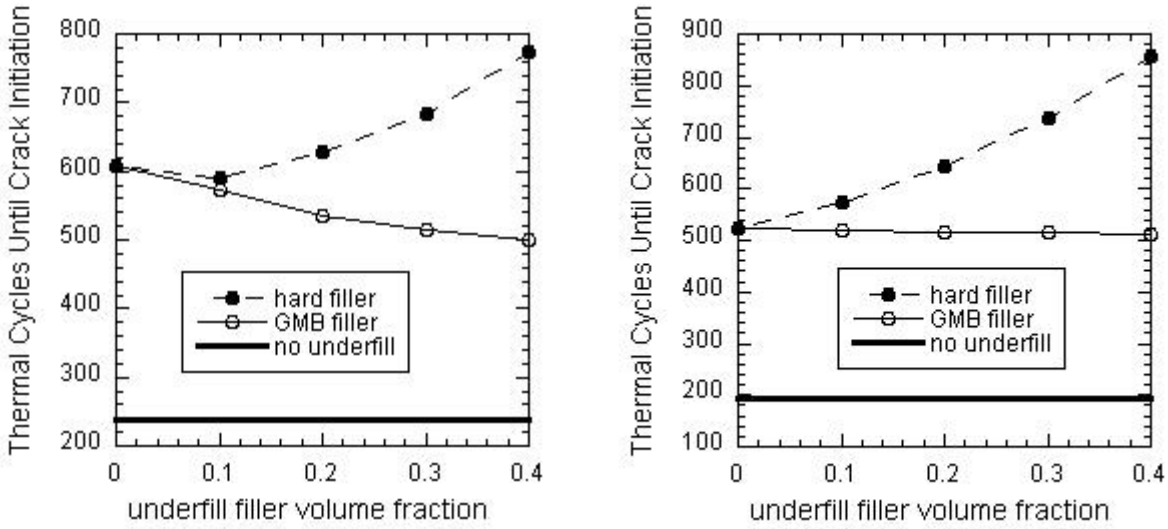

Figure 3-22: Capacitor thermal cycles until solder crack initiation for various underfill filler volume fractions with 0.005" (left) and 0.02" (right) thick PMB polysulfide coatings over-encapsulated with epoxy.

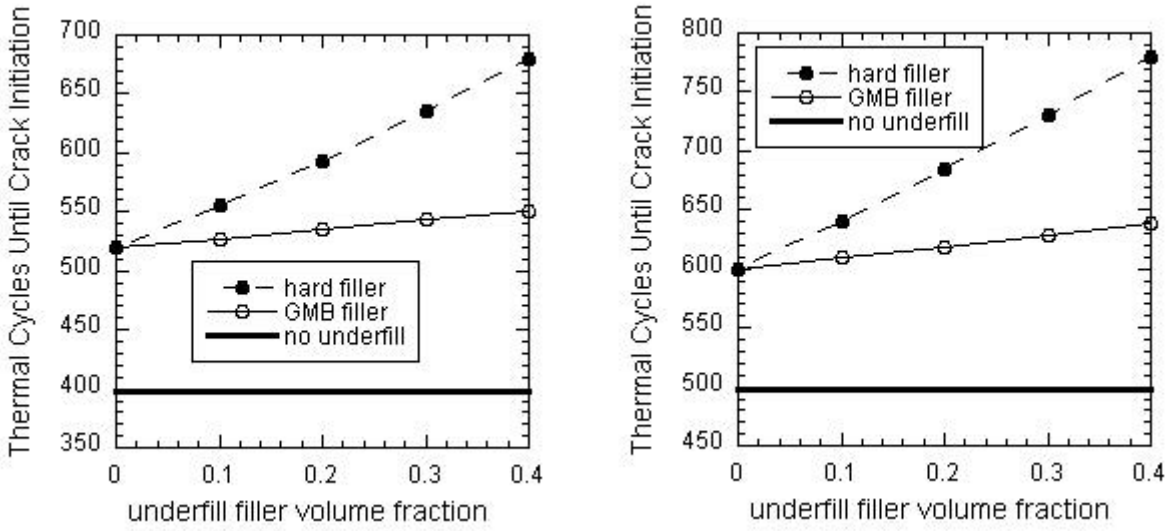

Figure 3-23: Resistor thermal cycles until solder crack initiation for various underfill filler volume fractions with 0.005" (left) and 0.02" (right) thick PMB polysulfide coatings over-encapsulated with epoxy.

As seen in the figures, some "trends" may be identified. In all of the cases, adding even an unfilled underfill increased the fatigue life, with the best case demonstrating an improvement from 239 cycles to 609 cycles for the thin coated capacitor, and the worst case improving from 497 cycles to 600 cycles for the thick coated resistor. Note that the "no underfill" case assumes a void under the component.

For both the capacitor and resistor, increasing the hard filler volume fraction increased the fatigue life. Increasing the GMB filler volume fraction slightly increased the fatigue life for the resistor, but slightly decreased the fatigue life of the capacitor. The resistor fatigue life increase for both coating cases was linear with the addition of filler to the underfill (Figure 3-23). By adding 40% FVF hard filler, a 30% increase in fatigue life was realized for both coating thicknesses, while the addition of 40% GMB filler resulted in a 6% increase in fatigue life. The capacitor results were slightly more complicated. While the fatigue life increased with the addition of solid hard filler, the increase was not linear with respect to the filler fraction. The thin coated capacitor ultimately achieved a 27% increase in fatigue life as the filler was increased to 40% FVF (Figure 3-22, left), while the thick coated capacitor life increased by 65% (Figure 3-22, right). The addition of 40% GMB filler to the underfill resulted in a linear 2% decrease in the fatigue life for the thick coated capacitor (Figure 3-22, right), and an 18% decrease for the thin coated capacitor (Figure 3-22, left).

3.3.2 Foam Encapsulant / No Encapsulant

Effect of Elastomeric or Epoxy Coating

While most of the epoxy encapsulated components in Figure 3-20 possess fatigue lives on the order of 600 cycles, Figure 3-24 tells a much different story.

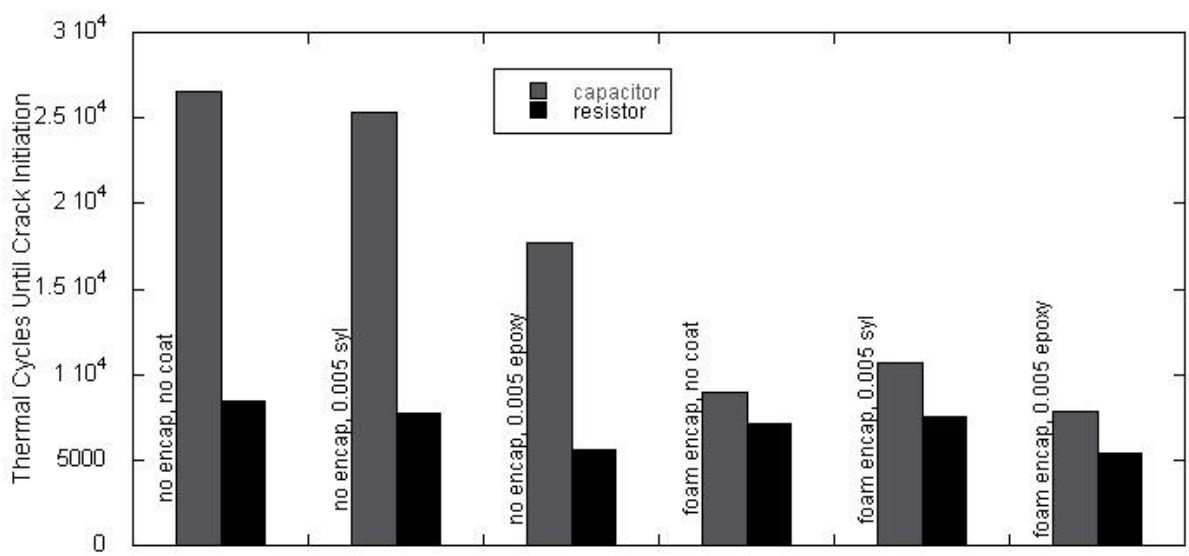

Figure 3-24: Thermal cycles until solder crack initiation for capacitor and resistor with various encapsulation/elastomer coating cases and 20% hard filler in the underfill.

As seen in the figure, unencapsulated and foam encapsulated components achieve at least an order of magnitude increase in fatigue lives. With the 20% hard filled underfill, the unencapsulated, uncoated capacitor achieved the longest predicted fatigue life of 26,513 cycles, and the shortest fatigue life of 5,361 cycles was predicted for the foam encapsulated, epoxy

coated resistor. The most noticeable difference between the unencapsulated and the foam encapsulated components was the ~60% decrease in fatigue life for the capacitors with the addition of foam encapsulation. The addition of the epoxy coating also reduced the fatigue lives of both the capacitor and resistor by ~30%. The Sylgard coating had a minimal effect on the fatigue lives.

Effect of Underfill Filler Volume Fraction

The predicted solder fatigue lives for the unencapsulated and foam encapsulated components are plotted in Figure 3-25 through Figure 3-28 for a range of underfill filler volume fractions. As in previous sections, the elastomer coated unencapsulated component results are not plotted because they are very similar to those of the uncoated components.

Like the 828/DEA/GMB epoxy encapsulated components, design "trends" for generic unencapsulated and foam encapsulated components may be identified with respect to solder fatigue life. In each figure, the addition of an unfilled underfill reduces the fatigue life from the no underfill case. The largest decrease in fatigue life was a 49% drop from 5,497 cycles to 2,821 cycles for the foam encapsulated epoxy coated resistor (Figure 3-28, right) with the addition of the unfilled underfill, and the smallest decrease was experienced by the unencapsulated epoxy coated capacitor, with a 28% drop from 10,584 cycles to 7,586 cycles (Figure 3-25, right). The addition of GMB to the underfill consistently increased the fatigue life. In the best case, the fatigue life for the unencapsulated uncoated capacitor (Figure 3-25, left) was increased from 10,556 cycles by 187% to 30,355 cycles with the addition of 40% FVF GMB to the underfill, and the worst cases improvement was an 89% increase from 4,461 cycles to 8712 cycles for the unencapsulated epoxy coated resistor (Figure 3-26, right) with 40% FVF GMB in the underfill. The addition of solid hard filler to the underfill increases the fatigue life to a point, after which addition of more filler reduces the fatigue life. 20% to 30% FVF hard filler appears to be the optimum. The best improvement from hard filler was achieved by the unencapsulated uncoated capacitor (Figure 3-25, left) by adding 20% FVF hard filler to increase the fatigue life by 151% from 10,566 cycles to 26,513 cycles. The smallest improvement was obtained by the unencapsulated uncoated resistor (Figure 3-26, left) by adding 20% FVF hard filler to increase the fatigue life by 89% from 4459 cycles to 8405 cycles.

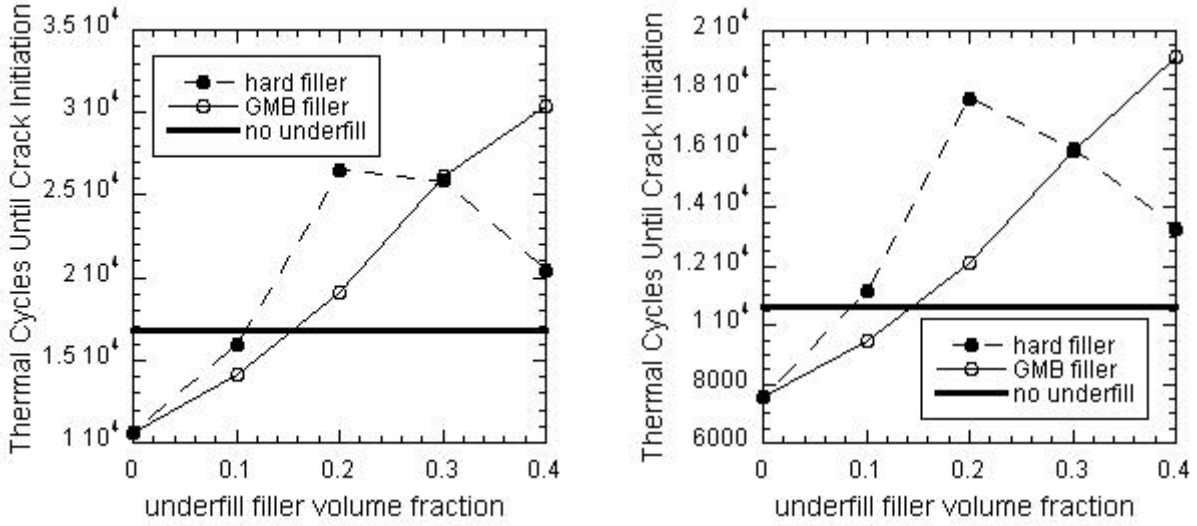

Figure 3-25: Unencapsulated capacitor thermal cycles until solder crack initiation for various underfill filler volume fractions with no coating (left) and 0.005" thick unfilled epoxy coating (right).

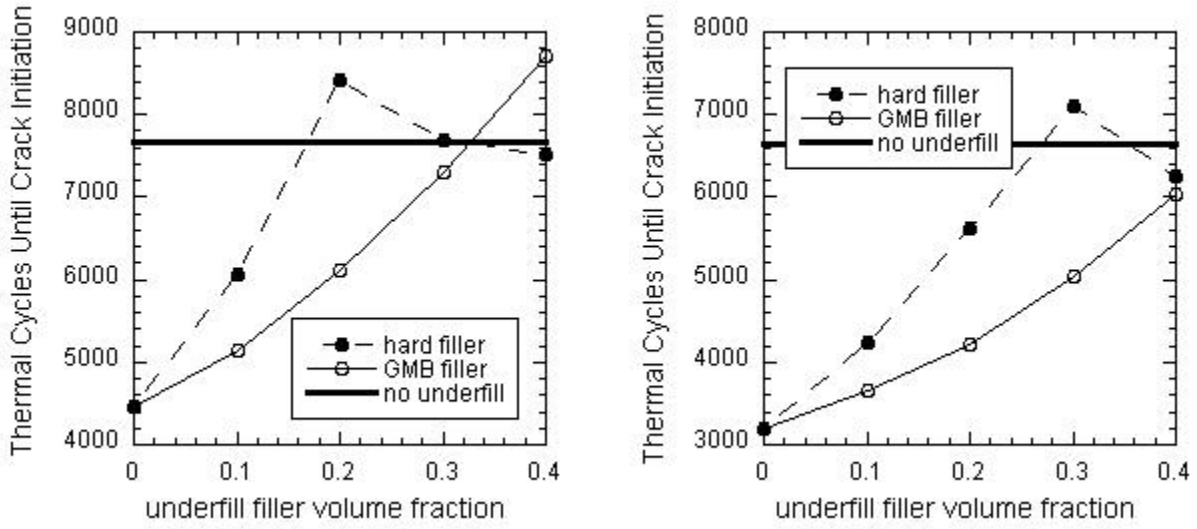

Figure 3-26: Unencapsulated resistor thermal cycles until solder crack initiation for various underfill filler volume fractions with no coating (left) and 0.005" thick unfilled epoxy coating (right).

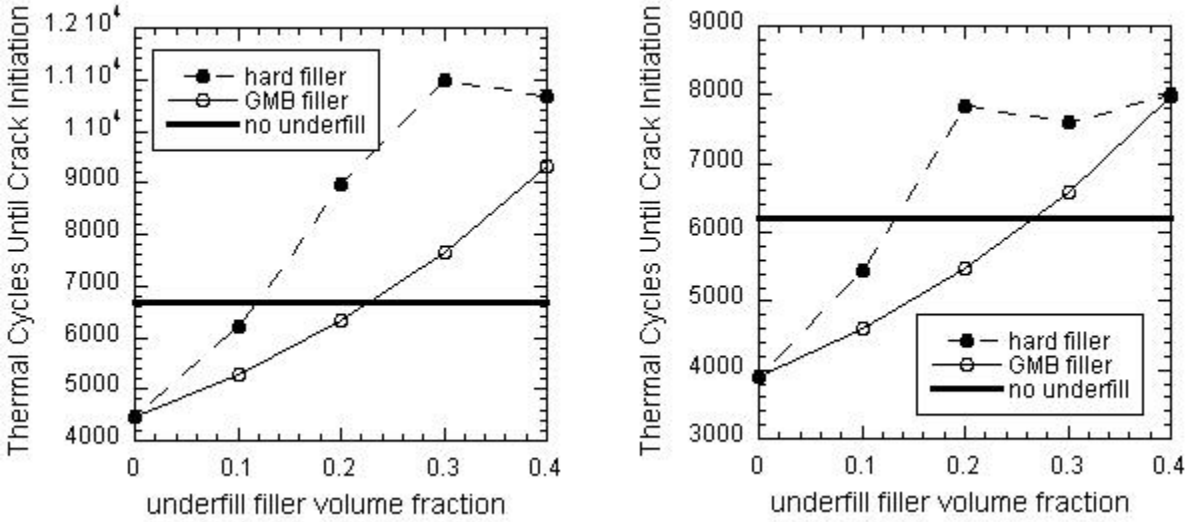

Figure 3-27: Foam encapsulated capacitor thermal cycles until solder crack initiation for various underfill filler volume fractions with no coating (left) and 0.005" thick unfilled epoxy coating (right).

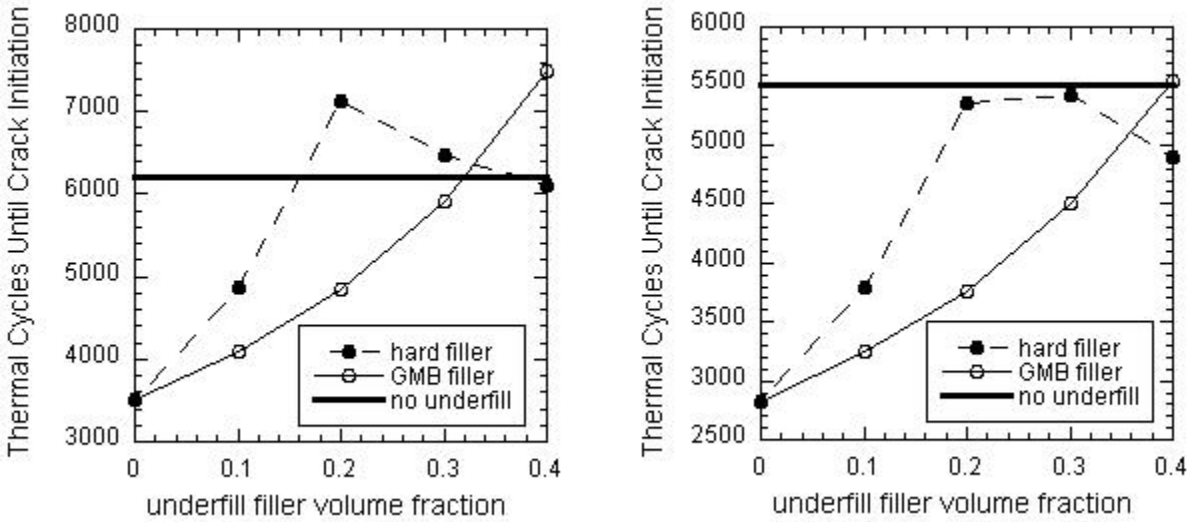

Figure 3-28: Foam encapsulated resistor thermal cycles until solder crack initiation for various underfill filler volume fractions with no coating (left) and 0.005" thick unfilled epoxy coating (right).

3.4 Underfill Stresses

3.4.1 Epoxy Encapsulant

Effect of Elastomeric Coating

The underfill maximum principal stress for epoxy encapsulated components was also studied. Again, 828/DEA/GMB epoxy over-encapsulated components coated with debonded polysulfide and Sylgard and contiguously meshed PMB filled polysulfide and GMB filled Sylgard were assumed. The effects of the elastomeric coatings and thicknesses can be seen in Figure 3-29. In the graph, PMB refers to PMB filled polysulfide and GMB to GMB filled Sylgard and 0.005 and 0.02 refer to the coating thickness in inches.

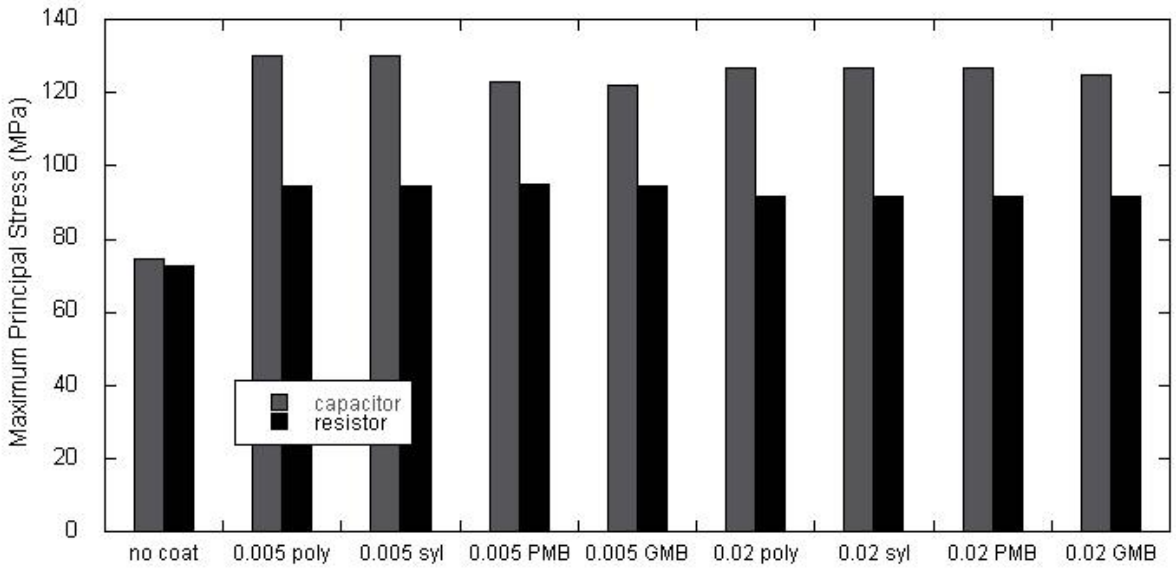

Figure 3-29: Underfill maximum principal stress for epoxy encapsulated capacitor and resistor with various elastomer coating cases and 20% hard filler in the underfill.

As indicated in the figure, coating material and thickness changes did not significantly affect the underfill stress, however including a coating significantly increased the underfill stress from the uncoated configuration. The peak maximum principal stress in the underfill increased ~70 % from 74.4 MPa to an average of 126 MPa for the capacitor, and 29% from 72.5 MPa to an average of 93 MPa for the resistor.

Effect of Underfill Filler Volume Fraction

The effect on peak maximum principal stress in the underfill for various underfill filler volume fractions can be seen in Figure 3-30 for the uncoated, epoxy encapsulated components.

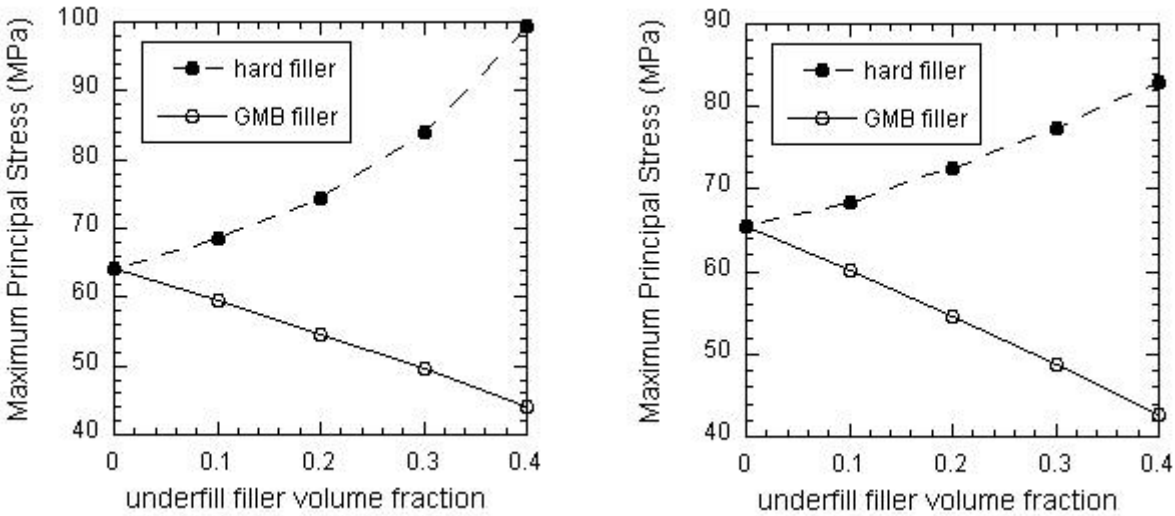

Figure 3-30: Underfill maximum principal stress for various underfill filler volume fractions in epoxy encapsulated capacitor (left) and resistor (right) with no coating.

Again, some "trends" may be identified from the figure. For both the resistor and capacitor, adding GMB filler to the underfill almost linearly reduced the underfill stress. The capacitor peak maximum principal stress was reduced 31% from 64.2 MPa to 44.2 MPa, and the resistor peak stress was reduced 35% from 65.6 MPa to 42.6 MPa with the addition of 40% GMB filler. The solid hard filler results indicated an opposite trend. The addition of hard filler to the capacitor increased the ceramic stress 55% from 64.2 MPa to 99.5 MPa, while adding hard filler to the resistor decreased the stress 26% from 65.6 MPa to 82.9 MPa. These results are very similar to those for the ceramic component stresses, and the explanation in Section 3.2.1 applies.

The predicted underfill maximum principal stress for the capacitor and resistor due to the addition of an underfill and filler are depicted in Figure 3-31 and Figure 3-32. As in previous sections, only the PMB polysulfide coating cases are presented in the plots because the results are so similar for the various coating cases.

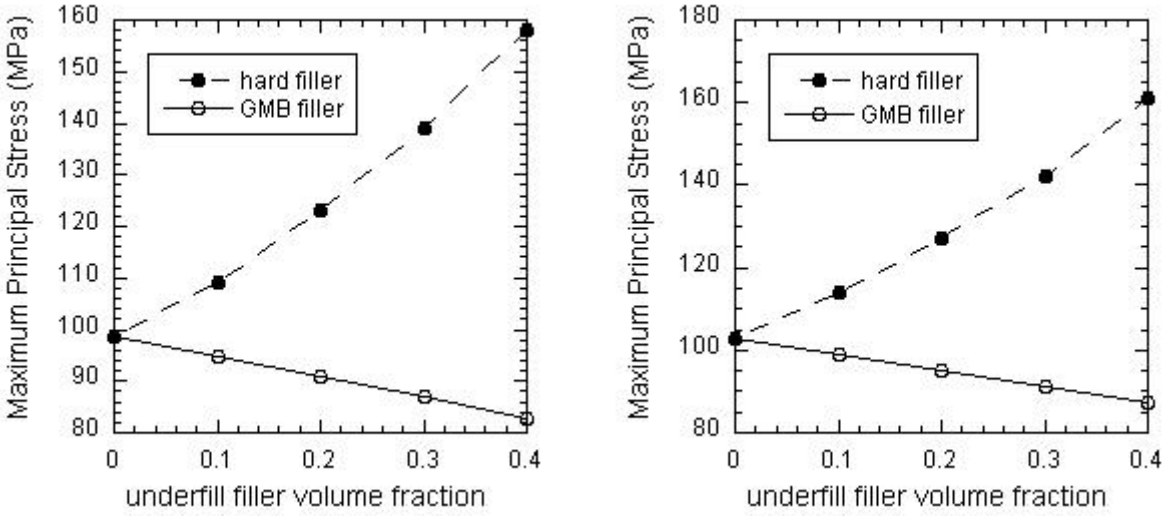

Figure 3-31: Capacitor underfill maximum principal stress for various underfill filler volume fractions with 0.005" (left) and 0.02" (right) thick PMB polysulfide coatings over-encapsulated with epoxy.

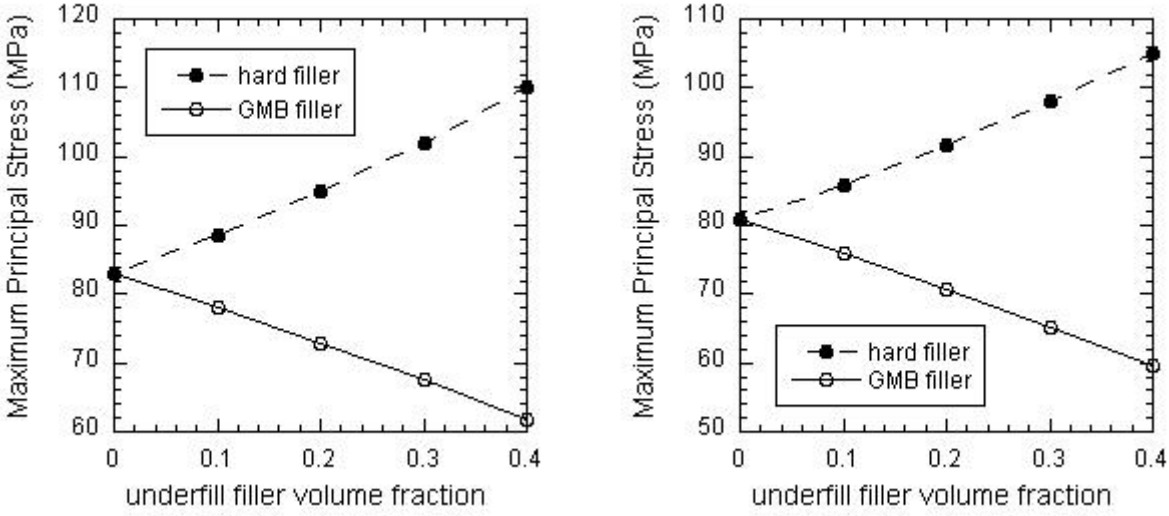

Figure 3-32: Resistor underfill maximum principal stress for various underfill filler volume fractions with 0.005" (left) and 0.02" (right) thick PMB polysulfide coatings over-encapsulated with epoxy.

As seen in the figures, obvious "trends" appear. In all cases adding GMB filler to the underfill linearly decreases the underfill stress while adding solid hard filler almost linearly increases the stress. Adding 40% FVF solid hard filler to the capacitor underfill increased the stress from 98.8 MPa to 158 MP, or 60%, while adding 40% FVF GMB filler to the underfill decreased the stress by 16% to 82.6 MPa (Figure 3-31, left). The trends were similar for the resistor. By adding 40% FVF solid hard filler to the resistor underfill, the maximum principal stress increased 33% from 83.0 MPa to 110 MP, while adding 40% FVF GMB filler to the underfill decreased the stress by 23% to 61.8 MPa (Figure 3-32, left).

In addition, high underfill residual stress affecting dynamic survivability, fatigue and creep failure of the underfill also should be considered. Shown in Figure 3-33 is the maximum principal stress vs. maximum principal strain for underfill elements subjected to thermal cycles. The components investigated consisted of an 828/DEA/GMB epoxy encapsulated, 0.02" thick PMB polysulfide coated capacitor and resistor. The FVF for the underfills were 40% for both the GMB and hard fillers. As can be seen in the figure, permanent strain in the underfill increased significantly for the capacitor model during a thermal cycle, and less for the resistor model.

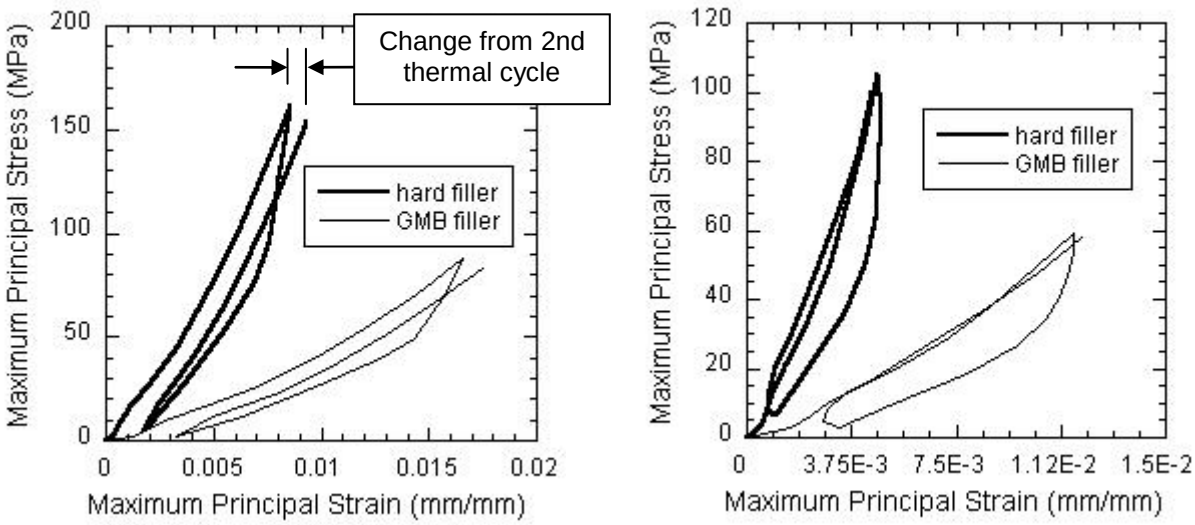

Figure 3-33: Epoxy encapsulated capacitor (left) and resistor (right) underfill maximum principal stress vs. maximum principal strain in underfill element.

The strain increase due to one thermal for the capacitor was found to be ~0.001 for both the hard filler and GMB fillers, indicating that ~200 thermal cycles could lead to crack initiation if strain to failure was assumed to be 20% (assuming the same strain per thermal cycle). For the resistor, no permanent strain increase was realized due to the thermal cycle for the hard filled underfill case, however a strain increment of 3.5E-4 was calculated for the GMB filled underfill, or ~570 thermal cycles to crack initiation. Clearly more investigation in this area is needed.

3.4.2 Foam Encapsulant / No Encapsulant

The uncoated capacitor and resistor from Figure 3-29 resulted in underfill stresses of 74.4 MPa and 72.5 MPa respectively. By removing the epoxy encapsulant, the underfill stress for the capacitor and resistor both dropped approximately ~18% to 60 MPa as shown in Figure 3-34. Also shown in the figure, is the surprisingly small difference in stress between the capacitor and resistor underfills, and the lack of any effect of the foam encapsulation on the stress.

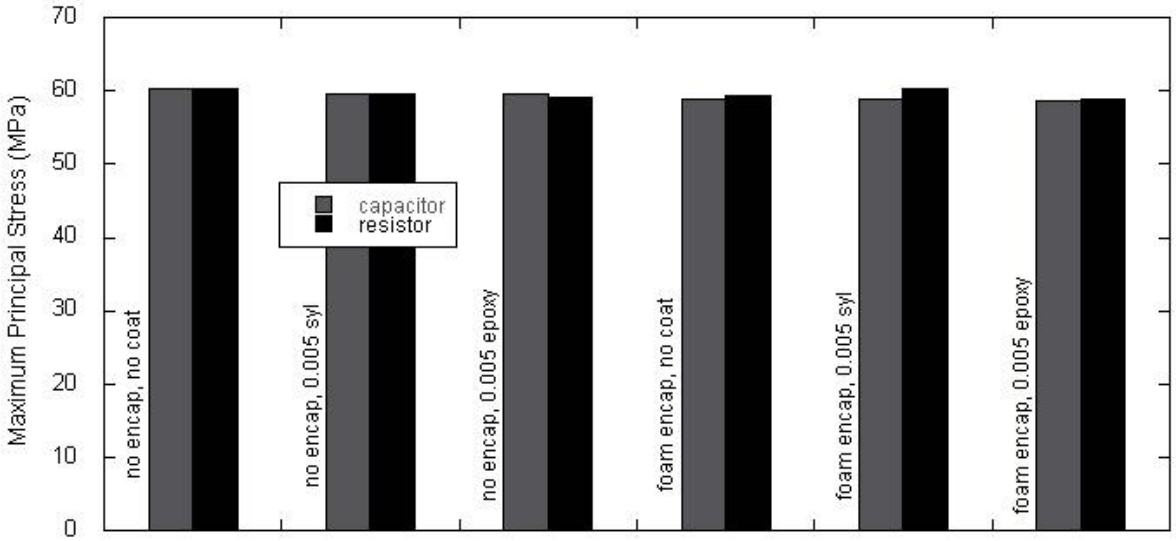

Figure 3-34: Underfill maximum principal stress for capacitor and resistor with various encapsulation/elastomer coating cases and 20% hard filler in the underfill.

Effect of Underfill Filler Volume Fraction

The predicted underfill maximum principal stress for the unencapsulated capacitor and resistor due to the addition of an underfill and filler are depicted in Figure 3-35. Because the encapsulation/coating options seemed to have no effect on the underfill stresses, only the unencapsulated uncoated component results are plotted.

As with the epoxy encapsulated components, obvious "trends" appear for the unencapsulated as well. In all cases, adding any filler to the underfill almost linearly decreases the underfill stress. Adding 40% FVF solid hard filler to the capacitor underfill decreased the stress from 62.7MPa to 55.5 MPa, or 11.5%, while adding 40% FVF GMB filler to the underfill decreased the stress by 30.6% to 43.5 MPa (Figure 3-35, left). The trends were almost identical for the resistor. By adding 40% FVF solid hard filler to the resistor underfill, the maximum principal stress decreased 11.2% from 63.4 MPa to 56.3 MP, while adding 40% FVF GMB filler to the underfill decreased the stress by 32.5% to 42.8 MPa (Figure 3-35, right).

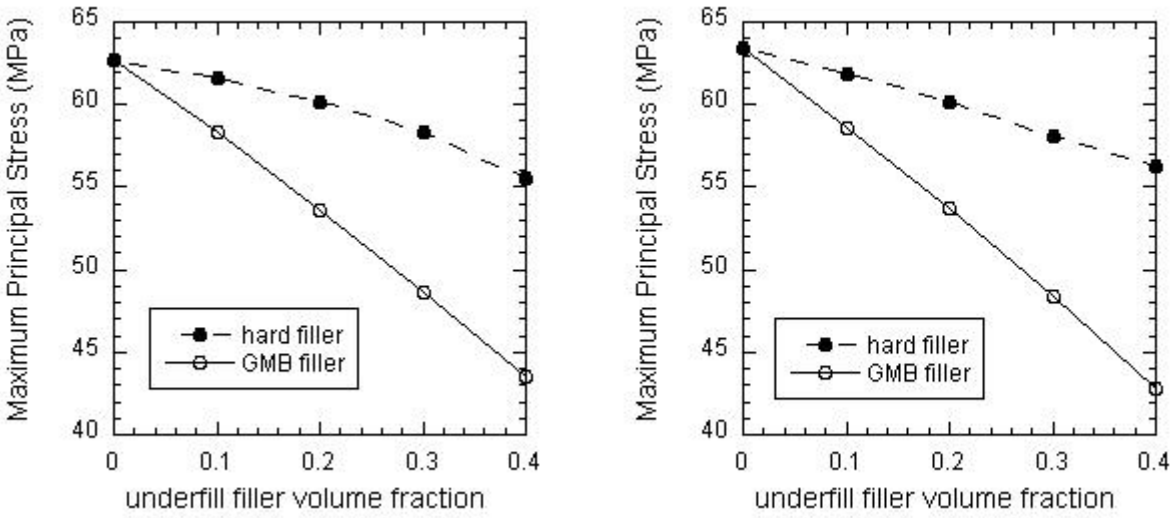

Figure 3-35: Unencapsulated capacitor (left) and resistor (right) underfill maximum principal stress for various underfill filler volume fractions with no coating.

3.5 PCB Bending during Thermal Cycles

Circuit board bending significantly affects the solder fatigue life of surface mounted components. Figure 3-36 demonstrates a geometry that is particularly susceptible to board bending. Because of the mismatch in coefficients of thermal expansion of the GMB epoxy over-encapsulation, the steel board support and other materials, significant board bending at the board-to-support interface was predicted using finite element modeling. The effect of this bending on solder fatigue life was investigated by inserting a component into the model at two separate locations using tied contact. The component used for the calculations was the surface mount resistor modeled in previous sections.

As seen in the figure, the resistor was inserted above the board-to-support interface, and also at a more benign location from the support. The resistor was assumed to be coated with 0.02" PMB polysulfide coating with a 40% FVF GMB underfill. The thermal cycle consisted of cooling from 80ºC to -55ºC, followed by heating to 70ºC, and finally cooling back to -55ºC. The change in plastic strain used for the Coffin-Manson solder fatigue calculation (Section 2.5) was calculated between the two low thermal excursions of -55ºC for eutectic tin-lead solder.

The results of the calculations were quite dramatic. The predicted fatigue life of the resistor located above the board-to-support interface (Figure 3-36, top) was 27 thermals cycles until solder crack initiation, and the fatigue life of the resistor located away from the support (Figure 3-36, bottom) was calculated to be 140 thermal cycles.

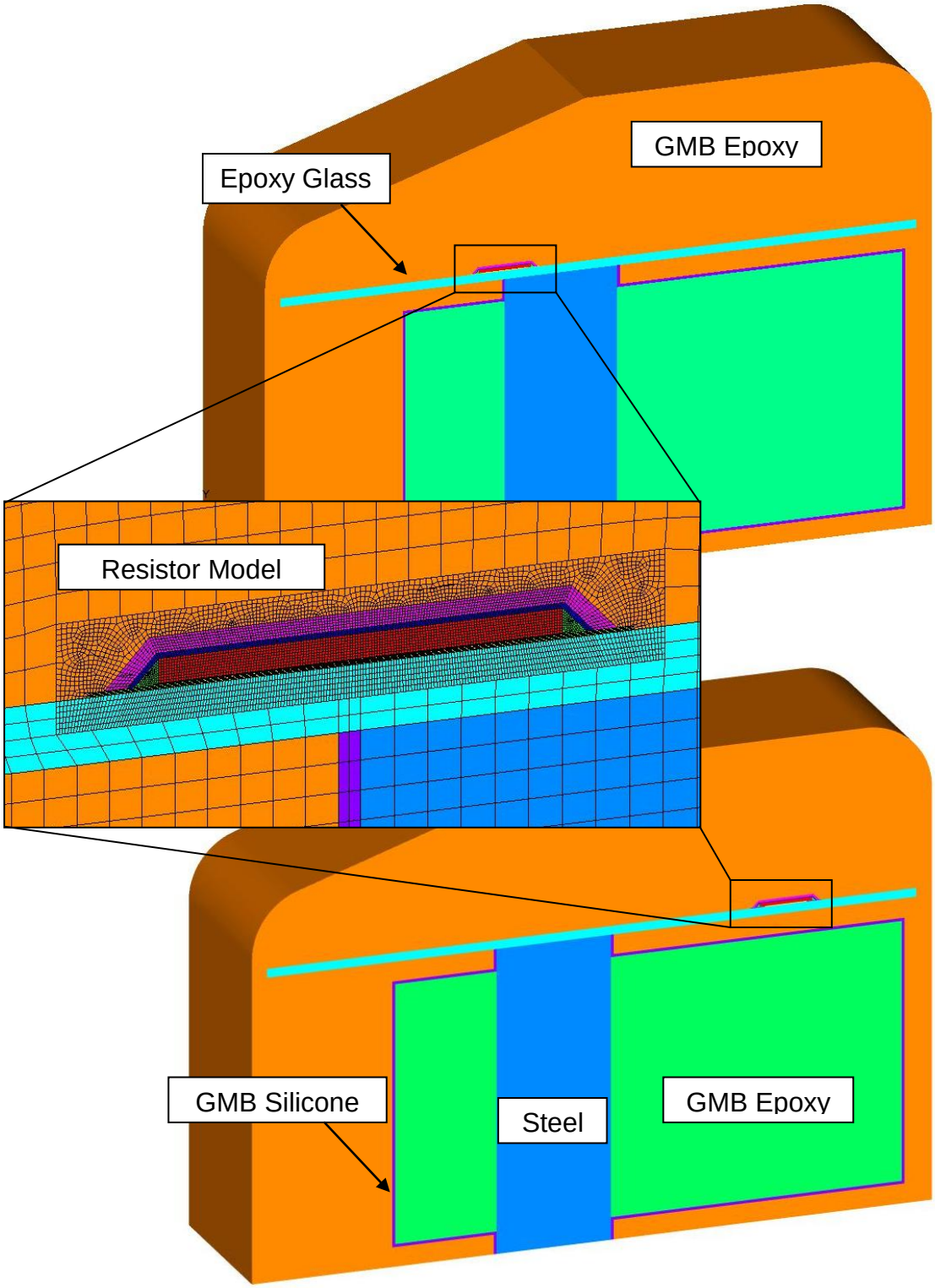

Figure 3-36: Half symmetry model of GMB epoxy encapsulated electronic device with resistor on circuit board in two different locations.

4 CONCLUSIONS AND FUTURE STUDIES

Computational tools have been developed to analyze the stresses and strains generated in packaged electronic components. Some typical material data and constitutive equations for unfilled and filled glassy thermosets, elastomers and eutectic tin-lead solder also have been presented. Using these computational tools and material definitions, finite element analyses were performed to evaluate design options for generic surface mounted components subjected to thermal cycling only. From this effort, an attempt has been made to identify, where possible, simple design guidelines for surface mount electronics packaging by looking for "trends". It should be noted that all calculations presented assume a free surface boundary condition. That is, the exterior surface of the encapsulant is not adhered to a "stiff" housing. A stiff housing would produce a high degree of confinement not considered in these analyses.

Effect of Epoxy Encapsulation

The first, and most obvious, conclusion from these modeling efforts was that 828/DEA/GMB epoxy over encapsulation reduced the solder fatigue life of surface mount components by an order of magnitude relative to an unencapsulated system. Stress in the underfill was virtually unchanged, and the ceramic stress was slightly increased by the addition of the epoxy over-encapsulation.

Effect of Elastomer Coating

Four elastomer coatings were investigated: unfilled Sylgard, GMB filled Sylgard, polysulfide, and PMB filled polysulfide. The stresses experienced by the unfilled elastomer coatings when over-encapsulated by an epoxy will likely result in tearing or debonding of the coating (important for finite element model boundary conditions). The filled elastomer coatings should not tear or debond. The application of the elastomer coating to the large encapsulated capacitor resulted in a significant reduction of hydrostatic stress in the ceramic. The cost however was a large increase in the localized ceramic stress at the solder joints. The elastomer coating had a minimal impact on the solder fatigue life of either the resistor or capacitor, but did result in an increase in the underfill stress.

Effect of Underfill Filler Volume Fraction

For 828/DEA/GMB epoxy encapsulated components, adding an underfill significantly increased solder fatigue life over the void condition. Adding hard filler to the underfill significantly increased the ceramic stress for the elastomer coated capacitor, but the stress increase was not as dramatic in the uncoated case. Increasing the filler volume fraction (FVF) of hard filler improved the solder fatigue life of epoxy encapsulated components, but GMB had a minimal effect. Increasing the hard FVF in the underfill increased the underfill stress, and increasing the GMB FVF in the underfill decreased the underfill stress.

For unencapsulated/foam encapsulated components, optimal filler volume fractions for underfills were observed. One such value that stood out was 20% FVF hard filler which coincidentally is the formulation of Hysol FP107 (Section 2.2) currently used at Sandia. In some cases, it was found that adding filler to the underfill could increase or decrease the solder fatigue

life, demonstrating the need for modeling. In addition, adding underfill could result in opposite trends for the capacitor and resistor. Adding underfill to the capacitor slightly decreased ceramic stress, while adding underfill to the resistor slightly increased ceramic stress, but in both cases, adding filler moved the stresses toward the no underfill stress state.

Effect of Foam Encapsulation

Foam encapsulation reduced the solder fatigue life of capacitor by approximately one half of the unencapsulated value, but had relatively little impact on the fatigue life of the resistor. The stress in the underfill and ceramic were also relatively unaffected by the addition of foam encapsulation. Stress in the underfill was consistently decreased with the addition of filler to the underfill for the foam encapsulated resistor and capacitor.

Effect of Epoxy Coating

Adding a thin epoxy coating to unencapsulated or foam encapsulated components slightly reduced the peak ceramic stress but also reduced the solder fatigue life.

Simplified Design Guide

A summary of identified trends that should be helpful to designers are summarized in Table 4-1 through Table 4-4. The tables are configured to demonstrate the effects of changes from a baseline encapsulation case. The encapsulation cases are defined in the left three columns, and in the underfill column, the term hard or GMB indicate an underfill with filler. Values in green indicate an improvement from the baseline, values in red indicate a decline, and values in yellow are within 10% of the baseline. The center three columns are the actual peak values predicted (min or max) for the identified encapsulation/coating/underfill case (for example, in one case, the maximum fatigue life may have occurred with 30% FVF hard filler, and may be further investigated in Section 3). The right three columns contain the percent change from the base line.

Future Studies

The design trends for the generic surface mounted components that have been discussed in this report came from finite element analyses of thermal cycling only. Clearly, there can be other important design environments to consider. The processing steps involved in manufacturing (e.g., curing of underfills) may generate significant residual stresses that are not negligible. Furthermore, the dynamics associated with operational conditions that may include violent impacts also should be considered. It is possible that the broad spectrum of requirements arising from the life cycle of the packaged electronics may lead to conflicting design solutions. Designers need to be aware of these tradeoffs. Subsequent work will focus on understanding how best to survive these other environments and how the conclusions from thermal analyses might be altered by dynamics.

Table 4-1: Effects of encapsulation on component stress, solder fatigue, and underfill stress.

RESISTOR

Case			Values			Percent Change from Baseline		
Encap	**Coating**	**Underfill**	ceramic max princ stress (MPa)	fatigue life (thermal cycles)	underfill max princ stress (MPa)	ceramic stress	fatigue life	underfill stress
none	none	none	50.8	7700	NA	18%	1251%	NA
none	none	unfilled	57.5	4500	63.5	8%	689%	2%
none	epoxy	unfilled	36	3200	63.5	42%	461%	2%
foam	none	unfilled	53.4	3500	63.5	14%	514%	2%
foam	epoxy	unfilled	37.3	2800	63.5	40%	391%	2%
epoxy	none	unfilled	62.3	570	65	baseline	baseline	baseline
epoxy	elastomer	unfilled	55.5	560	82	11%	-2%	-26%

CAPACITOR

Case			Values			Percent Change from Baseline		
Encap	**Coating**	**Underfill**	ceramic max princ stress (MPa)	fatigue life (thermal cycles)	underfill max princ stress (MPa)	ceramic stress	fatigue life	underfill stress
none	none	none	73	17000	NA	-19%	3300%	NA
none	none	unfilled	57.5	10500	63	6%	2000%	2%
none	epoxy	unfilled	45	7500	63	27%	1400%	2%
foam	none	unfilled	53.6	4500	63	13%	800%	2%
foam	epoxy	unfilled	46.7	3900	63	24%	680%	2%
epoxy	none	unfilled	61.3	500	64	baseline	baseline	baseline
epoxy	elastomer	unfilled	89.5	550	100	-46%	10%	-56%

Table 4-2: Effects of elastomer coating and underfill filler on component stress, solder fatigue, and underfill stress for epoxy encapsulated components.

RESISTOR

	Case			Values		Percent Change from Baseline		
Encap	**Coating**	**Underfill**	ceramic max princ stress (MPa)	fatigue life (thermal cycles)	underfill max princ stress (MPa)	ceramic stress	fatigue life	underfill stress
epoxy	none	none	70.5	330	NA	-13%	-42%	NA
epoxy	elastomer	none	69.5	450	NA	-12%	-21%	NA
epoxy	none	unfilled	62.3	570	65	baseline	baseline	baseline
epoxy	none	GMB	60	690	43	4%	21%	34%
epoxy	none	hard	56	770	83	10%	35%	-28%
epoxy	elastomer	unfilled	55.5	560	82	11%	-2%	-26%
epoxy	elastomer	GMB	50	600	61	20%	5%	6%
epoxy	elastomer	hard	58	730	107	7%	28%	-65%

CAPACITOR

	Case			Values		Percent Change from Baseline		
Encap	**Coating**	**Underfill**	ceramic max princ stress (MPa)	fatigue life (thermal cycles)	underfill max princ stress (MPa)	ceramic stress	fatigue life	underfill stress
epoxy	none	none	53	180	NA	14%	-64%	NA
epoxy	elastomer	none	86	240	NA	-40%	-52%	NA
epoxy	none	unfilled	61.3	500	64	baseline	baseline	baseline
epoxy	none	GMB	55.5	500	44	9%	0%	31%
epoxy	none	hard	73	610	100	-19%	22%	-56%
epoxy	elastomer	unfilled	89.5	550	100	-46%	10%	-56%
epoxy	elastomer	GMB	98	500	82	-60%	0%	-28%
epoxy	elastomer	hard	139.5	820	160	-128%	64%	-150%

Table 4-3: Effects of epoxy coating and underfill filler on component stress, solder fatigue, and underfill stress for foam encapsulated components.

RESISTOR

Case			Values			Percent Change from Baseline		
Encap	**Coating**	**Underfill**	ceramic max princ stress (MPa)	fatigue life (thermal cycles)	underfill max princ stress (MPa)	ceramic stress	fatigue life	underfill stress
foam	none	none	49.4	6200	NA	7%	77%	NA
foam	epoxy	none	27.3	5500	NA	49%	57%	NA
foam	none	unfilled	53.4	3500	63.5	baseline	baseline	baseline
foam	none	GMB	51	7500	43	4%	114%	32%
foam	none	hard	49.6	6100	56.5	7%	74%	11%
foam	epoxy	unfilled	37.3	2800	63.5	30%	-20%	0%
foam	epoxy	GMB	31	5500	43	42%	57%	32%
foam	epoxy	hard	30.5	5800	56.5	43%	66%	11%

CAPACITOR

Case			Values			Percent Change from Baseline		
Encap	**Coating**	**Underfill**	ceramic max princ stress (MPa)	fatigue life (thermal cycles)	underfill max princ stress (MPa)	ceramic stress	fatigue life	underfill stress
foam	none	none	63.5	6700	NA	-18%	49%	NA
foam	epoxy	none	37.75	6200	NA	30%	38%	NA
foam	none	unfilled	53.6	4500	63	baseline	baseline	baseline
foam	none	GMB	58	9300	43.5	-8%	107%	31%
foam	none	hard	61	11000	55.5	-14%	144%	12%
foam	epoxy	unfilled	46.7	3900	63	13%	-13%	0%
foam	epoxy	GMB	38.4	8000	43.5	28%	78%	31%
foam	epoxy	hard	35.5	8000	55.5	34%	78%	12%

Table 4-4: Effects of epoxy coating and underfill filler on component stress, solder fatigue, and underfill stress for unencapsulated components.

RESISTOR

Case			Values			Percent Change from Baseline		
Encap	**Coating**	**Underfill**	ceramic max princ stress (MPa)	fatigue life (thermal cycles)	underfill max princ stress (MPa)	ceramic stress	fatigue life	underfill stress
none	none	none	50.8	7700	NA	12%	71%	NA
none	epoxy	none	31.5	6600	NA	45%	47%	NA
none	none	unfilled	57.5	4500	63.5	baseline	baseline	baseline
none	none	GMB	53.9	8700	43	6%	93%	32%
none	none	hard	52.5	8600	56.5	9%	91%	11%
none	epoxy	unfilled	36	3200	63.5	37%	-29%	0%
none	epoxy	GMB	31.6	6000	43	45%	33%	32%
none	epoxy	hard	33.2	7200	56.5	42%	60%	11%

CAPACITOR

Case			Values			Percent Change from Baseline		
Encap	**Coating**	**Underfill**	ceramic max princ stress (MPa)	fatigue life (thermal cycles)	underfill max princ stress (MPa)	ceramic stress	fatigue life	underfill stress
none	none	none	73	17000	NA	-27%	62%	NA
none	epoxy	none	41.8	10600	NA	27%	1%	NA
none	none	unfilled	57.5	10500	63	baseline	baseline	baseline
none	none	GMB	61	30500	43.5	-6%	190%	31%
none	none	hard	63	26500	55.5	-10%	152%	12%
none	epoxy	unfilled	45	7500	63	22%	-29%	0%
none	epoxy	GMB	40.6	19250	43.5	29%	83%	31%
none	epoxy	hard	39.7	17500	55.5	31%	67%	12%

5 REFERENCES

1. Caruthers, J. M.; Adolf, D. B.; Chambers, R. S.; Shrikhande, P. Polymer 2004; 45: 4577-4597.
2. Adolf, D. B.; Chambers, R. S.; Caruthers, J. M. Polymer 2004; 45: 4599-4621.
3. Adolf, D. B.; Chambers, R. S.; Flemming, J. J. Rheol. 2007; 51: 517-540.
4. Adolf, D. B.; Chambers, R. S.; Neidigk, M. A. Polymer 2009; 50: 4257-4269.
5. Adolf, D. B.; Chambers, R. S. J.Polym. Sci.-Phys. 2005; 43: 3135-3150.
6. McKenna interface Tg
7. Adolf, D. B.; Stavig, M. E.; Kawaguchi, S.; Chambers, R. S. J.Adhesion 2007; 83: 85-104.
8. Van Krevelen, D. W. Properties of Polymers, Elsevier, NY, 1976.
9. Bicerano, J. Prediction of Polymer Properties, Dekker, NY, 2002.
10. May, C. A. Epoxy Resins, Dekker, NT, 1988.
11. Hill, R. J. Mech, Phys. Solids 1963; 11: 357.
12. Hashin, Z.; Shtrikman, S. J. Mech, Phys. Solids 1963; 13: 89 and 213.
13. Ferry, J. D. Viscoelastic Properties of Polymers, Wiley, NY, 1980.
14. Mistou, S.; Karama, M. J. Comp. Mat. 2000; 34: 1696-1709.
15. Jones, R. M. Mechanics of Composite Materials, Taylor & Francis, Philadelphia, 1999.
16. Visconti, K. Three-Dimensional Thermal and Mechanical Characterization of Glass-Fiber Reinforced Polymer Matrix Composites, PhD Thesis, New Mexico Institute of Mining and Technology, Socorro, NM, May, 2007.
17. Stephens, J.; Frear, D., Metal. Mat. Trans. A 1999; 30A: 1301-1313.
18. Boyce, B.; Brewer, L.; Perricone, M.; Neilsen, M., J. Elec. Pkg., submitted Sept. 2010.
19. Neilsen, M.; Burchett, S., Stone, C., Stephens, J. SAND96-0984, Sandia National Laboratories, Albuquerque, NM, April 1996.
20. Fossum, A.; Vianco, P.; Neilsen, M.; Pierce, D. J. Elec. Pkg. 2006; 128: 71-81.
21. More, J. Lecture Notes in Mathematics 630; Edt. G.A. Watson, Springer Verlag, 1978.
22. Solomon, H.D. IEEE Trans. Comp. Hybrids Manuf. Tech. 1986; 9: 423-431.

DISTRIBUTION

1 US Army ARDEC
Attn: Dr. Donald Carlucci
RDAR-SM
Picatinny Arsenal, NJ 07806-5000

6 US Army ARDEC
Attn: Dr. Nien-Hua Chao
RDAR-MEF-E
Picatinny Arsenal, NJ 07806-5000

1 US Army ARDEC
Attn: Dr. Jennifer Cordes
RDAR-MEF-E
Picatinny Arsenal, NJ 07806-5000

1 Danny R. Hayles
DTRA/RD-CXWW Bldg 13A, Suite 392
101 West Eglin Blvd
Eglin AFB, FL 3252

4 Dr. Kirk Vanden
AFRL/RWPC
101 W. Eglin Blvd.
Eglin AFB, Florida 32542-6810

1 Dr. Jason R. Foley
AFRL/RWMFI
306 W. Eglin Blvd., Bldg 432
Eglin AFB, FL 32542-5430

1	MS0340	Mike Rimbert	2136
1	MS0344	Ken Eras	2624
1	MS0344	James J. Calderone	2625
1	MS0344	Pat Smith	2625
1	MS0344	Clifton F. Briner	2626
1	MS0344	William Nance	2626
1	MS0344	Sara N. Pecak	2626
1	MS0344	George Clark	2627

10	MS0346	Robert S. Chambers	1524
10	MS0346	Matthew A. Neidigk	1526
1	MS0346	Michael J. Starr	1526
1	MS0348	Gerald Boyd	5331
1	MS0348	John Dye	5331
1	MS0348	Dale Brandt	5339
1	MS0348	Rick Heinzleman	5352
1	MS0348	John Moser	5352
1	MS0348	Jeff Pankonin	5353
1	MS0348	John L. Williams	5353
1	MS0349	Daniel Petersen	2614
1	MS0352	Jeremy A. Palmer	1718
1	MS0352	Nathan P. Young	1718
1	MS0372	Huei Eliot Fang	1524
1	MS0372	Kristin Dion	1525
1	MS0372	J. Franklin Dempsey	1526
1	MS0382	Brad Boswell	2127
1	MS0382	Joe DiMambro	2127
1	MS0402	Aaron Murray	5762
1	MS0405	Henry Duong	0416
1	MS0405	Kevin Maloney	0416
1	MS0405	Greg Scharrer	0416
1	MS0405	Todd Hinnerichs	0425
1	MS0405	Jared McLaughlin	0425
1	MS0415	Celeste A. Drewien	0245
1	MS0434	Grant Bloom	0412
1	MS0447	Christine C. Mitchell	2122
1	MS0447	Brandon Moore	2122
1	MS0447	Hal Radloff	2122
1	MS0447	Rashad Raynor	2122
1	MS0447	Shelly Sanchez	2122
1	MS0447	John Sichler	2122
1	MS0447	Tom Togami	2122
1	MS0447	Heather A. Wampler	2122
1	MS0447	Alex Waters	2122
1	MS0447	Doug Weiss	2122
1	MS0447	Jeff Whitlow	2122
1	MS0447	Joel Wirth	2122
1	MS0447	Scoti Hagerman	2127
1	MS0447	Lou Weichman	2127

1	MS0451	Dave Gelet	2144
1	MS0482	Daryl McCollister	0414
1	MS0487	Tom Denman	2142
1	MS0487	Brian Geery	2142
1	MS0487	Melissa Wilson	2142
1	MS0492	Susan Esfahani	2625
1	MS0501	Mandy Younger	5343
1	MS0513	John McBrayer	5358
1	MS0523	Jeff Christensen	1733
1	MS0523	Gordon Grimm	1733
1	MS0525	Robert O. Sanchez	1733
1	MS0529	Ken Plummer	5354
1	MS0529	Dave Wiegandt	5355
1	MS0549	Allen Baca	5953
1	MS0549	Bernie Jokiel	5953
1	MS0614	Bill Chambers	2547
1	MS0614	Tom Hund	2547
1	MS0614	Steve Showalter	2547
1	MS0614	Nick Streeter	2547
1	MS0620	Chris Dyck	5654
1	MS0638	Anthony Wingate	0422
1	MS0638	Dennis Owens	0424
1	MS0638	Ron Farmer	0426
1	MS0661	Aaron Niese	2623
1	MS0661	David Beck	2627
1	MS0661	Ron Focia	2627
1	MS0661	Chad Hettler	2627
1	MS0661	Jason Jarosz	2627
1	MS0661	R. Scott McEntire	2627
1	MS0661	Patrick D. O'Malley	2627
1	MS0661	Mike Partridge	2627
1	MS0678	Aaron M. Ison	2617
1	MS0678	John W. Franklin	2617
1	MS0678	Edward G. Winrow	2617
1	MS0824	James M. Redmond	1525
1	MS0824	Leah W. Tuttle	1525
1	MS0829	Janet Sjulin	0413
1	MS0847	Peter J. Wilson	1520
1	MS0860	Matthew Brown	2622
1	MS0862	Danny Rey	2732

1	MS0862	Barbara J. Wells	2732
1	MS0862	Carla C. Busick	2734
1	MS0862	Keith W. Meredith	2734
1	MS0869	Pamela K. Walker	2714
1	MS0869	Jedediah J. Alderete	2732
1	MS0869	Pierrette H. Gorman	2732
1	MS0869	Neil A. Lapetina	2732
1	MS0869	Gregory L. Neugebauer	2732
1	MS0869	Therese A. Ordonez	2732
1	MS0869	Frank R. Trowbridge	2732
1	MS0869	Jose Vigil	2732
1	MS0872	Ruben Muniz	0423
1	MS0873	John C. Nguyen	2712
1	MS0885	Terrence L. Aselage	1810
1	MS0885	Mark F. Smith	1830
1	MS0886	Donald E. Susan	1831
1	MS0889	Paul T. Vianco	1831
1	MS0956	Steven C. Anderson	2663
1	MS0958	Howard W. Arris	1833
1	MS0958	Kevin N. Austin	1833
1	MS0958	Michael J. Kelly	1833
1	MS0958	Jamie M. Kropka	1833
1	MS0958	Scott W. Spangler	1833
1	MS0958	David L. Zamora	1833
1	MS0959	Douglas A. Chinn	1832
1	MS1064	Andre Claudet	2613
1	MS1064	Ernie Garcia	2614
1	MS1064	Sergio Gonzalez	2614
1	MS1064	Julia Hammond	2614
1	MS1064	Mark Polosky	2614
1	MS1070	Chungnin C. Wong	1526
1	MS1070	Jordan Massad	1526
1	MS1156	Kelly A. Rhodes	5435
1	MS1164	Paul C. Butler	5435
1	MS1202	Reid Bennett	5953
1	MS1206	Kelly Wiegandt	5963
1	MS1218	Rich Neiser	5942
1	MS1398	Michael K. Neilsen	1526
1	MS1452	David Damm	2552
1	MS1452	Evan Dudley	2552

1	MS1453	Jim Salas	2553
1	MS9102	Jennifer Clark	8135
1	MS9106	Brett Wagstaff	8226
1	MS9108	Raphael Molle	8221
1	MS9154	Phil Bryson	8221

1	MS0899	Technical Library	9536 (electronic copy)